POLITECNICO DI TORINO

Applied Science and Technology Department

PhD thesis in Materials Science and Technology

XXVIII cycle (2013-2016)

Silver nanostructures on porous silicon for multiplexed Surface Enhanced Raman Scattering biosensing platforms

Chiara Novara

Tutors	prof. Francesco Geobaldo and prof. Fabrizio Giorgis
PhD Coordinator	prof. Claudio Badini

5th April 2016

To my family

Contents

Acknowledgements

Abstract

I Background

1. SERS spectroscopy 1
  1.1 Introduction 1
  1.2 Raman Spectroscopy 1
  1.3 Surface Enhanced Ramana Scattering (SERS) 4
    1.3.1 Electromagnetic enhancement mechanism 5
      1.3.1.1 Localized Surface Plasmons (LSPRs) 5
        1.3.1.1.1 LSPRs in single particle systems: size and shape effect 7
        1.3.1.1.2 LSPRs in multiple particle systems: inter-particle coupling in hot-spots 8
        1.3.1.1.3 Effect of sorrounding matrixes or substrates 10
    1.3.2 Chemical enhancement mechanism 11
    1.3.3 Experimental determination of the Enhancement Factor (EF) 12

2. SERS substrates 14
  2.1 Introduction 14
  2.2 SERS substrates fabrication methods 14
    2.2.1 Colloidal systems 14
    2.2.2 Solid systems 16
      2.2.2.1 Porous silicon SERS substrates 20
  2.3 SERS substrates for biosensing applications 23
    2.3.1 SERS bioassays and biosensors 23
      2.3.1.1 Small metabolites detection 23
      2.3.1.2 Protein detection 24
      2.3.1.3 DNA and oligonucleotides detection 25
        2.3.1.3.1 Micro-RNAs 27
    2.3.2 Lab-on-chip SERS platforms 28
      2.3.2.1 Inkjet printed SERS substrates 29
      2.3.2.2 Microfluidic integration 30

3. Characterization techniques 33
3.1 Introduction 33
3.2 Field Emission Scanning Electron Microscopy 33
3.3 UV-Vis-NIR spectroscopy 34
3.4 Raman spectroscopy 35
3.5 Optical Contact Angle 36

II Experimental

4. Materials and Methods 38
4.1 Porous silicon electrochemical etching 38
4.2 Silver nanoparticles synthesis 38
4.2.1 Immersion plating 38
4.2.2 Inkjet printing 39
4.3 Optical and morphological characterization 39
4.4 Raman characterization 39
4.4.1 4-mercaptobenzoic acid detection and Raman mapping 39
4.4.2 Rhodamine 6G detection 40
4.4.3 Cyanine 5 detection 40
4.5 Biofunctionalization protocol 40
4.5.1 SERS substrates stability in buffers 40
4.5.2 Bioassay protocol 41
4.5.3 Raman analysis 41

5. Silver coated porous silicon SERS substrates 42
5.1 Introduction 42
5.2 Application of a systematic protocol to probe SERS substrates 42
5.2.1 Analyte selection: Rhodamine 6G *vs.*4-mercaptobenzoic acid 42
5.2.2 Wavelength dependence of Raman efficiency and uniformity 45
5.2.2.1 Morphology and optical analysis of Ag coated pSi 46
5.2.2.2 Raman mapping 49
5.3 Conclusions 51

6. Inkjet printed arrays in porous silicon 53
6.1 Introduction 53
6.2 In situ synthesis of silver nanoparticles via inkjet printing 53
6.2.1 Influence of printhead passes repetition and drop-to-drop step size 53

6.2.2 Influence of silver nitrate concentration 55
6.2.3 Influence of ink properties 57
6.3 Raman efficiency and uniformity 59
6.4 Conclusions 61

7.Integration of Ag-coated porous silicon SERS membranes in all-PDMS optofluidic chips .. 62
7.1 Introduction 62
7.2 Chip fabrication 62
7.2.1 Porous silicon patterning and transfer 63
7.2.2 Immersion plating of porous silicon membranes 64
7.3 Raman efficiency and uniformity 65
7.3.1 Chip calibration 67
7.4 Towards an all-microfluidic process 68
7.4.1 Dynamic synthesis of silver nanoparticles and in situ monitoring ....
7.5 Conclusions 71

8. Label free miRNA detection 72
8.1 Introduction 72
8.2 Biocompatibility of the SERS substrates 72
8.2.1 SERS substrates stability in buffer solutions 72
8.2.1.1 Ag-pSi 72
8.2.1.2 Inkjet printed Ag-pSi 73
8.2.1.1 Ag-pSi-PDMS membranes 74
8.3 Functionalization protocol on printed and PDMS-supported Ag-pSi 75
8.3.1 Nonspecific signal removal 76
8.3.2 DNA probe immobilization 77
8.3.2.1 Optimization of the desalting process 77
8.3.2.2 Interpretation of probe Raman signal 78
8.3.2.2.1 Effect of the probe concentration 80
8.3.3 miRNA hybridization 82
8.3.3.1 Labelled miRNA222- cy5 detection 82
8.3.3.2 Unabelled miRNA222 hybridization 84
8.3.4 Cross-check through the ELISA assay 86
8.3.5 Conclusions 87

Conclusions and future perspectives 88

References 89

Publications and Conferences... 97

Acknowledgements

Vorrei ringraziare tutte le persone che hanno contribuito alla preparazione di questa tesi, sia attraverso le loro competenze e il loro lavoro che con il loro supporto. Innanzitutto Fabrizio Giorgis, per la sua disponibilità e apertura con cui ha seguito e indirizzato il mio percorso di dottorato, e Geo, per avermi dato questa opportunità.

Vorrei inoltre ringraziare Ale C per le ore e ore di esperimenti di funzionalizzazione insieme e per l’esempio che mi dà dell’importanza di lavorare con correttezza e precisione (e per avermi fornito i dati ELISA), Ale V. per avermi introdotto alla spettroscopia Raman e alla preparazione del silicio poroso e Paola per avermi aiutata sia con la sua esperienza riguardo alle tecniche di supeficie sia nella risoluzione delle problematiche legate alla vita di laboratorio.

Ringrazio Andrea Lamberti per aver condiviso con me la sua competenza nel campo della microfluidica in PDMS, Angelo Angelini per aver svolto le simulazioni FEM, Samuele Porro e tutti creatori di Politronica s.r.l. per avermi introdotto alla tecnologia inkjet e Marco Fontana per avermi insegnato ad utilizzare il FESEM.

Vorrei ancora ringraziare Alois Bonifacio, Silvia Dalla Marta e Stefano Fornasaro per l’accogliente ospitalità dimostrata nel periodo trascorso a Trieste e per avermi fatto conoscere aspetti diversi della spettroscopia Raman.

Un altro ringraziamento è rivolto ad Elisa che mi ha accolta e orientata al mio arrivo al Politecnico, ad Alessandro, Elnaz, Diego e Luca P. per i momenti di pausa insieme.

Ringrazio i miei genitori, che per la terza volta hanno dovuto subire la scrittura di una tesi e quindi meritano la dedica, per il loro continuo supporto. Ringrazio Anna, per la sua amicizia. Ringrazio infine Stefano per aver scelto di starmi accanto.

Abstract

Surface Enhanced Raman Scattering (SERS) technique merges an excellent sensitivity and a highly specific label free detection which can be exploited in miniaturized devices with a multiplexed approach. The development of plasmonic nanostructures, aimed to SERS analysis, satisfies therefore the need for point-of-care multianalyte sensing and biosensing platforms, both in the framework of diagnostics and therapy monitoring.

In this thesis, SERS active metal-dielectric nanostructures based on silver-coated porous silicon (Ag-pSi) are carefully optimized for biodetection purposes. The thesis is organized in two parts. Basic concepts, necessary to the understanding of the experimental work are provided in the "Background" section, dealing with fundamentals of SERS spectroscopy (Chapter 1), SERS substrates fabrication aimed to biosensing applications (Chapter 2) and the main techniques devoted to the substrates characterization (Chapter 3).

On the other side, the "Experimental" part includes the applied materials and methods (Chapter 4) and the presentation and discussion of the experimental results. (Chapters 5-8). In detail, a reliable SERS sensing requires a deep characterization of the optical and SERS response of the substrate providing the Raman enhancement. Theoretical and experimental techniques (FEM simulations and multi-wavelength Raman mapping) are systematically applied to get new insight into the fundamental and applicative SERS properties of Ag-pSi (Chapter 5).

Two different approaches for the fabrication of Ag-pSi multianalyte platforms are then presented and discussed. Chapter 6 deals with the in situ synthesis of silver nanoparticles (NPs) patterns synthesized by ink-jet printing. The correlation between the growth parameters, morphology and SERS response is studied in order to optimize the SERS signal efficiency and uniformity of the Ag-pSi printed nanostructures. On the other hand, Chapter 7 concerns with the fabrication of multichamber Ag-pSi-PDMS microfluidic chips, which can be applied as portable SERS multiplexing devices. An all-microfluidic in-flow synthesis of silver NPs is performed, integrating the preparation of the SERS active substrate and the detection step on the same chip.

Finally, a biofunctionalization protocol developed for the detection of miRNA222 (a recognized tumor marker) is optimized for the application to the Ag-pSi SERS substrates, assessing their compatibility to bioassays and suggesting the Ag-pSi nanostructures integrated in elastomeric chips as advantageous platforms for miRNA profiling, as well as for several other bioanalytical applications (Chapter 8).

I Background

Chapter 1

SERS spectroscopy

1.1 Introduction

Surface Enhanced Raman Scattering (SERS) has become widely recognized as a powerful tool to investigate several different systems, with applications ranging from forensic and bioanalytical chemistry, to catalysis, including also new emerging fields like food quality and safety assessment.[1–3] The SERS effect consists in the enormous amplification of the Raman scattering (RS) of vibrational modes by species adsorbed on or in the vicinity of nanostructured materials with the appropriate optical properties. Thanks to this enhancement, SERS overcomes the major limitation of Raman spectroscopy, its very low sensitivity, while keeping its rich structural and chemical information. For these reasons, after its first observation in 1974, concerning the huge enhancement of the Raman signal of pyridine adsorbed on a roughened silver electrode[4], SERS has become the most studied Raman based technique for analytical purposes, as well as for the investigation of surface phenomena. Research on the development of efficient and reproducible systems supporting SERS effect (SERS substrates) still leads to the appearance of a huge amount of studies, both theoretical and experimental, aiming to the improvement and better understanding of their SERS properties. Latest advances in the field concern with the development of real sensing platforms, integrating SERS substrates in more complex systems, like multifunctional microfluidic chips for on-line analyte detection.[5] In contrast to other highly sensitive Raman-derived techniques, such as CARS (Coherent Antistokes RS) or FSRS (Femtosecond Stimulated RS), SERS requires in fact a quite simple set-up, which is suitable for miniaturization. In this framework, the production of low-cost portable Raman spectrometer is also expected to pave the way to on-site monitoring and point-of-care applications of SERS spectroscopy.[2]

This first chapter will introduce the basis of SERS, starting from Raman spectroscopy and providing a description of the mechanisms underlying the SERS effect, which is necessary to understand the main factors affecting the SERS properties of substrates.

1.2 Raman Spectroscopy

Raman spectroscopy is an optical technique, which exploits the inelastic scattering of photons by matter to gain information about the vibrational features of the analysed sample. In detail, if molecules or atoms in solids, are irradiated by a monochromatic radiation source, a dipole moment is induced, due to the periodical perturbation of their outer electrons, which oscillates with the same frequency of the incoming electromagnetic wave. This results in scattered light, which is characterized by three different frequencies (figure 1.1): elastically scattered radiation, named Rayleigh scattering preserves the original frequency and constitutes the major part of the collected photons; inelastically scattered components show instead lower and higher frequency with respect to the incident light and are named Raman Stokes and anti-Stokes scattering. The difference in frequency is related to vibrations in the systems, which can be phonons in crystal structures and local vibrational modes in molecules.

From a classical point of view, the Raman effect can be described as follows.[6] In an anisotropic system, the oscillating induced dipole moment $\bar{\mu}$ can be written as

$$\bar{\mu} = \sum_{j} \alpha_{ij}\bar{E} \tag{1.1}$$

depending therefore on the incident electric field strength $\bar{E}$ and on α_{ij}, the polarizability, which is a tensor related to the chemical (nature of bonds) and structural properties of the analysed material. For simplicity, a time-dependent electric field directed along the X axis of a diatomic molecule is considered in the followings. The vibration of the diatomic molecule can be described by the periodic change of its inter-nuclear distance, q_v, at frequency ν_v: $q_v = q_v^0 \cos(2\pi\nu_v t)$. In this case, the polarizability is a scalar and its variation as a function of the inter-nuclear coordinate is simply described by a Taylor series of q_v:

$$\alpha = \alpha^0 + \left(\frac{d\alpha}{dq_v}\right)_0 q_v + \cdots \approx \alpha = \alpha^0 + \left(\frac{d\alpha}{dq_v}\right)_0 q_v^0 \cos(2\pi\nu_v t) \tag{1.2}$$

where higher terms are neglected for small amplitude vibrations.

The expression for the incident field, $\bar{E} = E_X^0 \cos(2\pi\nu t)$, where ν is the frequency of the incident wave, and equation 1.2 can be substituted in 1.1, giving a description of the induced dipole moment, which takes into account the three components of the scattering phenomenon:

$$\begin{gathered}\bar{\mu} = \bar{E} = E_X^0\alpha^0 \cos(2\pi\nu t) + E_X^0 \left(\frac{d\alpha}{dq_v}\right)_0 q_v^0 \cos 2\pi\nu_v t \cos(2\pi\nu t) = \\ \bar{\mu} = \bar{E} = E_X^0\alpha^0 \cos(2\pi\nu t) + \frac{E_X^0}{2}\left(\frac{d\alpha}{dq_v}\right)_0 q_v^0\{\cos[2\pi(\nu - \nu_v)t] + \cos[2\pi(\nu + \nu_v)t]\}\end{gathered} \tag{1.3}$$

The first component is the Rayleigh scattering, while the second component accounts for the Raman scattering, where the incident field frequency is modulated by the vibrational frequency of the molecule. From equation 1.3 it can be inferred that the vibration has to induce a variation of its polarizability in order to cause Raman scattering, being $\left(\frac{d\alpha}{dq_v}\right)_0 \neq 0$.

Considering the interaction of an electromagnetic wave with a quantized molecular system a semi-classical approach is however often required. In this framework Raman scattering can be visualized in the following way. Considering the ground and excited electronic energy levels of a molecular system, each equipped with several quantized vibrational levels, an incident photon is able to excite an electron to a "virtual energy state" between the ground and first excited ones. Upon decay, the electron will most probably occupy the original vibrational level of the ground electronic level, but it is also feasible that it is found in a higher or lower level. Consequently, a release or an absorption

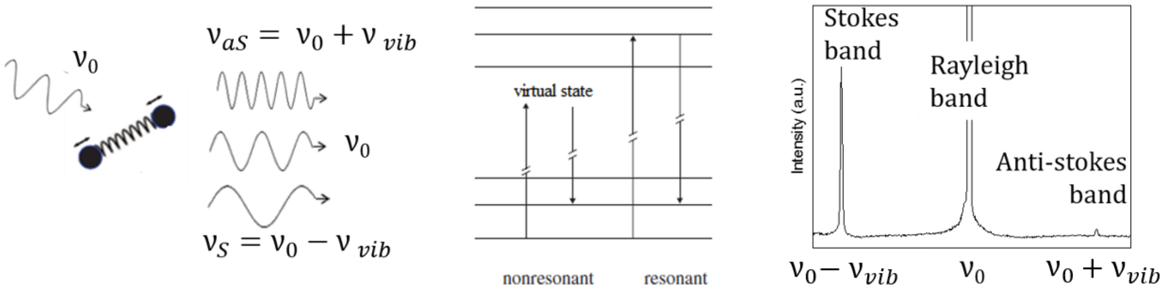

(a) (b) (c)

Figure 1.1 (a-b) Schematic representation of the Raman phenomenon and energy levels involved in normal and resonant Raman;[7] (c) example of a resulting Raman spectrum showing the Stokes, Rayleigh and anti-Stokes bands.

of energy modifies the frequency of the scattered photons. From this picture it is evident that the anti-Stokes Raman scattering is usually less intense than the Stokes component, due to the lower population in excited vibrational levels.

The central scheme in Figure 1.1 shows that in addition to the virtual state excitation, a different situation can occur. If the incident photon frequency matches the energy gap to the excited electronic level, resonant Raman is observed. In this case the Raman scattering cross section of the molecule increases and intense Raman spectra can be recorded. This condition is referred as electronic resonance.

In polyatomic molecules more than one coordinate is needed to describe the position of the atoms. For a molecule with N atoms, 3N coordinates are necessary. Three of them define its centre of gravity (translational coordinates), while three more are needed to describe the orientation (rotational coordinates) of the molecule. 3N-6 (3N-5 for linear molecules, where only two orientational degrees of freedom are possible) coordinates finally describe the vibrational behaviour of the molecule. A convenient representation of these vibrations is the definition of 3N-6 normal modes, which are synchronous motions of groups of atoms. Each normal mode, k, behaves as an independent harmonic oscillator (under the harmonic approximation), having several vibrational levels separated by an energy $\Delta E_k = h\nu_k$. Normal mode frequencies depend on the mass of the involved atoms, the molecular geometry and the interatomic forces, giving information about all of these molecular properties.

An interesting feature of this representation is that normal modes can be classified according to their symmetry, exploiting the group theory, and compared to the symmetry properties of the molecule in its equilibrium position, in order to identify selection rules for their Raman or infrared (IR) activity. From this analysis it is for example derived the so-called rule of mutual exclusion: Raman active modes in molecules with a centre of symmetry are IR inactive and vice-versa. In absence of a clear molecular symmetry, as in the case of complex biomolecules, the complementary nature of Raman and IR spectroscopy is kept, being the intense Raman modes very weak bands in IR spectra. This is ascribed to the electrical properties of the involved bonds: strongly polarized bonds, like O-H, N-H or C-O show a slight change in their polarizability upon a bond length variation, while they are subjected to a strong net dipole moment difference. Hence, such polar bonds provide intense IR bands, but weak Raman spectra. Contrary, non-polar bonds, like C-C, C-H or C=C are characterized by huge changes in their polarizability upon vibration, but they don’ t show important dipole moment, being therefore good Raman scatterers and bad IR absorbers.

The interpretation of new Raman spectra often requires the comparison to calculated spectra. Indeed, the observed frequencies correspond to normal modes of vibration that are more or less delocalized in a particular group.

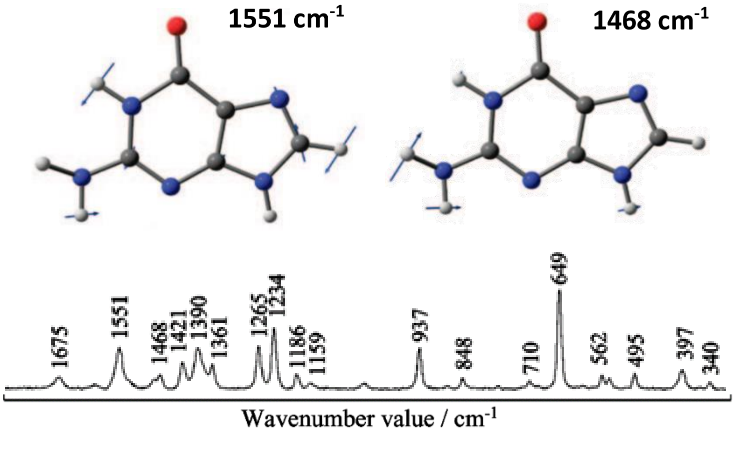

Figure 1.2. Raman spectrum of guanine and selected representations of two normal modes[8,9]

This is evident for aromatic cycles or complex biomolecules, as in the case of nucleic acids, where fingerprint bands related to the nucleobases usually arise from the synchronous motion of many bonds. Typical examples are the combined stretching-bending vibrations in the 1240-1600 cm^{-1} region, which involve several atoms of the ring, as shown in Figure 1.2 for guanine.

Raman spectroscopy has been applied in several fields. At the molecular level it enables structural studies about symmetry and bond nature as well as molecule identification thanks to the unique fingerprint spectrum of each compound. As a consequence of the development of time resolved techniques such analysis can also be carried out on transition state structures allowing the unravelling of chemical reaction mechanisms.[10] Concerning solid-state research Raman spectroscopy is employed to retrieve information about the phonon density of states, which is reflected in the Raman spectrum, to characterize materials and to detect crystallographic orientations through the use of polarized light. Finally, Raman spectroscopy has gained greater and greater importance both in the medical field, where imaging combined to multivariate statistical analysis is exploited for diagnostic purposes[11], and in biochemistry for biomolecule structure determination, for example through Raman Optical Activity (ROA).[12]

1.3 Surface Enhanced Raman Scattering

The first Surface Enhanced Raman Scattering spectrum was collected by Fleischmann in 1974, while he was studying pyridine Raman signal after adsorption on a roughened silver electrode. Few years later, Van Duyne and Creighton first demonstrated that the huge enhancement of the Raman scattering of pyridine, which was estimated as 10^6, could not be only due to the high surface area of the supporting material.[13] The special optical properties of the substrate were instead suggested to enhance the local electric field felt by the adsorbed molecule. Subsequent research on the understanding of SERS mechanism led to the design of new experiments and to the development of better SERS substrates, which allowed, in 1997, to reach the single molecule detection level.[14,15] Raman effective cross sections as high as 10^{-15}-10^{-17} molecules/cm^2 were calculated in these studies. Such values are comparable or greater than fluorescence cross sections ($\sim 10^{-19}$) and from 14 to 11 orders of magnitude higher than normal (10^{-31}) or resonant (10^{-29}) Raman scattering ones. Although the enhancement values were slightly overestimated, due to the high cross section of the employed dyes[16], these studies revealed the great potential of SERS spectroscopy in the analytical field. The huge SERS enhancement is nowadays explained in terms of two contributions:[17]

-an electromagnetic (EM) enhancement, based on the amplification of the electric field felt by molecules adsorbed on nanostructured materials supporting Localized Surface Plasmons (LSPs). This mechanism accounts for up to 10 orders of magnitude of the signal increase;

-a chemical enhancement (CE), which only contributes up to 2 orders of magnitude to the overall enhancement, related to charge transfer transitions in the metal-molecule system.

Both mechanisms act on factors that determine the Raman scattering intensity. In the absence of surface enhancement, the Raman scattering intensity, $P^{RS}(\nu)$, can be written as:

$$P^{RS}(\nu) = N\, \sigma^{R}_{free} I(\nu_L) \tag{1.4}$$

where N is the number of molecules in the excited volume, σ^{R}_{free} is the Raman scattering cross section and $I(\nu_L)$ the incident laser intensity. If molecules are instead adsorbed on a metal nanoparticle (NP), the scattering phenomenon takes place in an enhanced local optical field, which can be taken into account through the introduction of laser and Raman scattering field enhancement factors, $A(\nu_L)$ and $A(\nu_{RS})$ (electromagnetic mechanism). Moreover, the molecules interacting with the metal surface can exhibit a larger Raman cross section than free ones, σ_{ads}, (chemical mechanism), resulting in the modified equation for the SERS scattering intensity:

$$P^{SERS}(\nu) = N' \, \sigma_{ads} \, |A(\nu_L)|^2 |A(\nu_{RS})|^2 I(\nu_L) \qquad (1.5)$$

where N' is the number of molecules contributing to the SERS effect.

Next sections will focus on the origin and on the factors influencing the effectiveness of each mechanism. Finally, a brief discussion about the experimental calculation of enhancement factors will be presented.

1.3.1 Electromagnetic enhancement mechanism

As introduced in the previous section, the electromagnetic enhancement depends on the existence of an amplified electric field at the metal surface in addition to the incident electromagnetic field. The origin of the enhanced field is found in the optical properties of the nanostructured material, which is able to support Localized Surface Plasmons (LSPs). Generally speaking, Surface Plasmons are collective oscillations of the free electrons of a metal under a homogenous positive background, which produce an oscillating electric field, whose propagation properties depend on the nature of the metal structure and on the surrounding matrix. For example, surface plasmons are supported by flat metal/dielectric interfaces in the form of Surface Plasmon Polaritons, longitudinal electron waves, which propagate along the interface, but are evanescently confined in a layer of thickness in the perpendicular direction. In case of metal nanoparticles, SPs appear instead as highly localized collective oscillations of valence electrons and can be usually excited from the far field at certain resonance frequencies. Next section will discuss the nature of Localized Surface Plasmon Resonances and their role in the EM enhancement.

1.3.1.1 Localized Surface Plasmon Resonances

A metal NP with a radius smaller than the incident radiation wavelength can be considered subjected to a uniform EM field. In this approximation an incident EM field drives highly localized collective oscillations of the whole electron cloud of the nanoparticle at a certain resonance frequency, producing a dipole charge density distribution near the surface. As a consequence, an induced dipole moment arises, whose sign is periodically changing at the incident field frequency (Figure 1.3(a)). Subsequently, the oscillating electrons radiate EM field at the frequency of their oscillation. The magnitude of the induced dipole depends on the polarizability of the particle, which

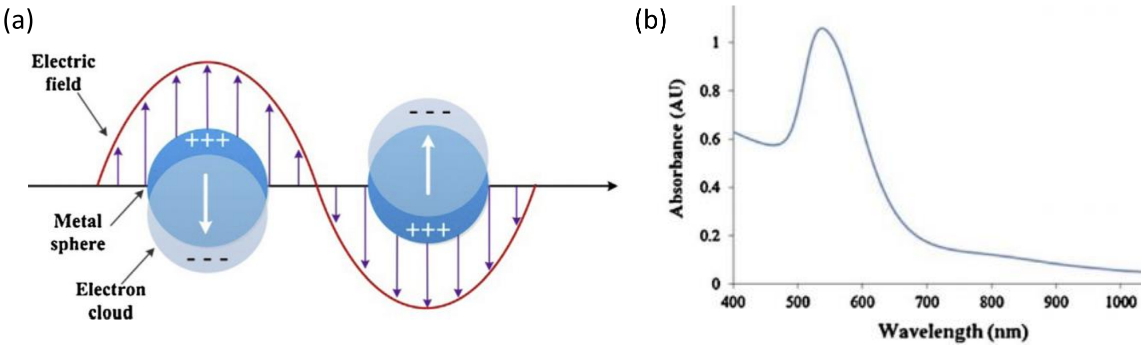

Figure 1.3. (a) Model of charge separation induced in a sub-wavelength metal particle in a homogenous EM field and (b) typical corresponding LSPR extinction spectrum[18]

for a sphere (under the electrostatic approximation) is:[19]

$$\alpha = 4\pi\varepsilon_0(r)^2\frac{\varepsilon-\varepsilon_0}{\varepsilon+2\varepsilon_0} \tag{1.6}$$

where r is the radius of the particle, ε_0, the dielectric constant of the surrounding matrix and ε the one of the metal particle. The dipolar resonance is achieved when $\varepsilon \approx -2\varepsilon_0$. It can be noticed that in case of resonant excitation of the system, α and therefore the amplitude of the field at the NP surface, is extremely high. Such condition can be exploited in SERS to boost the electromagnetic enhancement. This situation is referred as plasmonic resonant excitation of a SERS substrate.
Figure 1.3(b) shows a typical extinction spectrum for a spherical nanoparticle, corresponding to the dipole charge separation at the particle surface depicted in Figure 1.3(a). A single peak centred around the LSP resonance frequency is observed. However, two contributions, arising from the scattering and absorption of the particle, are convolved in this spectrum. These two mechanisms are competitive and both show a maximum in resonance conditions. Only scattering, however, is responsible for the SERS effect. As shown in Figure 1.4(a) the cross section related to each mechanism is variable, depending on the excitation wavelength and on the particle diameter. Such dependence can be exploited to favour the scattering phenomenon: for bigger particle sizes scattering is for example usually dominant, leading to higher enhancements. Plasmonic induced heating effects, which can be purposely exploited in thermo-plasmonics[20], but can be detrimental in SERS applications due to sample degradation, can also be minimized under these conditions.

Based on the introduced concepts, a simple model of the electromagnetic enhancement can be finally derived for a metallic nanoparticle with a complex dielectric constant, ε, and radius, r, surrounded by a medium of dielectric constant ε_0 (Figure 1.5). A molecule at a distance d from the nanoparticle surface is therefore subjected to an electromagnetic field E_M, which is the superposition of the incident field, E_0, and the field scattered by the dipole induced in the nanoparticle, E_{SP}.
The field enhancement factor is expressed as the ratio between the total field felt by the molecule and the incident one:

$$A(\nu) = \frac{E_M(\nu)}{E_0(\nu)} \sim \frac{\varepsilon-\varepsilon_0}{\varepsilon+2\varepsilon_0}\left(\frac{r}{r+d}\right)^3 \tag{1.7}$$

An analogous equation can be written for the enhancement factor of the Stokes and anti-Stokes scattered radiation. The combination of the two factors gives an overall enhancement for the

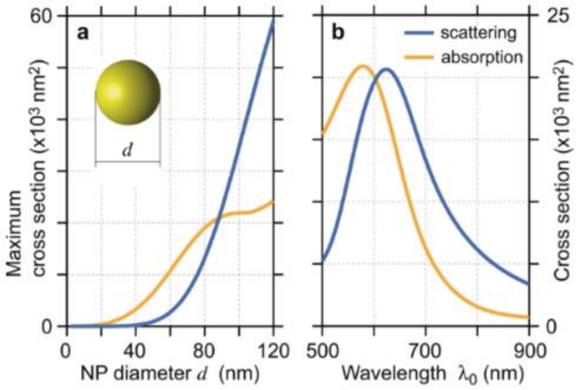

Figure 1.4. (a) Maximum absorption and scattering cross sections vs NP diameter and (b) Absorption and scattering cross section spectra for a gold nanosphere with *d*= 88 nm.[20]

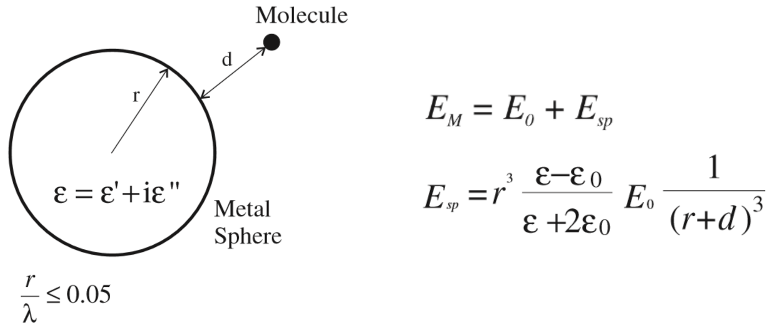

Figure 1.5. Schematic diagram of the EM enhancement mechanism[17]

Stokes signal power expressed by:

$$G(\nu) = \ |A(\nu_L)|^2 |A(\nu_S)|^2 \sim \left|\frac{\varepsilon(\nu_L) - \varepsilon_0}{\varepsilon(\nu_L) + 2\varepsilon_0}\right|^2 \left|\frac{\varepsilon(\nu_S) - \varepsilon_0}{\varepsilon(\nu_S) + 2\varepsilon_0}\right|^2 \left(\frac{r}{r+d}\right)^{12} \qquad (1.8)$$

It can be noticed from equation 1.8 that, although the electromagnetic mechanism does not require contact between the metal surface and the molecule, $G(\nu)$ decays as $(1/\,d)^{12}$ and only for very short d a strong electromagnetic enhancement can be foreseen. Moreover, an optimal enhancement occurs when the real part of the metal dielectric constant both at the laser and Raman scattering frequencies is close to -2ε_0. As discussed above, this represents the dipolar resonance condition of the particle, meaning that both the incident photon frequency and the Stokes scattered radiation need to be close to the plasmonic resonance frequency to maximize the enhancement. In this case, which is realistic for green and blue laser excitations only, the scattered power is directly proportional to the fourth power of the local field.[1]

As the EM mechanism depends on LSPRs excitation, understanding their behaviour moving from single spherical nanoparticles to differently shaped multiple particle systems, their interaction with surrounding materials and their resonances is essential to exploit them in SERS. These topics are discussed in the following sections.

1.3.1.1.1 LSPRs in single particle systems: size and shape effect

The dipole approximation of LSPs only applies to subwavelength nanoparticles. In case of larger diameters more complex models are required, which take into account the retardation effect of the electron cloud. The theory developed by Mie gives a good description of the effect of the size of the particle on the plasmonic properties, predicting a red shift of the resonance wavelength by increasing the particle diameter. Figure 1.6 shows this trend calculated for gold spheres in water.

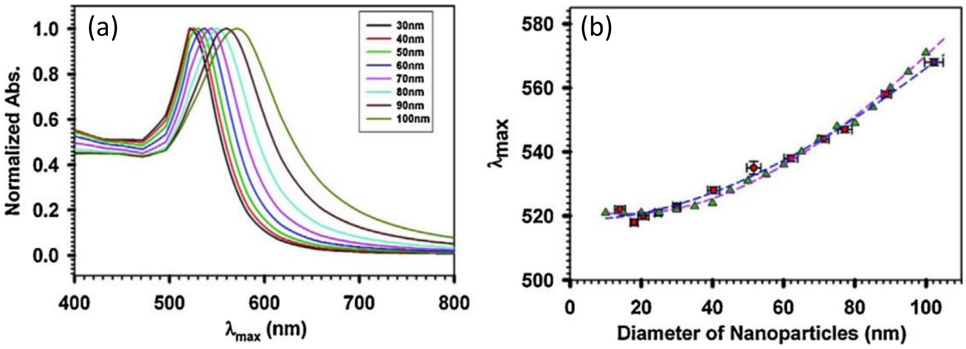

Figure 1.6. (a) Absorption spectra for gold particles in water at increasing diameters, calculated by the Mie theory; (b) Comparison of the absorption maximum vs NP diameter for the calculated (triangles) and experimental (squares) spectra.[21]

The maximum wavelength plotted against the particle diameter agrees well with the experimentally measured spectra (Figure 1.6(b)).

Computations for non-spherical geometries require numerical methods, as the Discrete Dipole Approximation (DDA), Finite-Difference Time-Domain or Finite Elements Method (FEM) calculations. In this case the shape of the nanoparticle influences the possible LSPRs, generating the splitting of the original plasmonic modes. Geometries presenting sharp edges and corners favour charge concentration in these parts of the structure. Very strong electric fields are, in fact, localized at the tips, as highlighted by the comparison of the calculated EM near-field distribution (shown as $|E|^2$ contours in Figure 1.7(a)) between spherical and cubic/pyramidal NPs.[22] Better SERS efficiencies are thus associated to these nanostructures, as well as to other multipointed geometries, like nanostars or dendrites.[23] The corresponding spectra show red shifted multiple resonances with respect to a spherical particle of the same volume. On the other hand, high aspect ratio nanostructures, like nanorods or nanowires, are characterized by two distinct resonances, due to the oscillation of electrons along the long and short axis (longitudinal and transversal plasmon modes), whose splitting increases with the aspect ratio of the rod (Figure 1.7(c)).

1.3.1.1.2 LSPs in multiple-particle systems: LSPRs coupling in hot-spots

Isolated nanoparticles are not usually applied in SERS. Indeed, first studies about single-molecule SERS revealed that these outstanding enhancements arose from particle dimers or trimers, showing complex multiply peaked extinction spectra.[24] Extraordinarily intense localized EM fields were also observed by near field microscopy[25] in inter-particle junctions, which were named hot-spots, confirming that the special enhancement derives from near field inter-particle interactions. Subsequently, SERS substrates were always designed in order to maximize hot-spot density, to exploit their huge enhancement efficiency. In detail, LSPRs of an isolated nanoparticle can be dramatically modified in terms of wavelength maximum, charge distribution and EM field confinement and intensity if a second nanoparticle is close enough. In this case the oscillating dipoles are able to interact giving rise to new resonances.

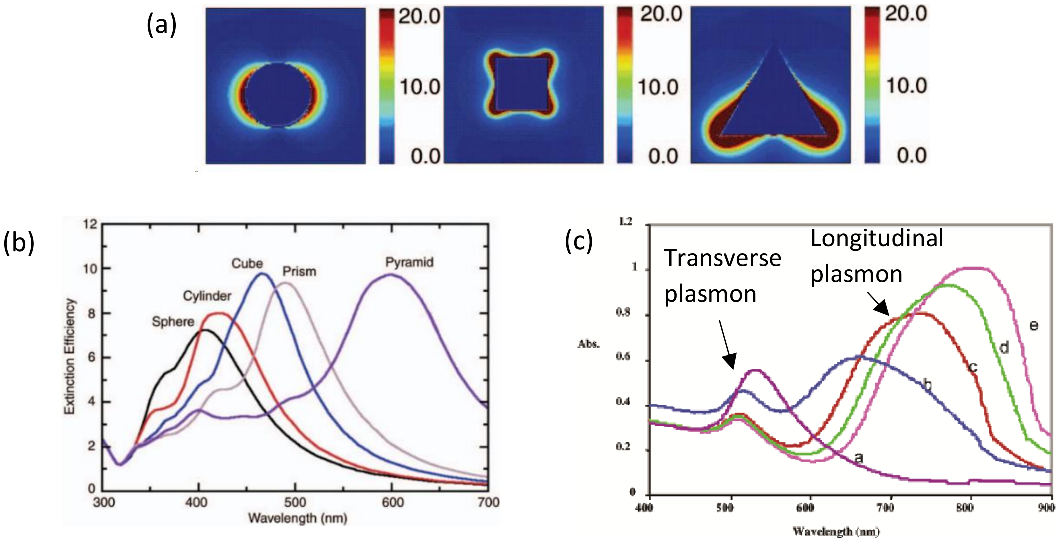

Figure 1.7. LSPRs in non-spherical geometries: (a) $|E|^2$contours (E is the electric field) for sphere, cube and pyramid, plotted for wavelengths corresponding to the plasmon peak in fig 1.7b; (b) extinction efficiency (cross section to effective area ratio) for the marked particle geometries;[22] (c) absorption spectra of gold nanorods with increasing aspect ratio: a) 1.35 ± 0.32, b) 1.95 ± 0.34, c) 3.06 ± 0.28, d) 3.50 ± 0.29, e) 4.42 ± 0.24;[26]

LSPRs in coupled nanoparticles can be discussed based on the “plasmon hybridization” model, which describes the plasmon modes of a complex nanostructure in terms of interactions between the plasmon resonances of its elementary components.[27] As the simplest coupled nanostructure, a dimer of spherical particles can be considered. Upon excitation with polarized light along the interparticle axis (that guarantees the maximum coupling), the splitting of the dipolar plasmon mode of each nanoparticle into a low-energy “bonding” mode and a higher-energy “antibonding” mode (Figure 8a) occurs, in analogy to the molecular orbital diagrams for diatomic molecules. As the lower-energy mode shows mutually aligned longitudinal dipoles, a large induced dipole and a strong coupling to the far field are expected (“bright” plasmon mode). The higher energy mode is characterized instead by antialigned dipoles. Due to the resulting absence of a net dipole moment, the antibonding mode is not able to couple to the far-field, being a so-called “dark” mode. As a consequence of the different coupling of the two modes to incident light, the far field optical properties of a plasmonic dimer are dictated by its bonding plasmon, resulting in an overall red shift of the resonance wavelength compared to the isolated particles. Moreover, if the gap between the NPs is so small that they are nearly touching, mixing between the dipolar states and all higher order modes of the neighboring nanoparticle occurs. This further hybridization provides an increased redshift of the bonding dimer mode with decreasing dimer separation. Despite the higher complexity, many of these principles can be transferred to multiple particle systems, although the effects of a change in the morphology on the plasmonic properties of the system can be only qualitatively described.

In analogy to the case of LSPs in single nanoparticles, hot spots can be resonantly excited. Depending on the excitation wavelength different plasmonic modes are activated, hence different electric field distributions around NP dimers are found. Figure 1.8 (b) shows the calculation of the EM near field for a 0.25 nm spaced dimer of gold nanocylinders, excited with light polarized along the interparticle axis at two different wavelengths: a dipolar mode (n=1) and a higher order mode (n=3) are excited at 714 and 592 nm, respectively, both displaying electric field focusing in the gap, but with different distributions, as highlighted by the zoom in the bottom of Figure 1.8 (b).[28] The confinement of the radiation in coupled plasmonic systems is very high, leading to huge EM fields concentrated in nanometric regions, well below the diffraction limit. As a general rule, the smaller the gap between the nanostructures, the higher the light focusing.

From the SERS point of view, the highest enhancements are therefore achieved for the smallest interparticle separations.[29] Figure 1.9 shows how the hot-spot geometrical parameters influence the maximum SERS enhancement in the gap between two spherical NPs. The huge sensitivity of the

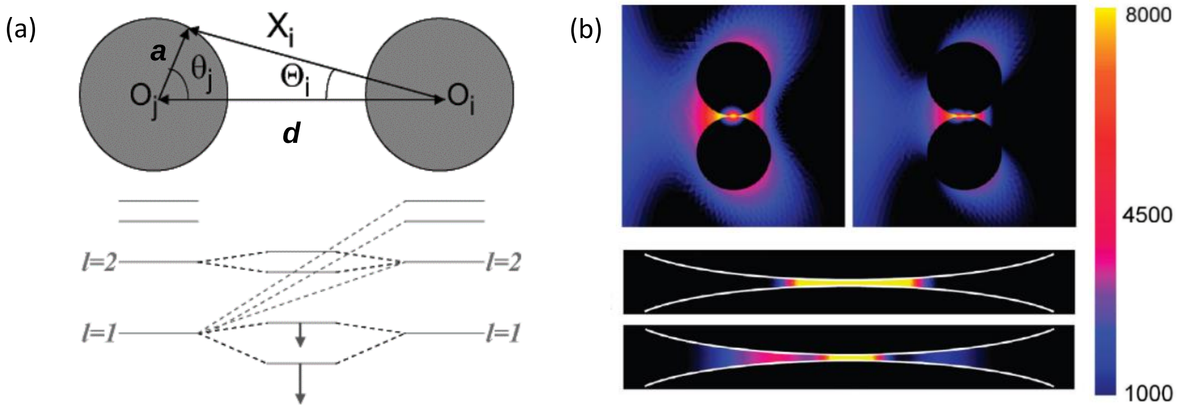

Figure 1.8. (a) Diagram of plasmon modes in a particle dimer according to the plasmon hybridization model.[30] (b) FEM simulation of $|E|^2/|E_0|^2$ contour profiles at 714 nm and 592 nm for gold dimers that are 50 nm in diameter with a 0.25 nm separation showing light focusing inside the gap.[28]

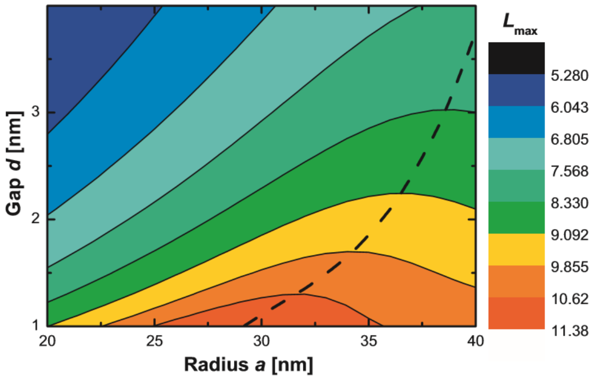

Figure 1.9. Maximum SERS effect (F_{max}) on the surface in the gap of a dimer as function of geometrical parameters (radius and gap). L = $\log_{10}(F_{max})$.[29]

EM enhancement to the hot spot geometrical features can be inferred from the map: the decrease of the gap, as well as the increase of particle size both contribute to the boost of the EM SERS effect by orders of magnitude, especially for very small inter-particle separations. In addition to the many theoretical evidences, experimental proofs of this trend have been provided by systematic variation of inter-particle gaps in dimers prepared by lithographic techniques[31] or by the assembly of core/shell SiO_2-silver nanocubes dimers with different thickness of the silica coating.[32]

Finally, it was recently demonstrated, that despite their inability to directly interact with light, dark plasmon modes can be involved in Raman scattering enhancement.[33] The far-field optical response of a SERS substrate, being a useful indication about its plasmonic properties, may not fully reflect their SERS response, because of the contribution of these non-radiative near-field modes.

1.3.1.1.3 Effect of surrounding matrixes or substrates

As it is evident from equation 1.6, which establishes that the resonant condition for LSPs also depends on the dielectric function of the surrounding medium, the presence of a coating over or of a substrate under the plasmonic nanostructures can affect their LSPRs significantly. For this reason, core- or multi-shell nanoparticles, both in case of metal/metal (i.e. Ag-Au particles) and metal/dielectric (i.e. silica embedded metal particles) structures, show interesting plasmonic properties and the tailoring of their coating is exploited to tune their LSPRs.[34–36] In general, a coating with a refractive index higher than air leads to a red-shift of the plasmonic resonances, as theoretically experimentally stated by several groups.[37,38] In a similar manner a substrate is able to dramatically change the plasmonic properties of the supported nanostructures. This situation always occurs for solid SERS platforms. In general, a NP placed on a support is attracted to it, because of the image charge induced in the substrate, regardless of its nature.[39] Figure 1.10 illustrates this mechanism for the dipolar charge distribution in a nanoparticle over a dielectric surface for p-polarized and s-polarized incident light. Although dielectrics usually show weak image charges, this introduces a symmetry breaking in the system, which causes a splitting of the original plasmonic modes of the NP. Concerning the p-polarization, in which the NP-substrate coupling is higher, the mixing of the dipolar mode with multipolar modes is also possible and can result in the appearance of higher order hybridized plasmon resonances in the spectrum, as well as in the presence of dark plasmonic modes. The image charge for dielectrics was calculated to be screened by factor $(1-\varepsilon)/(1+\varepsilon)$, where ε is the permittivity of the substrate: as a consequence, materials with higher permittivity give rise to a stronger image charge and hence a stronger interaction. If a metal substrate is considered, in addition to the described phenomenon, its SPs interact with the

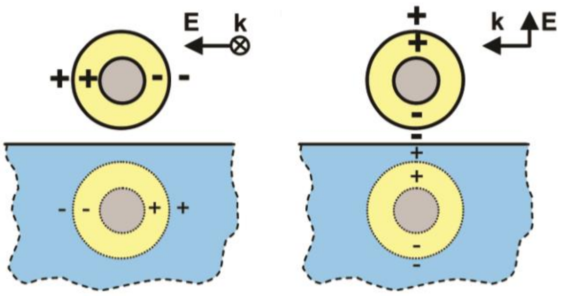

Figure 1.10. Image charge induction in a dielectric substrate due to the excitation of the dipolar LSP of the metal NPs under p- and s-polarized radiation.[39]

LSPRs of the NPs, generating an effect that shares similarities with the coupling in a dimer of nanoparticles. An extra SERS enhancement can be attained by both these near-field interactions, due to particular EM field distributions and concentrations.

1.2.3 Chemical enhancement mechanism

The chemical enhancement mechanism acts in addition to the EM one, when molecules are adsorbed on the nanostructured surface. Its contribution, which is estimated to be around one or two orders of magnitude, was first inferred by the strong dependence of the magnitude of SERS enhancement on the analysed molecule.[17] Moreover, SERS spectra are usually different with respect to normal Raman ones. In particular, it was noticed that some Raman modes are preferentially enhanced in SERS spectra, leading to a modification in the relative Raman band intensities, and that forbidden bands can occur. This happens together with a shift in the frequencies of Raman modes which is ascribed to adsorption and metal-molecule interaction. Examples are the SERS spectrum of C_6F_6 (Figure 1.11 (a)), in which the C-F symmetric breathing vibration is the dominant feature, while in the ordinary Raman spectra is among the weaker bands[13] or the 4-mercaptobenzoic acid one[40], where the mode at 1075 cm^{-1}, arising from the ring breathing coupled to the C-S stretching is clearly shifted due to the semi-covalent interaction of the sulphur atom to the silver surface (Figure 1.11 (b)).

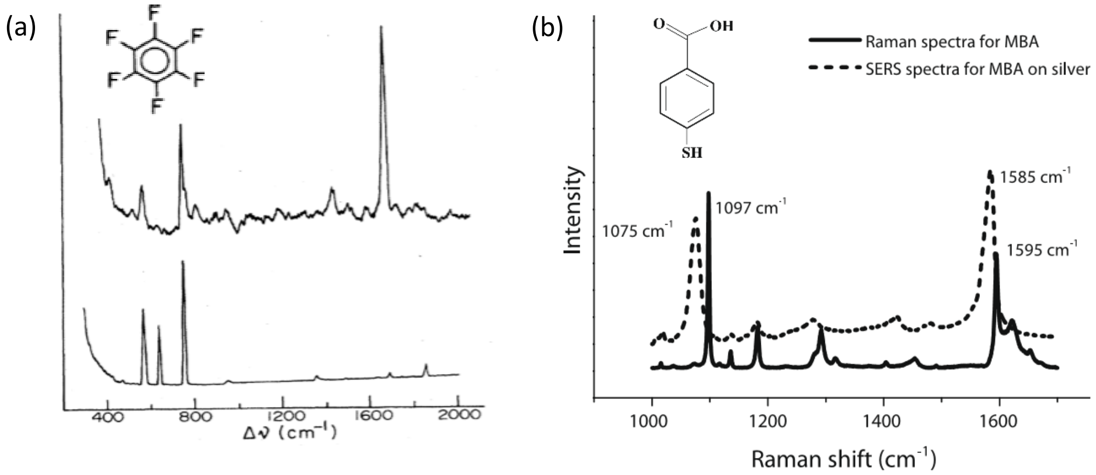

Figure 1.11 (a) C_6F_6 Raman (bottom) and SERS (top) spectrum.[13] (b) 4-MBA Raman (solid line) and SERS (dashed line) spectrum.[40]

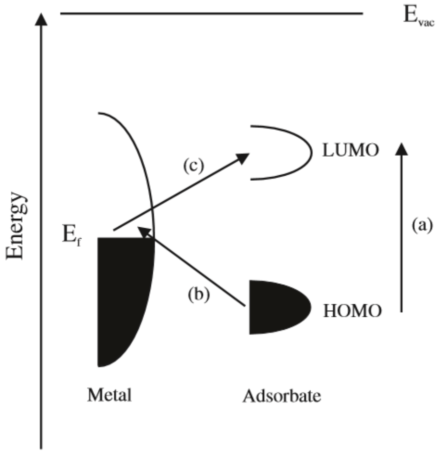

Figure 1.12. Scheme of possible resonant Raman pathways in a metal-molecule system.[17]

Several mechanisms were suggested to explain the CE, including the formation of metal-molecule complexes with enhanced Raman cross-sections, due to molecule polarizability modification upon adsorption, or the appearance of new electronic resonances. Figure 1.12 illustrates three electronic resonance processes enabled in a metal-molecule system, where the highest occupied molecular orbital (HOMO) and the lowest unoccupied molecular orbital (LUMO) energies are approximately symmetric relative to the Fermi level of the metal. Concerning pathway a, the resonance is possible due to the broadening of molecular electronic levels, while pathways b and c represent charge transfer transitions between the Fermi level of the metal and the HOMO/LUMO orbitals of the molecule. The latter effect has been probed in several studies, which demonstrate the potential dependent SERS enhancement factor for molecules adsorbed on electrodes or in nano-gaps.[41,42] Changes in the enhancement are attributed to the shift of the metal Fermi level at the different applied potentials. Further support of this mechanism is provided by time resolved single-molecule experiments, in which the fluctuation of Rhodamine 6G bands and the variation of their relative intensities were observed and interpreted as the result of the lateral diffusion of the dye on the heterogeneous adsorption sites (characterized by different local work functions associated to steps or point defects) on the nanoparticle surface.[43] Finally, computational studies on the electronic structure of molecules adsorbed on metal clusters are a useful tool in order to distinguish the contribution of the different CE mechanisms.[44]

1.2.3 Experimental Enhancement Factor (EF) calculation

As discussed above, the observed SERS enhancement depends on the EM and CE mechanism acting synergistically. However, how to extract a significant value, which gives an estimation of the SERS efficiency of a real substrate is still under debate. Several factors should be taken into account:[45]

1) The non-SERS properties of the probes, in particular their Raman cross-sections, have to be included in the definition;
2) The possible influence of the specific experimental conditions should be carefully evaluated and minimized;
3) The average SERS EFs and SM (single molecule)-SERS EFs have to be distinguished; the first represents the average SERS properties of a substrate, while the second expresses the local enhancement experienced by a molecule in a specific position of the substrate. SM-SERS EFs can be order of magnitude higher than the average EF, especially if hot-spots are considered.

The most widespread definition of average EF is:

$$EF = \frac{I_{SERS}/N_{Surf}}{I_{RS}/N_{Vol}}$$

which is the ratio between the SERS and Raman intensity, normalized to the number of molecules contributing to the signal: N_{Surf}, the number of adsorbed molecules in the scattering volume for SERS and N_{Vol}, the average number of molecules in the probed volume for the Raman spectrum. More specific equations, which include a rigorous definition of N_{Surf} and N_{Vol} have been developed. Anyway, all of them often require the precise estimation of morphological properties, that is rarely feasible for real SERS substrates. An approximation can be given by the analytical EF (AEF):

$$AEF = \frac{I_{SERS}/C_{SERS}}{I_{RS}/C_{RS}}$$

In this case the concentrations of the probed solutions are used for the normalization. The AEF neglects however the adsorption properties of the analyte, which is in some cases taken into account by introducing an adsorption coefficient[46], and the peculiarities of the substrate, such as porosity or specific wetting behaviours. An alternative way to roughly express the average enhancement factor, suited for the analysis of solid SERS substrates, is the External Amplified Raman Efficiency (EARE).[47] This value is calculated through the ratio of the lowest concentration of an analyte detectable on the bare support to its lowest concentration that can be observed on the metal coated one:

$$EARE = \frac{C_{min,\ bare\ support}}{C_{min,\ metal-coated\ support}}$$

The same surface is therefore investigated and provided that the incubation or drop-spot conditions are fixed, this number enables a good comparison between different substrates. Attention must be payed that particular electronic resonance conditions can give rise to extra enhancement of the SERS cross-section with respect to the Raman one, which cannot be considered in the EARE. Hence, it is preferable to compare substrates under electronic off-resonance excitation. The EARE will be employed in the experimental part of the thesis, in order to evaluate the enhancement efficiency of the probed SERS solid substrates.

Chapter 2

SERS substrates

2.1 Introduction

The previous chapter has introduced the fundamental concepts of plasmonics needed for a rational SERS substrate design. In a simplified picture, a SERS substrate should maximize the hot-spot density and show at least one plasmonic resonance which matches the excitation wavelength in order to achieve high SERS efficiencies. However, other requirements have to be met in case of real applications: good uniformity (low point-to-point variability) and reproducibility (low substrate-to-substrate variability) together with an easy and low cost fabrication are necessary, especially for quantitative analysis. Although advances in nanotechnology have enabled an increasing control over the synthesis of plasmonic nanostructures, no substrate which completely satisfies both properties is available.[48] The main issue concerns with the huge sensitivity of SERS enhancement to hot-spots geometrical features, leading to a high variability of the SERS signal in efficient SERS substrates. Finally, in case of biological applications the stability of substrates in harsh physiological conditions (high salt concentrations, presence of complex and potentially chemically aggressive matrixes) should be considered. This chapter aims to an introduction to the main fabrication techniques of SERS substrates and their applications in biosensing. The first part will discuss wet and solid state SERS systems with a special focus on the in situ synthesis of plasmonic nanoparticles on porous silicon substrates. The second part is devoted to biotechnological applications, including an overview of the lab-on-chip developments in these fields thanks to ink-jet printing technology and microfluidic integration.

2.2 SERS substrates fabrication methods

SERS substrates are commonly divided in two categories: solution-based systems, which are mainly colloids of plasmonic nanoparticles, and solid platforms, which can be either produced by bottom-up (vacuum deposition techniques, immobilization of colloidal NPs or in-situ NPs growth) or top-down (nanolithography or nanoimprint) techniques. Colloids are usually chosen for their high SERS efficiency (in their aggregated form) and their versatile and easily accessible synthetic routes. However, reproducibility and time stability issues exist.[49] Solid SERS substrates allow instead the achievement of a time-stable spatial arrangement and therefore of stable SERS properties. While bottom-up techniques are almost always suited for large area production, nanolithography methods are mainly limited to the study of the SERS phenomenon due to the high time and cost requirements.[50] A brief review about the main SERS substrates typologies is provided in the followings.

2.2.1 Colloidal systems

Plasmonic Au and Ag colloids can be produced by wet chemistry with an always increasing control over shape, size and composition. NPs synthesis relies on the reduction of a metal precursor, usually a soluble metal salt, which is co-precipitated in presence of a reducing agent.[51] Thermal or ultra-sound decomposition methods can be also employed. During all of these synthesis a nucleation and growth process is responsible for NPs formation: atoms (already reduced or in complex with the

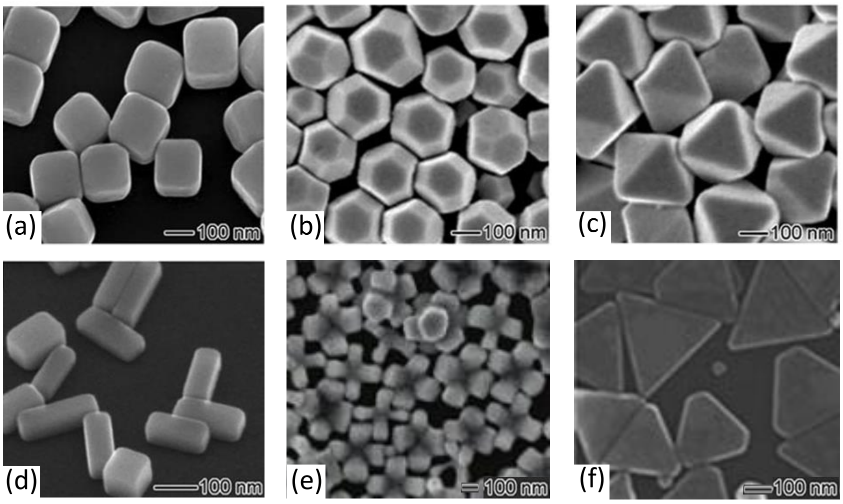

Figure 2.1. Shape control in silver nanocolloids. Electron microscopy images of: a) nanocubes prepared in ethylene glycol with PVP as a capping agent; b) truncated octahedra prepared in 1,5-pentanediol in presence of PVP and Cu^{2+} ions; c) octahedra obtained by further growth of the truncated ones at longer reaction times; d) nanobars prepared in ethylene glycol in the presence of PVP and Br^{-} e) octapods prepared by etching of silver octahedra in NH_4OH/H_2O_2 mixtures; f) nanoplates synthesized in water with PVP as a reductant.[51,52]

reducing agent) in supersaturation conditions, initially aggregate into nuclei which then start to increase their dimension by atomic addition or agglomeration. Single or twinned nanocrystals can appear at this stage, determining the possible final shape of the nanoparticles.[51] One of the most widespread methods for the preparation of silver colloids is the Lee and Meisel's one[53], which exploits the reduction of silver nitrate by sodium citrate in aqueous medium. The synthesized particles show a negatively charged citrate monolayer adsorbed on their surface, which is able to stabilize the suspension due to the repulsion between the charged particles. Other typical reducing agents are $NaBH_4$[54], hydroxylamine[55] or polyols[56]. Lee and Meisel's colloids show a quite wide size distribution and mainly spherical NPs. Homogeneously sized colloids are however achieved by the separation of the nucleation and growth steps[46], which can be accomplished either by generating the seeds separately and then adding them to a growth solution or by the fine tuning of temperatures, reagents concentrations and ratio, choice of solvent mixtures and presence of additives.[57] Moreover, non spherical nanoparticles can be produced by the addition of capping polymers or surfactants which preferentially adsorb on certain crystal facets, favouring the growth of the free ones or acting as templates. This is the case for gold nanorods, where CTAB (cetyl-trimethyl ammonium bromide) directs the one dimensional growth of the nanostructures in the presence of silver catalysing ions[58], and of many nanoplates with triangular or hexagonal shape.[59] Silver nanocubes were instead prepared in the presence of PVP (Polyvinylpyrrolidone).[60] Nanostars and other complex geometries have been recently obtained by the addition of unconventional template agents to the reaction mixture, such as protoporphyrin IX[61], while pointed particles were also obtained by anisotropic etching of octahedra in NH_4OH/H_2O_2 mixtures.[52] Except for these nanoparticles, which can show huge enhancements due to the richness of sharp edges and corners, well-dispersed nanoparticles usually do not provide very high SERS efficiencies. Colloids have to be purposely aggregated to form clusters where the Raman signal is boosted in the hot spots.[62] The aggregation can be driven by salts, such as NaCl, $MgSO_4$ or $NaNO_3$, which are able to screen the negative charges of the nanoparticles, reducing the electrostatic repulsion between them, or by the analytes themselves (for example several dyes are positively charged).[63,64] The main drawbacks of aggregated colloids are however the poor reproducibility of their preparation and the reduced stability over time. In the recent years, some strategies have been developed for a controlled aggregation of colloidal nanoparticles, which involve the functionalization of their surface with polymers[65] or linkers, such as DNA strands[66] and thiols, but applications in SERS spectroscopy is still limited because of the coating hindering an easy access of the analyte to the metal surface. In a different approach, $Fe(NO_3)_3$ has been instead used to induce the etching of silver nanocubes and the subsequent assembly to a stable suspension of nanosphere dimers in presence of PVP and ethanol.[67]

Besides chemical approaches, laser ablation is a promising techniques for the production of plasmonic nanoparticles. Colloids can be obtained without the need of chemical reactants or stabilizers in several pure solvents by focusing a pulse-laser radiation onto a metal plate immersed in a vessel. The laser triggers the photoionization of the surface atoms which form a plasma plume near the substrate. During the cooling of the plume, nucleation and growth of nanoparticles can occur.[68] Coalescence of nuclei directly extracted from the metal plate is also possible.[69] Due to the extreme temperatures and pressures, non-equilibrium compounds, such as alloys of plasmonic and catalytic metals, can be produced by this method, highlighting the potential of laser ablation in the synthesis of multifunctional nanoparticles.[70]

2.2.2 Solid platforms

The first SERS spectra were acquired on roughened electrodes, which actually belong to the class of the solid SERS substrates. Their production was based on electrochemical oxidation reduction cycles (EC-ORC) of metal surfaces. In the first half of the cycle an applied potential triggered both the oxidation of the metal to soluble compounds and the formation of oxidized surface complexes. In a second step a reducing potential was applied and oxidized metal species were again reduced onto the electrode, resulting in a nanostructuration of its surface.[71] Roughened electrodes showed however a huge variability in their morphological features, with protrusions ranging from 25 to 500 nm, and hence in the enhancement factor. Nowadays, many techniques are available for the fabrication of solid SERS substrates, which are usually classified in three main categories:[49]

1) nanostructures obtained by lithographic techniques;

2) substrates obtained by template-based techniques;

3) nanoparticles immobilized on a substrate.

Among them, nanolitography is the technique of choice for the fabrication of reproducible nanostructures. Although it shows few applications for analytical purposes, it has been widely employed in several fundamental studies because of the fine control over the produced structures. Electron Beam Lithography (EBL) is the most common nanolithographic technique for the fabrication of nanostructures with specific shapes, sizes and small inter-particle spacing.[49] An electron beam is focused on a polymeric resist (positive or negative), previously cast on a substrate, to modify its solubility according to the desired pattern. As shown in Figure 2.3 for a polymethyl methacrylates (PMMA) positive resist, after resist development metal can be directly deposited on the obtained structure, followed by resist removal, or a further step of Reactive Ion Etching (RIE) can be carried out to produce a 3D structuration of the substrate before resist lift-off and the evaporation of a metal film.[72] Structures below 10 nm can be produced by EBL.[50] UV-laser irradiation or Focused Ion Beam (FIB) also enable the patterning of the resist, either by direct writing or indirectly with the assistance of a mold, but with lower resolution. The fabrication of highly ordered arrays allowed to study the effect of the inter-particle spacing[73] and gap geometry[31]

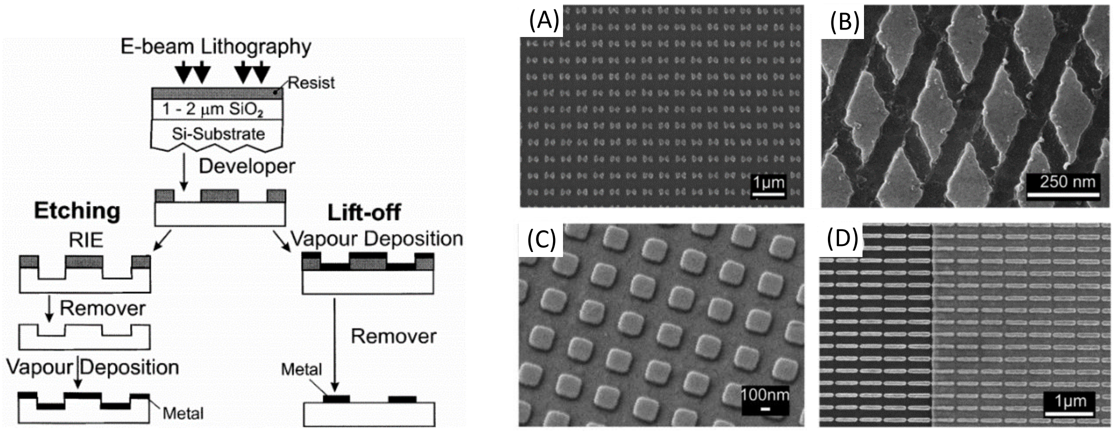

(a) (b)

Figure 2.2 (a) Scheme of two possible nanolitographic pathways: etching of the masked substrate (left) and lift-off (right)[72] (b) Examples of plasmonic nanostructures obtained by EBL: (A) Bowtie nanoantennas; (B) gold nanorhombs produced by EBL and RIE etching processes; (C) silver nanosquares; (D) SEIRA structures produced by lift-off EBL.[50]

on the SERS enhancement and the influence of light polarization in anisotropic nanostructures.[31,73,74] However, the long production time and high costs discourage the use of nanolithography in real applications.

A different approach consists in the preparation of silicon or quartz molds by nanolithography. The pattern is then transferred onto a resist by imprinting. After curing, the SERS active metal is deposited onto the patterned surface, which is then removed. Ordered patterns are in this way attained at a lower cost, but usually show quite high inter-particle spacing and therefore low enhancement factors.

A lower cost method to produce ordered SERS substrates consists in the template approach, in which the metal is deposited in or/on a matrix with a well-defined geometry. Anodic Alumina Oxide (AAO) templates and nanosphere lithography belong to this category. The fabricated arrays usually display clean surfaces, due to the absence of contaminations by surfactants or other chemical reagents. AAO substrates exploit alumina frameworks electrochemically etched in acidic environment which are characterized by a honeycomb close packed arrangement of pores (with diameters ranging from 15 to 150 nm).[75] The metal can be deposited into the nanopores by electroless, AC or DC plating. The template may be partially dissolved in phosphoric acid, resulting in well-ordered nanowire or nanotube arrays, or completely removed, releasing the nanostructures to form highly SERS active collapsed nanowires bundles.[76] Recently, AAO templates were also used as molds to imprint PET (polyethylene terephthalate) substrates, which were afterwards coated with a thin gold film, resulting in ordered arrays of gold nanocaps.[77] Despite the low cost, tunability and easy production of AAO substrates, some issues persist, related to the nanowire spacing, which is hardly lower than 5 nm when ordered arrays are required. The template structure is in fact damaged when the pore walls are too thin.

In Nanosphere Lithography (NSL) colloidal nanoparticles (e.g. polystyrene nanospheres) are self-assembled as a 2D monolayer on a substrate by capillary forces and exploited as a template or mask for the subsequent metal deposition. Three different nanostructure typologies are obtained depending on the thickness of the metal layer and on the deposition technique[78], as illustrated in Figure 2.3. Physical vapour deposition yields metal films over nanospheres (M-FON). If the polymeric nanoparticles are then removed by sonication triangular shaped nanostructures are left

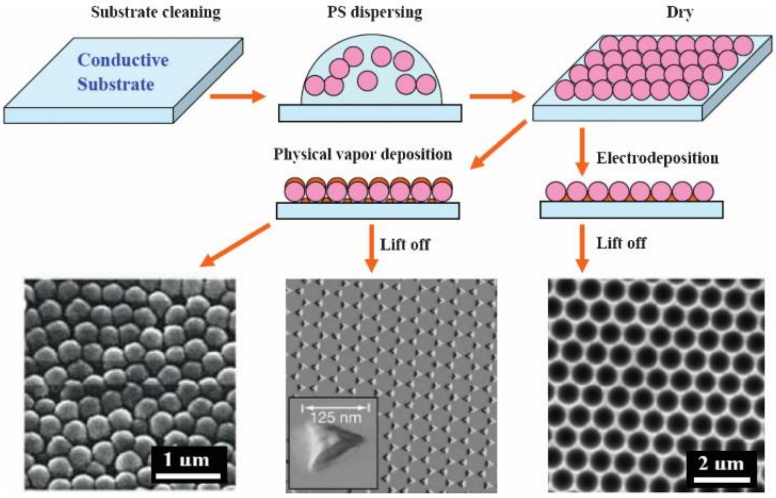

Figure 2.3. Scheme of the nanosphere lithography process and three possible resulting structures. From left to right: metal films over nanospheres (M-FON), nanoprisms array, segment sphere voids (SSV) array.[78]

on the surface in correspondence of the interstices between the spheres. In case of electrodeposition, followed by the lift-off of the self-assembled monolayer, regular arrays of sphere voids (segment sphere voids, SSV) with hexagonal geometry are instead formed. Strategies such as the use of multilayer masks or the variation of the deposition angle can be employed to further tune the nanoparticle structural motif. Nanostructures in the 20-1000 nm range can be prepared with a very good control of their size and inter-particle spacing. Due to the easy tuning of these features NSL prepared substrates have been applied to study the size-dependent plasmonic properties of Ag nanoparticles and the effect of the local, external dielectric environment.[79]

Some groups have attempted the deposition of metal nanostructures without the help of templates, producing uniform SERS substrates. Oblique Angle Deposition provides ordered arrays of silver nanorods with high SERS efficiency thanks to the small rod to rod distances.[80] Evaporation of silver atoms is however performed by means of an electron beam. Low cost DC sputtering has also been demonstrated to be suitable for the deposition of homogeneously sized metal nanoislands on polymeric/elastomeric planar surfaces.[81]

Immobilization of nanoparticles on solid surfaces was initially tested in order to overcome the poor stability and aggregation control of colloidal systems. This approach was first described by Freeman et al. in 1995. Their substrate consisted in a well-ordered monolayer of NPs bound to a polymer-coated glass slide. Such procedure is referred as the self-assembly method. NPs immobilization can be either performed by chemical approaches or by electrostatic interactions. In the first case, bifunctional ligands are employed. These molecules can be anchored to an activated surface (e.g. covered by hydroxyls due to a piranha treatment) by means of one functional group, leaving the second one, typically a thiol or an amine group, exposed for the binding of the metal NPs. In fact, most of the functionalizations of glass, quartz or silicon supports are performed by exploitation of the silane chemistry.[49] At the same time, the tailoring of the nanoparticle-substrate spacing is possible thanks to the introduction of linkers of different length by EDC-NHS coupling of different amines and carboxylic groups. The controlled assembly of 3D structures has been also demonstrated, by the addition of successive layers (Figure 2.4 (a)), providing higher enhancement factors than the traditional 2D platforms.[82] A similar method was also employed to fabricate SERS

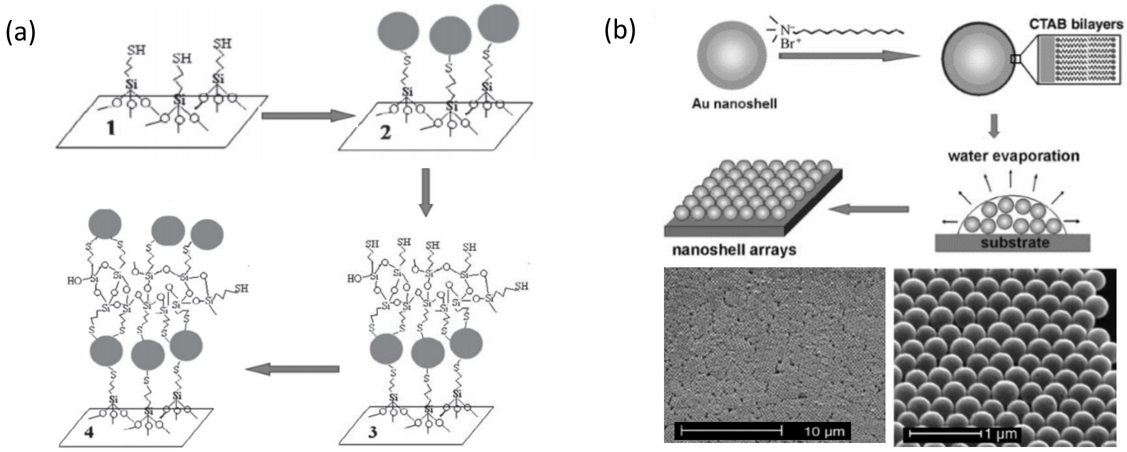

Figure 2.4 (a) Preparation of self-assembled multiple layers: 1) MPTMS (mercapto propyl tetraoxysilane) functionalization of a clean glass slide; 2) capture of the NPs from the solution through the thiol groups; 3) dipping in a MPTMS sol-gel; 4) second layer immobilization.[82] (b) Scheme of electrostatic self-assembly of CTAB capped Au nanoshells by capillary forces and SEM images of the prepared array on a silicon substrate.[83]

active optical fiber tips.[84] In the electrostatic approach, the assembly of bare or capped metal NPs on the solid support is mediated by the interaction with polymers[85] or biomolecules.[86]
Negative DNA networks on mica have been for example employed to adsorb CTAB capped silver nanoparticles, achieving ordered SERS substrates.[87] Besides the mentioned approaches capillary forces are also employed to drive the self-assembly. Nanoparticles can organize in close packed monolayers during the drying of a droplet if properly capped with surfactants that prevent their uncontrolled aggregation (Figure 2.4 (b)).[83] Moreover, the self-assembly can be performed in the liquid phase, followed by transfer of the already formed monolayer onto the support. This is the principle of the Langmuir-Blodgett technique, where the particle film is created at the interface between water and an immiscible organic solvent containing the dispersed NPs. The applied pressure controls the density of the monolayer and very homogenous films can be prepared.[88]
The SERS properties of self-assembled substrates can be tuned by varying the particle and support chemical nature, the substrate activation procedure or the incubation time in the NPs solution. Quite compact monolayers, showing a homogenous enhancement factor (RSD in the 5-20%) over large areas can be obtained. The enhancement factors usually range between 10^4-10^7.[49]

In alternative to the immobilization of pre-synthesized nanoparticles, the direct growth of nanostructures on the solid substrates has also been explored. Seeds can be anchored to a surface and then enlarged until the inter-particle gap reaches the desired size. Furthermore, the substrate can be immersed in a solution of a metal precursor and a reducing agent which react to form nanoparticles at solid/liquid interface.[89] Silver nitrate and HF in presence of silicon substrates have been employed for these purposes.[90] The intrinsic reactivity of a surface can also be exploited. Some examples are the synthesis of silver flower-like nanostructures, obtained by dipping polyaniline substrates in silver nitrate/lactic acid solutions[91] or the in situ reduction of $HAuCl_4$ onto PDMS slices driven by the residual curing agent.[92] This principle is also exploited for porous silicon based SERS substrates, where copper, silver and gold nanoparticles can be synthesized thanks to the reducing properties of its freshly etched surface.[93] In particular, silvered porous silicon (Ag-pSi) has been demonstrated a highly efficient, versatile and easily prepared SERS substrate. As far as they represent the starting point of the nanostructure developed in this thesis, the next section will be

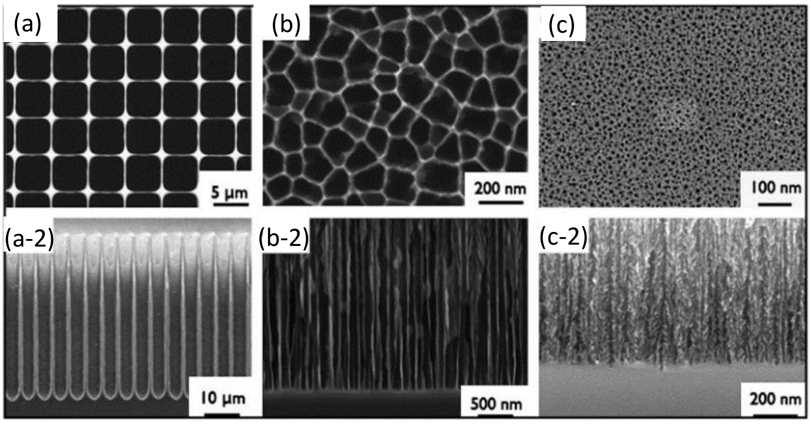

Figure 2.5. SEM top-view and cross sections (-2) of different pore morphologies achievable by variation of the starting wafer material and etching conditions: (a) ordered macropores (b) medium-sized pores (c) sponge-like mesoporous silicon.[94]

devoted to an introduction of Ag-pSi substrates.

2.2.2.1 Porous silicon SERS substrates

Porous silicon is an extremely versatile material, that, after its discovery by A. Ulhir in 1956[95], has found applications in numerous fields for its electrical, optical, morphological and chemical properties. Although different preparation methods have been developed, the electrochemical anodization of doped silicon wafers in HF solutions is the most common approach. Si etching is performed in a Teflon or HF resistant material cell, showing an aperture from which an area of the wafer is exposed to the electrolyte. A constant current density (galvanostatic regime) is usually applied, during the anodization, between silicon (the working electrode) and a platinum foil (counter-electrode), which drives an electrochemical reaction at the silicon/electrolyte interface. The proposed mechanism involves two steps:[96]

1) $Si + 2F^- + 2h^+ \rightarrow [SiF_2]$
2) $[SiF_2] + 4F^- + 2H^+ \rightarrow SiF_6^{2-} + H_2$

During the first reaction, holes (h^+) from the valence band are attracted to the surface, causing Si oxidation to the +2 state. Subsequently, $[SiF_2]$ species readily react with water protons, as it can be noticed by the evolution of hydrogen at the anode, and Si is further oxidized to the +4 state.[96] Contrary to the so called electropolishing reaction, in which Si is completely dissolved at high applied voltage, only 2 of 4 electrons are involved in the electrochemical etching. In this 2-electron anodization a porous structure is formed, where the pores tend to propagate preferentially along the <100> direction of the wafer. Depending on the type and amount of doping of the starting wafer and on the reaction conditions (HF concentration, supplied current density, temperature, presence of surfactants, solvent mixtures) different pore morphologies are obtained, spanning from vertically aligned macropores to sponge-like meso- and microporous silicon, as shown in Figure 2.5. A fine control over the important features of the porous silicon layer, such as its porosity (volume fraction of voids) and thickness is achievable through the tuning of the etching conditions.[97] Since the etching only proceeds at the pore tips, multilayers with periodically varying properties can be prepared, which are exploited as photonic crystal sensors.[98] Due to the porosification process in HF, porous silicon is characterized by a unique surface chemistry. As it was inferred by FT-IR spectroscopy, silicon hydride species in the $Si\text{-}H_x$ form (x=1,2,3) cover the walls of the freshly prepared porous silicon. Such groups are responsible of its high reactivity towards oxidizing

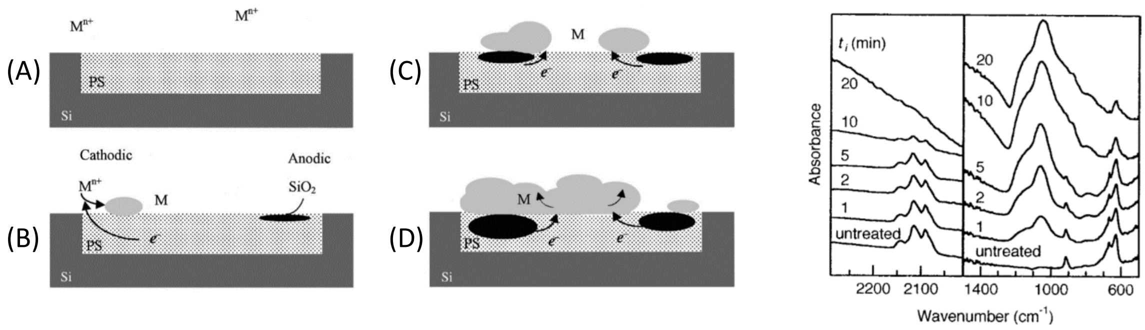

(a) (b)

Figure 2.6. (a) Main steps of metal NPs growth by immersion plating of pSi in metal salts solutions.[93] (b) FT-IR spectra of pSi acquired at increasing plating time in $CuCl_2$. Bottom spectrum is acquired before the immersion (untreated). [99]

agents.[100] Moreover, they are involved in the spontaneous deposition of noble metals onto its surface.[99] Indeed, if porous silicon is immersed into Cu^{2+}, Ag^{+}, Au^{3+} or Pd^{2+} salts solutions, it is able to drive their reduction to metallic nanoparticles or rough films. The mechanism of the so-called immersion plating was first explained by Ogata et al. who suggested that the reduction of metal cations occurs in combination with the oxidation of Si-H_x species, according to the following reaction:[93]

$$SiH_{x\,surf} + 2H_2O + (4+x)\,AgNO_3 \rightarrow SiO_2 + (4+x)\,HNO_3 + (4+x)\,Ag$$

The scheme in Figure 2.5 illustrates the deposition steps: at the beginning metal nuclei form on those surface sites characterized by higher reactivity, such as dangling bonds (Figure 2.5(a) A-B). Oxidized porous silicon can be already detected in this early stage of the plating. Electrons are then continuously supplied by the enlargement of oxidized regions, while the initially grown nuclei behave as local cathodes, where new ions are reduced according to a local cell mechanism (Figure 2.5(a) C). Under certain conditions, nanoparticle coalescence occurs, resulting in the formation of metal films (Figure 2.5(a) D).[101] FT-IR transmission spectra in Figure 2.5 (b) witness the depletion of Si-H_x stretching related peaks around 2100 cm^{-1} and the appearance and intensity increase of the Si-O-Si bands at 1100 cm^{-1} as the reaction proceeds.

Although the deposition of different metals has been studied, silver nanostructures are by far the most interesting ones for SERS purposes, due to the higher enhancement. While Chan et al. demonstrated the first pSi SERS substrate prepared by impregnation and thermal decomposition of a silver precursor in 2003[102], Sailor's group first reported the application of silver plated pSi as SERS substrate one year later.[103] Since then, immersion plating has become the most studied

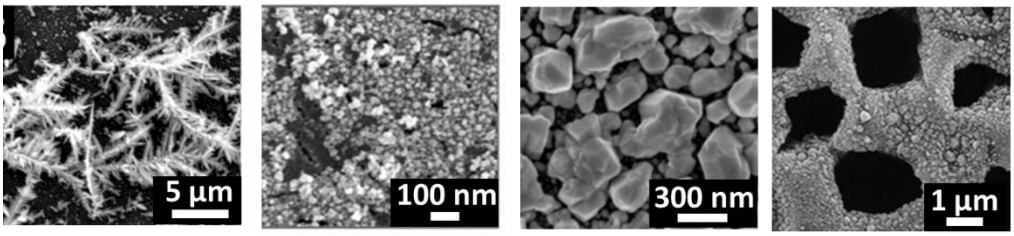

(a) (b) (c) (d)

Figure 2.7 SEM images of silver-coated pSi showing the wide range of achievable NPs morphologies: (a) Ag-dendrites[104], (b) high density small AgNPs[105] and (c) sharp-edges AgNPs on mesoporous silicon; (d) AgNPs grown on macroporous silicon as a template.[106]

fabrication technique because of the number of parameters that can be varied to tune the SERS response of the substrate. Figure 2.7 collects electron microscopy images of Ag-pSi samples showing the completely different morphologies which can be obtained depending on the choice of the silicon doping, pore morphology, porosity, thickness and reaction conditions.

The Giorgis' group has devoted much work to the optimization of Ag-pSi SERS substrates in the recent years. Starting from boron doped mesoporous silicon they studied the influence of silver NPs synthesis parameters, such as silver nitrate concentration, temperature, dipping time and the addition of capping agents.

Figure 2.8 (a) shows the effect of the variation of silver nitrate concentration and of reaction time on the morphology of the obtained nanostructures.[47] If the $AgNO_3$ concentration is fixed, a longer dipping time results in a size increase of the synthesized particles. Indeed, a different growth mechanism is observed in high and low concentration regimes: for longer reaction time, a higher polydispersion is found at high concentration, due to the nucleation of new NPs families. In contrast, particle growth by coalescence is favoured at low $AgNO_3$ concentration. As expected, concentration and temperature (not shown) influence the reaction kinetics, as it is evinced by the quite longer dipping time required to get particles with comparable diameter at low and high concentrations. Such morphological changes affect the palsmonic properties of the Ag plated material. In this way, the optical response of Ag-pSi can be easily tuned from the UV to the NIR range in order to match the laser excitation wavelength, as highlighted by the UV-Visible reflectance spectra, shown in Figure 2.8(b) for several synthesis conditions (note that the observed signal modulation by narrow fringes is a consequence of the Fabry-Perot interference in pSi thin films). Concerning the SERS efficiency of the Ag-pSi nanostructures, ultra-low detection limits were reported in the last years for dyes under electronic resonance conditions. Rhodamine 6G and Cyanine 3 spectra were observed in single molecule regime, at concentrations ranging from 10^{-12} M to 10^{-15} M.[43,106] SERS spectra of crystal violet were also detected with an off-resonant excitation at 785 nm at concentrations as low as 10^{-10} M.[107] Although the substrates show a very high SERS efficiency, the analysis of Raman signal uniformity on silvered porous silicon has received less attention. Bandaranka et al. addressed this issue in a recent paper.[108] They measured an intra-substrate relative standard deviation of 20% on their Ag-pSi samples, suggesting that the homogeneity of the SERS enhancement could be improved by a more uniform distribution of the dopant in the starting silicon wafer. Indeed, they found out that in Sb-doped silicon a swirl-like

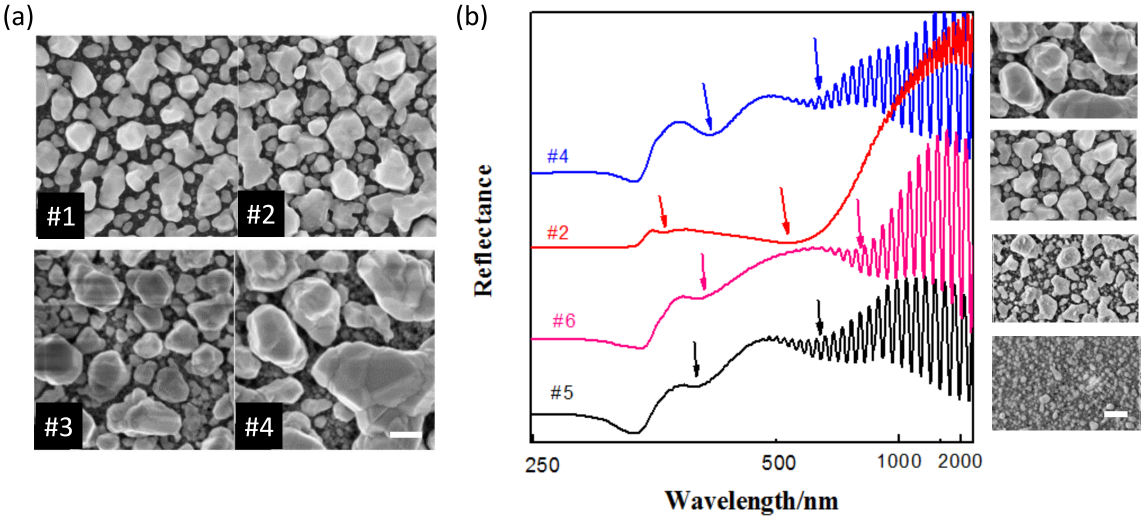

Figure 2.8 (a) FESEM images of Ag NPs on pSi obtained under different synthesis conditions (dipping time and $AgNO_3$ concentration). #1: 30s / 10^{-2} M; #2 60s / 10^{-2} M; #3: 300s / 10^{-3} M; #4: 600s / 10^{-3} M. (b) UV-Vis-NIR specular reflectance of Ag-pSi samples characterized by various morphologies shown on the right of the plot. Dips ascribed to LSPRs are marked with arrows.

resistivity profile influenced the porosification and the subsequent metal plating in a negative way.[108] After Sb ion implantation the RSD was reduced to 7%.

2.3 SERS substrates for biosensing applications

The potential of SERS spectroscopy in the biological framework was immediately recognized after its discovery.[109] The trace sensitivity combined to the selective structural and compositional information, the ability to quench the typical fluorescence of biological samples and the possibility of analysis in water based environments were important factors which led to a strong development of this field.[17] Furthermore, in recent years the advantageous combination of SERS substrates with microfluidic or arrayed platforms promises the evolution of fully portable, low cost and more efficient bioassays, in addition to high throughput parallel analysis of many interesting species. An introduction to SERS biosensing and to the miniaturization of the SERS platforms is provided in the following sections.

2.3.1 SERS bioassays and biosensors

SERS bioresearch has focused both on fundamental aspects, such as the study of biomolecules structures, conformational changes or function, and on applied biomedicine, namely for diagnostics and therapy monitoring.[49] Bioanalytical applications and biosensing actually belong to this second stream and concerns with the detection of molecules relevant for biological processes and/or biomarkers. The bioanalyte can be either revealed on the bare SERS substrate or on specifically functionalized surfaces. The first approach benefits of the intrinsic specificity of SERS spectroscopy which provides the vibrational fingerprint of the analysed molecule. However, due to the complexity of the involved molecules, that can be even polymeric, and of the biological matrixes, a probe, which specifically captures the target molecule, is often required. Different classes of analytes have been detected by SERS spectroscopy, including small molecules, such as metabolites, nucleic acids, proteins and peptides. Next sections will introduce the main strategies and SERS substrates employed, with a special focus on DNA and RNA biosensing.

2.3.1.1 Small metabolites detection

Metabolites are products or intermediates of the metabolic cycles in the organisms. They are therefore small molecules of fundamental importance, whose detection can reveal details about normal biological processes or pathological states.[110] Glucose sensing is for example essential for diabetes-patients, while neurotransmitters detection is of interest in the framework of brain functions and injuries.[7] Due to the relatively small and simple structure of these metabolites their analysis by SERS has been performed without the functionalization with specific probes. Dopamine and norepinephrine mixtures were adsorbed on silver colloids and their signals could be distinguished, although their structure differs only in a hydroxyl group, thanks to the enhanced specificity of SERS spectra.[111] An optical sensor for glucose was also suggested as an alternative to the traditional electrochemical method. An Ag-FON (Film Over Nanospheres) substrate was modified with alkanethiols chains to favour the adsorption of the sugar onto the surface. A calibration curve was built by means of the partial least squares (PLS) chemometric method and quantitative measurements were possible in the clinically relevant range of concentraitons.[112] Recently, SERS spectra of complex biofluids, such as serum or whole blood plasma were acquired. Measurements performed under 785 nm excitation provide signals that are dominated by metabolites peaks. Typical features of hypoxantine and uric acid were identified.

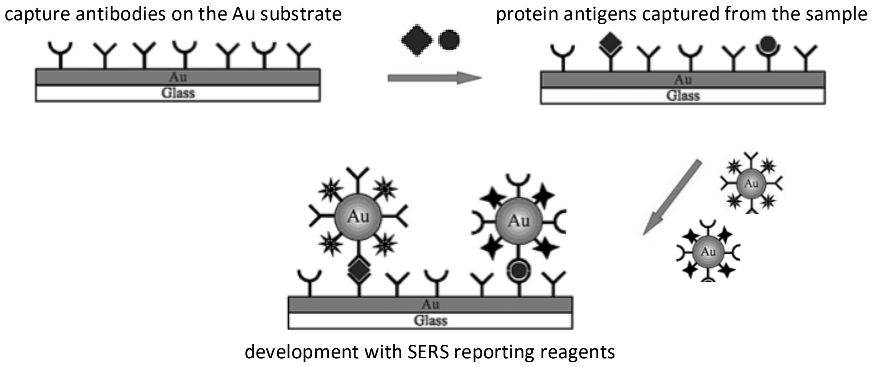

Figure 2.9 Scheme of a sandwich immunoassay for protein detection by means of SERS analysis[1]

Different Au and Ag colloids[110] or Au NPs grown on a silica substrate were employed.[113] The alteration of the metabolic profile of serum or blood/plasma can be related to several pathological conditions and its SERS analysis is hence considered promising for diagnostic purposes.

2.3.1.2 Proteins detection

Proteins are complex biopolymers of aminoacids that fold into a precise 3D structure. These biomolecules play important functional and structural roles in every organism. Moreover, specific proteins or peptides are involved in cancer and neurodegenerative diseases Although spectra of proteins adsorbed on metal nanostructures have been presented[114,115], their SERS identification and quantitation is usually performed exploiting a functionalized sample. Indeed, proteins can undergo denaturation (loss of the 3D folded structure) upon direct interaction with the nanoparticles, complicating their detection. For instance, this makes very hard to distinguish different protein isoforms. Most of the assays are, then, based on a specific interaction between the protein and its ligand. Commonly, an antibody, a receptor, or even a small molecule (e.g. biotin or an oligonucleotide), which are able to bind a specific protein domain, are chemically linked to nanoparticles modified with a SERS label.[1] Different detection schemes are then possible. Proteins immobilized on a substrate can be incubated in the probe NPs solution, or sandwich immunoassays can be performed. The latter involve the covalent immobilization of the antibodies onto a surface, the recognition of the analyte (the protein of interest) and finally the incubation with the probe nanoparticles (Figure 2.9). After washings, a step of silver staining may be necessary to observe a SERS signal if the arrangement of the nanoparticles is not dense enough to provide the desired SERS enhancement. These methods offer however the advantage of the easy development of multiplexing platforms, where each protein is recognized by a particle functionalized with a different Raman label.[116]

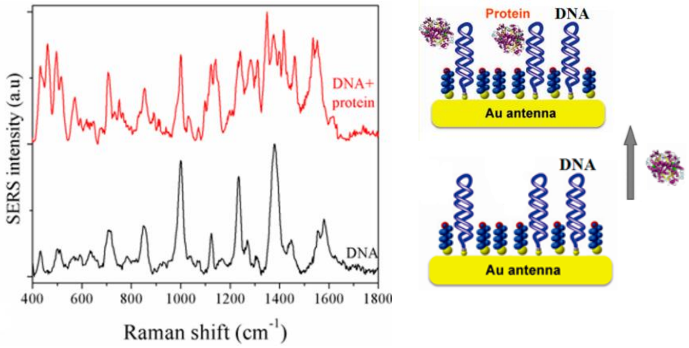

Figure 2.10. Label free detection of MnSOD on aptamer-functionalized Au nanoantennas[117]

An alternative approach, based on aptamer (DNA sequences showing high and specific affinity to a certain protein) functionalized SERS substrates has been recently reported. A protein cancer biomarker, the MnSOD (Manganese SuperOxide Dismutase), was detected without the need of SERS reporters down to the nanomolar concentration range.[117] The vibrational signature of the protein can be distinguished in the spectrum of the protein-bound aptamer (Figure 2.10). In contrast to the traditional SERS label based assays, this method is not influenced by nonspecific signal, which gives rise to a higher noise level and consequently rises the limit of detection.[117]

2.3.1.3 DNA and oligonulceotides detection

The detection of nucleic acids by SERS is very promising and has attracted a huge attention in the last years. Due to the combination of the quite high Raman cross sections of the nucleobases, combined with the enhanced sensitivity provided by the SERS substrate, low limits of detection can be reached. Therefore, nucleic acids have been analysed starting from their smallest components, the nitrogenous bases, adenine (A), guanine (G), cytosine (C) and thymine (T) (replaced by uracil (U) in RNA)[118,119], their monomers, the nucleotides[120] (nts), and oligomers[121–123], up to DNA and RNA strands both by SERS and TERS[124,125] (Tip-Enhanced Raman Spectroscopy). Figure 2.11 (a) shows the structure of the adenosine monophosphate, one of the four nucleotides of DNA. Each nucleotide is composed by a 3'-phosphorylated deoxyribose ring, that binds a nitrogen of the nucleobase with its carbon in position 1'. The linkage between monomers occurs through the C5' of the sugar of one nucleotide and the phosphate group of the following one. The DNA polymer has therefore a specific direction and is characterized by a negatively charged backbone in physiological conditions, which determines the electrostatic interactions of the molecule. Nucleobases bear instead the hydrogen bonding ability of DNA, thanks to the nitrogen and oxygen atoms of the heterocycle. These are responsible for the assembly of double stranded DNA, where specific base pairs (A-T, C-G) keep the structure together through this kind of interactions (Figure 2.11 (b) and (c)).[126] In analogy to DNA, base pairing of complementary sequences takes place for oligonucleotides, both for DNA-DNA and DNA-RNA complexes. Such interaction is called hybridization. Stacking between the aromatic rings has also been demonstrated to be an important stabilizing factor for the hybridized structures, in particular in solution and in presence of salts.[127] Hybridization is a highly specific biorecognition event and is for this reason widely exploited in biosensing of oligonucleotides. Depending on the base pairs and on the length of the oligo sequence different binding energies are foreseen and the

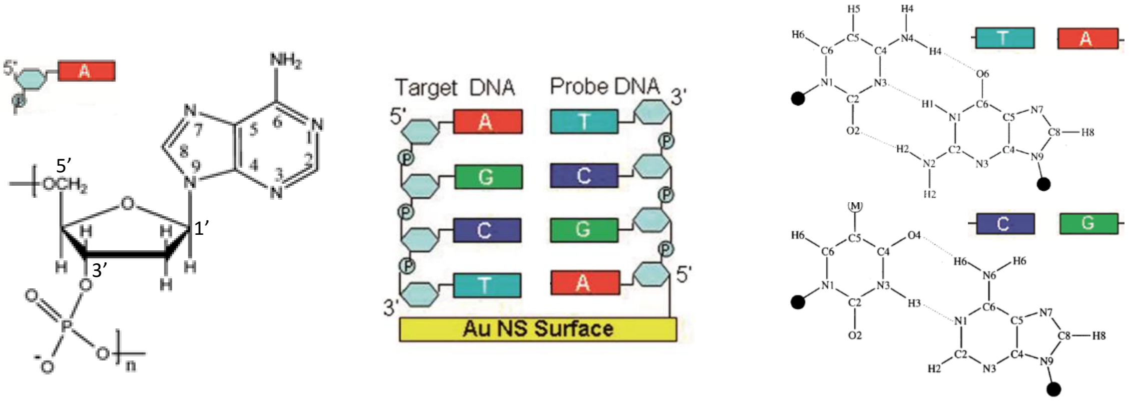

(a) (b) (c)

Figure 2.11 (a) Adenosine monophosphate nucleotide, one of the four DNA building blocks; (b) hybridization between an immobilized probe and a free target oligonucleotide. (c) Hydrogen bonding between thymine and adenine (top) and cytosine and guanine (bottom).

so-called melting temperature of the hybridized complex can be defined. Due to the discussed dependence on solvent, ionic strength and temperature of the energies involved in the double strand formation, these factors have to be carefully considered when developing a hybridization based bioassay.[128] Indeed, customized sequences, which are complementary to the interesting one, can be synthesized to capture it specifically. The detection can take place with different schemes, including tests with labelled targets[129,130], labelled probes, but label free targets[131,132] and completely label free assays.[133–135]

In the first SERS bioassays for oligos, presented by Vo-Dinh et al., the target sequences were immobilized on a nitrocellulose filter and exposed to a solution of complementary dye-labelled oligo probes. After washings to remove the non-specifically bound probes, the hybridized complexes were recovered from the filters and transferred to a silver-coated alumina substrate for the SERS detection.[132] A three component sandwich assay was, then, implemented by Cao et al.[131] In this assay, whose scheme is shown in Figure 2.12, Au nanoparticles are functionalized with a thiolated and dye-labelled 15-nts oligo, complementary to the first half of the 30-nts target DNA. A second oligo probe, which matches the second half of the target was immobilized onto a surface and then incubated with the target and the nanoparticles. SERS activity is then conferred by silver staining, providing limit of detection as lows as 20 fM. Although this is the best sensitivity reported so far, the development of the assay directly on the SERS substrate surface would be advantageous and reduce the number of steps, thus leading to shorter sensing times. To this end, the detection of the decrease in intensity of the SERS label spectrum upon hybridization of molecular sentinel structure was suggested. In such an assay a hairpin shaped oligo probe is modified with a SERS dye at one end and attached to an Au MFON substrate at the other end. After binding the complementary target sequence, the dye is far from the enhancing surface, causing a reduced SERS intensity. Such platform is suited for quantitative measurements.[136]

Despite the complexity of DNA analysis, due to the fact that probe and target are made by the same type of nucleotides, some examples of completely label free detection have appeared. Among the approaches that involve probe immobilization through a thiol end, the hybridization has been assessed either by the comparison of the peak intensity ratios before and after the recognition of the target[134] (Figure 2.12 (b)) or through the replacement of the naturally occurring adenine nucleobase with a 2-aminopurine in the probe sequence. In the latter case, intense adenine bands were observed upon hybridization.[133] Finally, some groups have demonstrated that

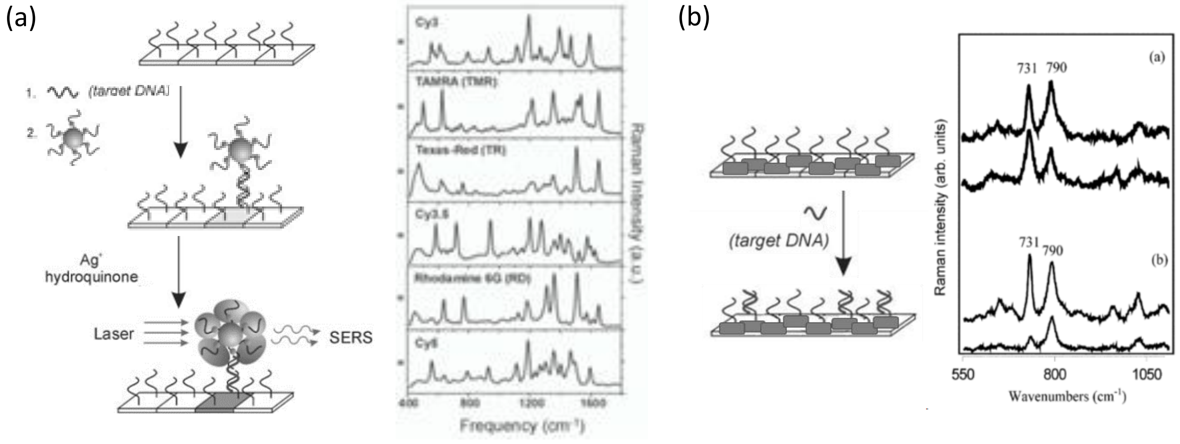

Figure 2.12 (a) Scheme of a sandwich assay for SERS detection of DNA with labelled probes. The recognition event is reported by the detection of the dye spectrum.[131] (B) Label-free detection of target DNA binding to the oligo probe immobilized on SERS active silver nanotori. Hybridization is assessed through the changes in the spectrum due to the vibrational fingerprint of the target.[134]

oligonucleotides can be distinguished by their vibrational fingerprint applying an appropriate elaboration of the spectra. SERS of different sequences were systematically acquired on silver colloids by Papadopoulou et al., which reported the possibility to differentiate the sequences at the single base mutation level.[137] Prado et al. showed that several RNAs mixtures can be analysed quantitatively by a method based on the deconvolution of the spectra in the ones of pure homosequences.[122]

The great interest devoted to nucleic acid detection is explained by the numerous applications related to this aim. Few examples are the genomic sequencing by hybridization of known complementary oligonucleotides, the detection of DNA mutations, the identification of viruses and pathogens by their genome or the quantification of disease biomarkers. MicroRNAs, short ribonucleic acid sequences with regulatory functions, belong to this last class. Next section will introduce the main roles of these oligonucleotide explaining the importance of their detection.

2.3.1.3.1 Micro-RNAs

MicroRNAs are single stranded RNAs composed by 17-23 nucleotides, that are endogenously expressed in several plants, animals and viruses.[138] A large variety of miRNAs have been so far identified, being more than 1000 in humans[139], even if the number of miRNAs is typically estimated as ~30 000.[140] In their mature form, which is achieved after several cleavages of the primary miRNA (pri-miRNA, a 1000 to 3000 nts sequence) inside and outside the nucleus, they carry out a post-transcriptional regulation function on gene expression.[140] In detail, miRNA act on the protein synthetic pathway through their interaction with messenger RNAs (mRNA), transcripts of encoding genes, containing in their nucleotodic sequence the information about the aminoacidic sequence to be assembled in the ribosome. This interaction, occurring in the cell cytoplasm, is mediated by the RNA Silencing Complex (RSIC)[141], which binds the mature miRNA and drives its perfect or imperfect hybridization to the target mRNA[142]. As a consequence, mRNA degradation, translational inhibition or sequestration occurs, determining a lowering of protein expression levels. The system involved is intricate: genes can be regulated by multiple miRNAs and each miRNA is able to target hundreds of transcripts either directly or indirectly. As expected due to this powerful influence on the translational stage, several experiments have demonstrated the involvement of miRNAs in almost all biological processes, including early development, cellular differentiation, proliferation, apoptosis and haematopoiesis, as well as initiation of diseases and alteration of immune system functions.[140] Furthermore, the inability to produce mature miRNA results in the death or infertility in some animal species.[143] The known miRNA redundancy (more than one sequence is able to perform the same role, due to the imperfect matching with the target) has therefore been understood as a defence mechanism, which allows the correct regulation even if one miRNA is not

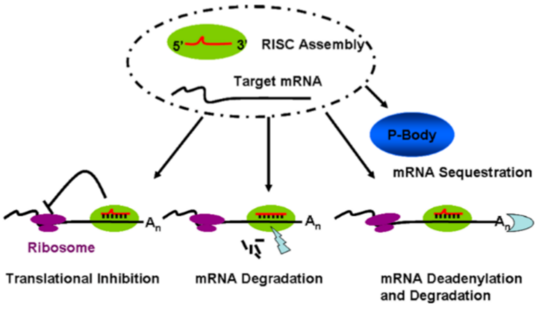

Figure 2.13 Binding of the miRNA-RISC assembly to the 3' untranslated region of a target mRNA already associated to the ribosome and possible mechanism of protein translation blocking.[140]

expressed.[144]

In the organism, miRNAs are found both as intracellular and extracellular species. From few copies to 50000 miRNAs can be present in a cell, constituting however less than the 0.01% of the total RNA cellular content.[140] In the extracellular environment, they are probably protected from endogenous RNAase degradation thanks to the inclusion in vesicles, such as exosomes (microparticles produced by exocytosis and apoptotic bodies) or by the association to RNA binding proteins.[145] Their release in plasma concerns with specific miRNA patterns, whose alteration has been correlated to many diseases and cancer types.[140] For this reason, and due to their central role in cancer initiation, development, maintenance, and proliferation, the use of circulating miRNAs as biomarkers of the pathological state or for therapeutic purposes has been suggested.[146] Moreover, circulating miRNA could improve on current strategies for cancer detection towards a noninvasive early diagnosis of various cancers. To this end, a monitoring platform is strongly needed. The development of biosensors for miRNAs has however to face many challenges. In particular, their low abundancy, the co-presence of mature and immature sequences, the huge variation in concentration between miRNAs and the slight difference in sequences highlight the requirement for a sensitive, highly specific and wide dynamic range technique. Multiplexing is also fundamental as the entire miRNA expression profile related to a specific pathology or biological process has to be screened. Although some well-established technologies exist, mainly based on electrophoretic separation (Northern blotting), microarrays (fluorescent or isotope labelled probes are used) and qRT-PCR (Quantitative Real-Time Polymerase Chain Reaction) [147], SERS technique is very promising to address this issue. Driskell's group first presented a methodology to discriminate between miRNAs adsorbed on Oblique Angle Deposited nanorod arrays by the treatment of SERS spectra with a multivariate PLS-DA (Partial Least Squares-Discriminant Analysis).[148] Sandwich and direct bioassays based on labelled probe nanorods[149] were also suggested for miRNA 21, but showed a quite high limit of detection (0.36 nM) in comparison to the typical sensitivities in the presence of SERS reporters. Recently, the label free detection of miRNA hybridization in a rationally designed bioassay was reported again by Driskell's group, which exploited a Least Squares analysis to get semi-quantitative results.[135] However, the development of new cheaper SERS substrate, a careful optimization of the assay conditions, and the integration of multiplexing platforms in microfluidic chips are expected to improve both the specificity and the limit of detection of the bioassay. Last section of this chapter will discuss the development of multianalyte platforms both integrated or not in a microfluidic system and their advantages.

2.3.2 Lab-on-chip SERS platforms

The case of miRNAs clearly demonstrates how a reliable multiplexing platform for SERS detection is of broad interest. However, many other analytes could benefit from such an approach. Fully portable, low cost chips, allowing rapid measurements, are required for on-site monitoring and point-of-care applications. Indeed, SERS substrates prepared as arrayed spots or integrated in microfluidic circuitries have been fabricated to respond to this need. Open or closed platforms can be chosen, each characterized by its own advantages and drawbacks. SERS arrays can be obtained by pre-patterning (either chemically or physically) of the support surface, followed by selective metal deposition [86], by masking[150] or by additive techniques.[151,152] The latter approach groups the emerging printing technologies, such as screen and ink-jet printing. The second one has attracted great interest for its mold-free nature and low cost, where the pattern can be easily defined by direct writing with a printhead. The main features of ink-jet technology and its first applications concerning with SERS arrays are described in the followings.

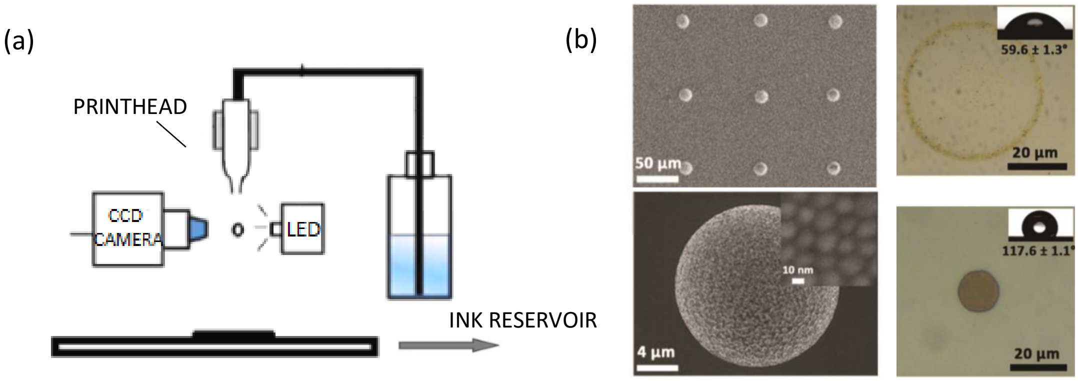

Figure 2.14 (a) Schematic representation of the fundamental components of an inkjet printer.[153] (b) SEM images of an ink-jet printed SERS array and magnification of a single spot made by close packed gold NPs. Optical micrographs on the right show the effect of the ink contact angle on the final NPs arrangement after drop drying.[154]

2.3.2.1 Ink-jet printed SERS substrates

The principle underlying inkjet technology is quite simple. In the most common set-up a piezoelectric responsive print-head, fed by an ink reservoir, is actuated by a software-driven electrical waveform. The compression of the liquid in the printhead initiates the propagation of a pressure wave, which, after reflections at the nozzle ends, finally causes liquid ejection if the fluid kinetic energy is higher than the surface energy required by droplet formation.[155] In this way, droplets can be printed on demand, on the desired point, with a good control over drop volume and velocity, by simply shifting the substrate under the printhead with sub-micrometric accuracy (see Figure 2.14 (a)). Droplet ejection can be monitored by a CCD camera. Indeed, the DOD (Drop On Demand) technology and the reproducibility of drop dispensing are two of the most attractive features of inkjet printing. However, the printability of the ink and the substrate-drop interaction are key aspects that have to be taken into account. As the ink properties affect the propagation of the pressure wave, different liquids can be printed more or less easily. According to Fromm's and Derby's work[156], the printing behaviour of inks can be classified by the calculation of the Z number, a value that depends on the liquid density, surface tension and viscosity, as well as on the diameter of the nozzle orifice. Inks with $1< Z < 10$ show a good printability. Below 1, the viscosity is too high and the pressure wave is dissipated, while for $Z>10$, satellite droplets are ejected with the main drop. Pure water is for example hardly printable, hence it is often used in mixtures with lower surface tension, higher viscosity solvents or with surfactants. Regarding the interaction of the drop with the surface, the wettability of to the printed substrate towards the ink has to be considered. The static and dynamic contact angles of the ink determine the resolution of the pattern or the possibility to write continuous stripes.[154] For particular interfaces and printing parameters (especially printhead pass rate and drop-to-drop step size) these lines are in fact unstable leading to profiles affected by the presence of bulges or to the collapse in separated and bigger drops.

Patterning of SERS substrates by inkjet technology follows two different strategies.[157] The ink can either contain plasmonic nanoparticles or some precursors. Both approaches are quite common in the inkjet printing of conductive tracks. As for SERS applications, in the first case, the quality of the starting colloid and the ability to drive solvent evaporation towards the assembly of uniform and reproducible aggregates are fundamental. This can be achieved by printing on substrates modified by a hydrophobic coating, as demonstrated by Yang et al.[154] They employed inkjet technique to print a gold NPs based ink, producing the array of SERS active spots displayed in Figure 2.14 (b), with an outstanding uniformity (RSD of Rhodamine 6G signal <3%) and a very good Raman

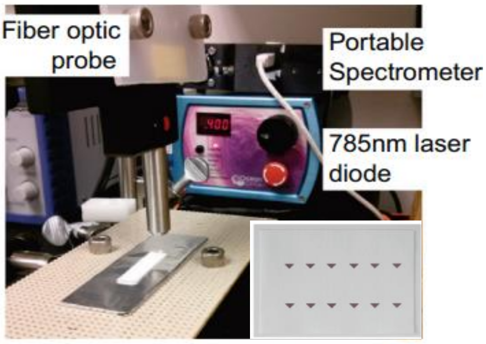

Figure 2.15 Set-up for the detection on a SERS active paper strip with a portable Raman spectrometer. The inset shows an array of printed SERS substrates, which can be cut with the desired shape.[153]

enhancement. The right side of the figure shows how they were able to avoid the coffee-ring effect (concentration of the particles at the borders of the drop) observed for drying of low contact angle drops, obtaining a closely packed arrangement of the NPs. This was achieved by tuning the surface properties of the substrate. Inkjet printing was also exploited for the production of Ag or Au NPs patterned paper-based dipsticks and swabs for on-site sampling and measurement.[158] The capillarity due to cellulose porosity was exploited to pre-concentrate the analyte by the lateral flow technique, whereas the set-up displayed in Figure 2.15, equipped with a fiber optic coupled portable Raman spectrometer, was used for the detection. In situ synthesis of nanoparticle was instead demonstrated by a single proof of concept experiment by Chiolerio et al. by printing silver nitrate based inks on porous silicon.[159] Although silver nanostructures could be synthesized in situ, their morphology didn’t allow sensitive SERS detection.

2.3.2.2 Microfluidic integration

The fabrication of multiplexing SERS microfluidic devices is another convenient solution for multianalyte detection. It is worth to underline that SERS analysis in microfluidic channels or chambers is characterized by some advantageous features in comparison to normal SERS. First of all, the distribution of the analyte on the SERS substrate surface, which is usually non-uniform due to the drying process, can be quite homogenous in fluidic systems. Minimization of the sample volume required for the measurements and the reduced risk of contaminations due to the isolated environment are also convenient aspects, especially in case of on-field analysis.[81] Furthermore, in dynamic conditions, the continuous flow lowers the localized heating of the measured area, leading to more reproducible spectra, not affected by the thermal- or photodegradation of the analytes.[5] More general advantages deal with the enhanced kinetics in dynamic conditions and the low cost of miniaturized devices.[160]

Microfluidic chips for SERS analysis can either be based on the injection of a plasmonic colloid in the channel, under controlled mixing between the analyte and the nanoparticles, or exploit nanostructures immobilized on a substrate. In both situations the synthesis/fabrication may be performed in situ. While the first method seems to provide better mixing conditions, which are achieved by the design of micromixers, problems related to the stability and cleanliness of the colloidal suspensions exist.[161] An example of a basic set-up is shown in Figure 2.16 (a). The two inlets allow the separate the injection of the molecule and of the nanoparticles, while the signal is sampled in the regions characterized by the presence of pillar arrays which promote the mixing by chaotic advection.[162] More complex chips have also been prepared. Choi et al. reported on the SERS detection of bicomponent dye-labelled oligonucleotide mixtures in a chip presenting a complex micro-network, from which concentration gradients arise.[163] Prado et al. compared laminar streams

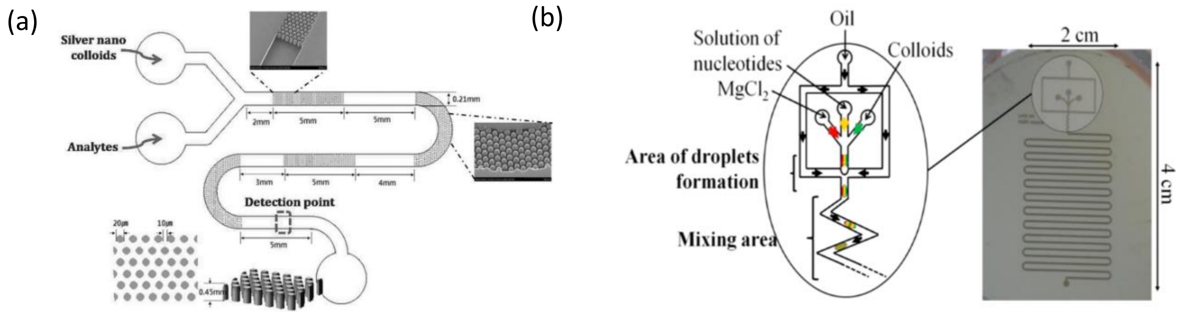

Figure 2.16 (a) Scheme of a PDMS microfluidic chip for SERS detection on flowing silver nanoparticles. Homogeneous mixing is provided by the pillar arrays shown in the SEM micrographs.[162] (b) Scheme and photograph of a microfluidic circuitry for flowing microdroplets mixing.[164]

to flowing microdroplets based chips for the label free analysis of short RNA sequences. The scheme of the latter system is depicted in Figure 2.16 (b) and makes use of an oil as carrying agent in which hydrophilic vesicles behave like microreactors in which the SERS detection takes place.[164] Popp's group focused instead its attention on the exploitation of a microfluidic circuitry for the development of reliable quantitative analysis methods.[165,166] In contrast to the discussed platforms, highly stable anchored nanostructures are sometimes affected by analyte diffusion issues, which reduce their sensitivity, and may require higher cost technologies.[5] However, in situ-synthesis and the increase of the SERS active volume can overcome these drawbacks of solid substrates. Indeed, nanostructures prepared by lithography[167,168] (Figure 2.17 (a)) or metal deposition methods[81,169] (Figure 2.17 (b)) need to be first fabricated and then aligned and bonded to the microfluidic circuitry. On the contrary, easily prepared SERS active nanostructures were directly synthesized in microchannels through galvanic replacement[170,171](Figure 2.17 (c)) or by photoreduction of an

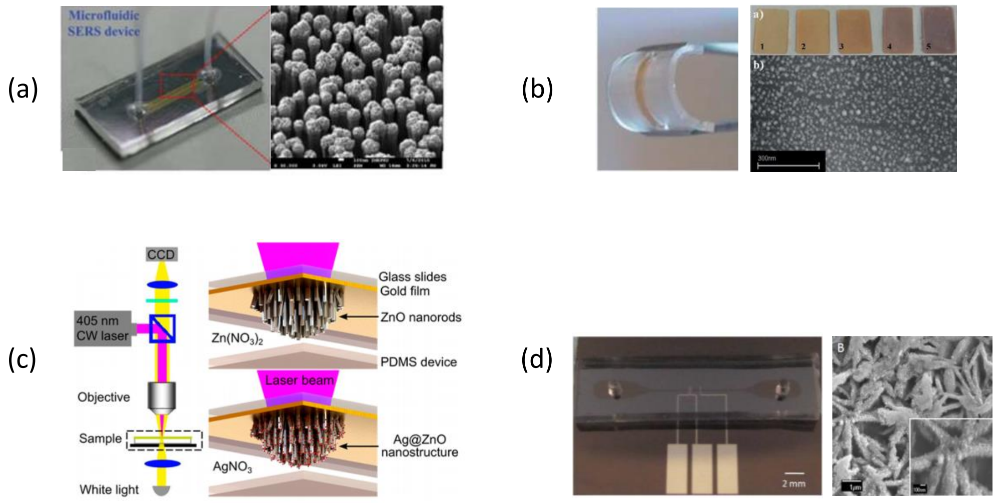

Figure 2.17 Top: Microfluidic devices fabricated by bonding of a cover on (a) Ag-coated Si nanopillars obtained by oxygen-plasma stripping of photoresist and RIE;[167] (b) DC sputtered AgNPs nanoparticles on flexible PDMS slices.[81] Bottom: In situ synthesis in microfluidic channels. (c) optothermal growth of Ag-coated ZnO nanowires obtained by heating of a gold substrate thanks to laser irradiation in presence of ZnO and Ag precursors;[172] (d) Ag decorated Cu nanowalls synthesized by in channel Cu electrodeposition and subsequent Ag galvanic replacement.[171]

adsorbed silver precursor on titania nanotube arrays.[173] These tubular structures, similarly to the Ag-coated ZnO nanowires obtained by laser optothermal activation in specific sites of the channel[172](Figure 2.17 (d)), can also take advantage of their 3D dimensionality to increase the sampling volume. Concerning the SERS efficiency of the microfluidic devices, enhancements of 6-7 orders of magnitude are observed for most of the systems.[170,172,174,175] The use of such platforms for environmentally relevant threats has been reported, concerning with the detection of pesticides[170,176], pollutants[177] or pathogens. An assay for the detection of oligonucleotides via the so called molecular-sentinel probes was also demonstrated in a PDMS chip equipped with gold nanoporous disks.[178] Finally, microfluidic devices can implement additional functions, such as sample preparation or pre-concentration, which can further improve the SERS substrate performances.[161]

Chapter 3

Characterization techniques

3.1 Introduction

When a new SERS substrate is developed, several characterization techniques can help to get an insight into its properties. First of all, a morphological characterization should be provided. Scanning Electron Microscopy is the technique of choice for solid SERS substrates (while Transmission Electron Microscopy is typically used in case of colloids). An overview on the optical far-field response can be inferred by UV-Visible-NIR spectroscopy. Raman characterization is the core, providing the information about the SERS performances of the substrate. In some cases, contact angle measurements can be useful to study the surface chemistry of the support, both to better understand its behaviour along the synthetic process or to monitor substrate wettability changes upon nanoparticles formation and functionalization. This last chapter aims to a brief introduction to the theoretical basis of the characterization techniques of SERS substrates, limited to those employed in the thesis work.

3.2 Field Emission Scanning Electron Microscopy

Field Emission Scanning Electron Microscopy (FESEM) is a Scanning Electron Microscopy (SEM) technique suitable for very high resolution morphological characterizations. The basic set-up comprises a microscope, equipped with an electron gun for the electron beam generation, a number of magnetic lenses and electromagnetic coils for beam size, focusing, shape and trajectory adjustment and the detectors, interfaced to a control console. Regardless of the used electron source, the construction of a morphological image is obtained by the interaction of the electron beam probe with the sample. When the beam impinges onto its surface two different phenomena are observed: elastic scattering of the incident electrons and inelastic scattering, combined to the emission of outer electrons from the atoms of the studied material as well as X-rays and Auger electrons generation. In the first case, electrons are scattered multiple times in the sample until their random trajectory leads them to emerge from its surface as Back-Scattered Electrons (BSE). Low energy (< 50 eV) electrons produced by inelastic scattering are instead called Secondary Electrons (SE). Because of the different energies involved in the processes, each signal is able to provide information about different properties of the analysed material. SE, coming from a limited sample thickness, are for example more sensitive to the topological features and allow the best resolution, while BSE are able to provide a good Z (atomic number) contrast, as the elastic scattering cross section depends on Z^2.[179] Both BSE and SE can be employed to build a morphological image of the sample, by rastering the electron beam on its surface and collecting the signal with the specific detector. The image appears on the computer screen with a point-by-point correspondence. The resolutions for a SEM system is around 10 nm, while it is around 2-1 nm for commercial FESEM instruments. This improvement is due to the replacement of classical SEM thermionic electron sources, where heat is the driving force for electron ejection from a tungsten hairpin, with a field emission cathode. In FESEM systems a negative potential of several thousand of volts is applied at the very sharp tip of a thin tungsten needle.[180] The concentration of a huge electric field at the tip apex causes electron tunnelling out of the cathode over values of 10 V/nm.

Very high currents (10^9 A/cm^2) and monochromatic beams can be supplied by this “cold” electron source, which works under high vacuum conditions (10^{-10} Torr) and can be also partially heated to desorb impurities from the wire.[181]

Due to the use of electrons as a probe, the studied material should be at least partially conductive. If not, metallization with thin conductor films can be performed for those samples, whose features are not altered by the nanoroughness of the film. Otherwise some tricks to supply a discharging pathway have to be implemented. A Zeiss SUPRA-40 FESEM (Zeiss SMT, Oberkochen, Germany) was employed in this work. The instrument provides an accelerating voltage between 0.1 and 30 kV, magnification from 12 to 900000 X and a nominal resolution of 1.5 nm at 10 kV and at a working distance of 2 mm.

3.3 UV-Vis-NIR spectrophotometry

UV-Vis-NIR spectrophotometry can be employed to monitor a number of processes, ranging from electronic (HOMO-LUMO, charge transfer, d-d) transitions in molecules and solids, band transitions in semiconducting and insulator materials and reflection in photonic nanostructures. Plasmonic absorption and scattering also occur in this range for Ag and Au. In a typical experiment, a monochromatic radiation, obtained by passing the light from a continuous source in a monochromator, is focused on the sample and the reflected or transmitted radiation is sent to the detector. The CARY5000 UV-Vis-NIR spectrophotometer (Agilent Technologies, Santa Clara, CA, USA) used in this thesis (Figure 3.1) works with liquid and solid samples (both powders and films), thanks to the different sample-holders. This instrument is also equipped with a diffuse reflectance integration sphere and a specular reflectance unit with an incidence angle of 12.5°. The wide accessible wavelength range (175-3300 nm) is achieved by the combination of a deuterium (UV) and a halogen (visible) source with a R928 photomultiplier tube UV-Vis detector and lead sulphide photocell NIR detector. Wavelength dispersion is performed using dual double-sided gratings in a Littrow monochromator.

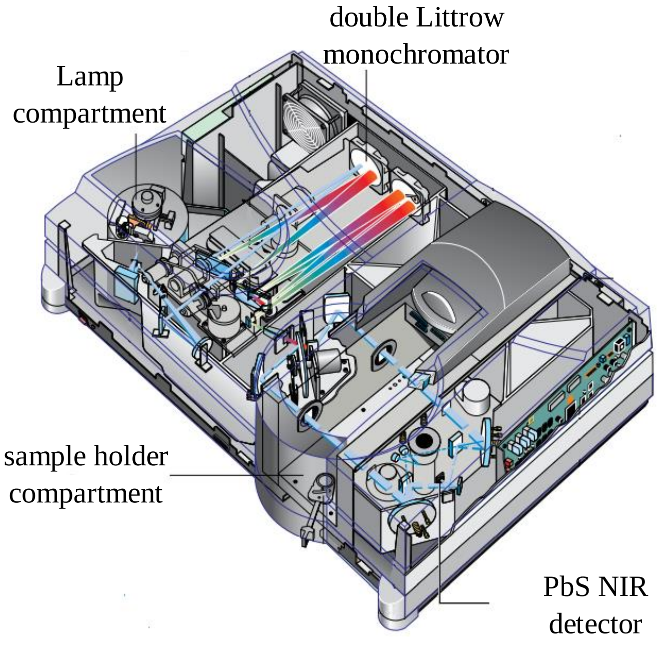

Figure 3.1 Schematic view of the UV-Vis-NIR CARY5000 spectrophotometer

3.4 Raman spectroscopy

Raman spectrophotometers or Raman microscopes are commonly employed for laboratory Raman measurements. The working principle is similar: they are both based on a laser source producing a monochromatic collimated laser beam, which is sent to the sample through the reflection by a series of mirrors. After collection of the light scattered by the analysed material, a very narrow band pass filter is needed to remove the intense Rayleigh component, which is spectrally close to the Raman scattered ones. Notch or edge filters usually carry out this function. Subsequently, the isolated Raman scattered radiation is sent to a dispersive element, usually a grating, which is able to separate it in its spectral components. Finally, a mirror deviates light towards the detector, typically a CCD array. The Raman microscope differs from a normal spectrophotometer in that the excitation and collection of the radiation is performed through the objective of an optical microscope. In this way, light can be focused on the sample, reaching very high intensities, small sampling volume and very good resolutions, which allows high resolution Raman mapping. A scheme of a micro-Raman spectrophotometer is shown in Figure 3.2. This set-up exploits a backscattering configuration, in which the incoming and collected radiations are separated by 180°. Special optics, that can operate both as a Rayleigh filter during collection and as a laser mirror in the excitation, are required at the interface between the Raman spectrometer and the microscope. Holographic notch or edge filters and special dielectric mirrors are often employed, since they minimize laser intensity and Raman scattering losses.

A Renishaw inVia Reflex Raman Microscope was used in this thesis. The set-up is characterized by the following features:

- wavelengths range 400−1000 nm;
- -70 °C Peltier cooled CCD detector;
- spatial resolution 1 µm (objective 50x);
- available excitation laser lines (diode lasers): 457.9 nm (25 mW), 514.5 nm (100 mW) and 785 nm (500 mW).

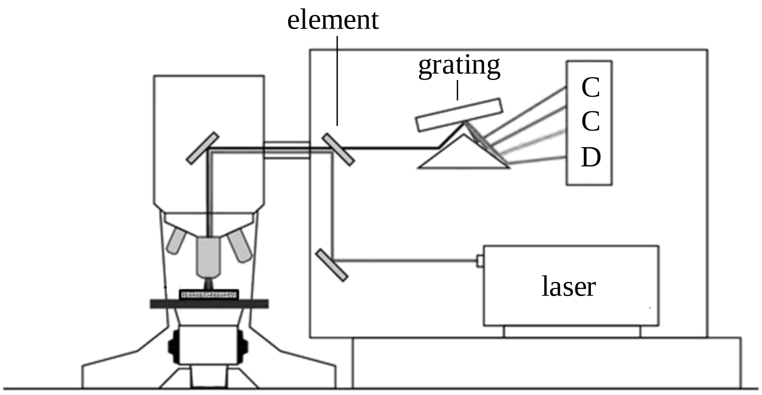

Figure 3.2 Scheme of a Raman microscope

3.5 Optical Contact Angle

Optical Contact Angle measurements are widely applied to the study of surface properties and functionalization by means of well characterized standard liquids. Moreover, the contact angle (CA) between specific surfaces and liquids can be monitored, if their wettability is of interest for some particular applications.

The interpretation of contact angle data for a drop lying on an ideal surface is based on the Young's equation:[182]

$$\gamma_{lv} \cos\vartheta_Y = \gamma_{sv} - \gamma_{sl} \qquad 3.1$$

Young's equation explains the observed contact angle, ϑ_Y, as the result of the mechanical equilibrium of the drop under the action of the three interfacial forces: γ_{lv}, the surface tension of the liquid-vapour interface, γ_{sv}, the surface energy, namely the solid-vapour interfacial tension, and γ_{sl}, the interfacial solid-liquid tension. For smooth and homogenous surfaces, it is possible to derive the surface energy if the surface tension is known. The development of a model for the unknown γ_{sl} is however required and it is usually based on the assumption that the interfacial solid-liquids tension is a function of γ_{lv} and γ_{sv}, although many variations exist.[183]

Although Young's equation defines a single equilibrium CA, many metastable angles can be observed in sessile drop measurements. Their values are comprised between two extremes, the advancing (ϑ_{adv}) and the receding contact angles (ϑ_{rec}). Advancing and Receding CA (ARCA) measurements are usually performed by monitoring the CA variation during the addition and removal of liquid from the drop. In this experiment ϑ_{adv} and ϑ_{rec} values are calculated as the maximum and minimum CA that can be measured at the advancing or receding edge of the drop just before the motion of the three phase contact line.[184] Their difference is named contact angle hysteresis (CAH) and is of interest in many practical applications[185], besides providing information about the interaction energy between the liquid and solid and the wetting regime.[186]

The behaviour of drops on a surface characterized by heterogeneities or nano and microroughness cannot however be accounted for by Young's equation in the original form. Two modifications of 3.1 have been developed, the Cassie-Baxter and the Wenzel models. The first one applies to the cases in which air is trapped in the roughness, so that a heterogeneous interface, constituted by solid and air, is in contact with the liquid.[187] The Cassie's equation is therefore:

$$\cos\vartheta_{CB} = \phi_1 \cos\vartheta_1 \quad \phi_2 \cos\vartheta_2 \qquad 3.2$$

where ϕ_i is the projected area fraction of the components 1 and 2, namely solid and air, and ϑ_i is the correspondent Young contact angle. In the Wenzel model complete penetration of the liquid in the grooves or pores is considered. In this case, a roughness factor, r, is defined to take into account the higher contact surface per unit area.[188] The Wenzel's relation is:

$$\cos\vartheta_W = r \cos\vartheta_Y \qquad 3.3$$

Where r is the ratio between the actual wetted surface and the geometric surface. These equations can be used to extract the surface energy of a composite surface[189] or to determine the roughness of a porous solid.[186]

During the thesis work, contact angle measurements were performed by an OCA H200 (Dataphysiscs), equipped with two software-controlled motorized syringes. The set-up includes a stage where the sample is fixed, two 600 µm nozzles for liquid dispensing (2 more normal syringes can be mounted), an illuminator and a camera, that allows to acquire a magnified image or video of the drop. Starting from the collected screenshots the contact angle can be measured by the calculation of the tangent to the drop perimeter at three phase contact point. Fitting of the drop profile with a sphere, an ellipse or by Laplace-Young axisymmetric drop shape analysis are also possible and more suitable for ϑ > 90°. The system enables moreover dynamic measurements of ARCA.

II Experimental

Chapter 4

Materials and Methods

In this chapter a description of the experimental methods used is provided. In order to avoid repetitions, the chapter is organized in sections dealing with porous silicon preparation (4.1), silver nanoparticles synthesis (4.2) and characterization (4.3-4). These aspects are treated in parallel for the three SERS substrates typologies developed or applied in this thesis:

- Ag-coated porous silicon, synthesized by immersion plating (Ag-pSi, chapter 5)
- Ag nanoparticles stripes synthesized in situ on porous silicon by inkjet printing (printed Ag-pSi, chapter 6)
- Ag-coated porous silicon PDMS membranes (Ag-PSD, chapter 7) for microfluidic integration

Section 4.5 finally presents the biofunctionalization protocols for the inkjet printed samples and Ag-PSD membranes used for the detection of microRNAs.

4.1 Porous silicon electrochemical etching

Porous silicon anodization was performed in a Teflon cell with a circular aperture (d= 1 or 1.9 cm), starting from boron doped crystalline silicon wafers with resistivity between 34-40 mΩ-cm and <100> orientation. A 20:20:60 hydrofluoric acid-water-ethanol mixture was employed as electrolyte and a platinum foil was immersed as counter electrode. Silicon was etched in galvanostatic regime applying a current density of 80 mA for 30 s, unless elsewhere stated. Under these conditions a porous layer with a 64% porosity and 1.7 microns of thickness is produced. So prepared samples are simply referred as pSi (or pSi/Si to emphasize the fact that they are bound to the original Si wafer).

If needed, the detachment of the porous silicon membrane from the silicon substrate was attained by a second electrochemical attack in a diluted 4% HF mixture at a current density of 4 mA/cm^2 for 95 s. The as-prepared membranes were then transferred to a PDMS substrate, as detailed in section 7.2. Such samples are thereafter named PSD (or Porous Silicon-PDMS membranes).

4.2 Silver nanoparticles synthesis

4.2.1 Immersion plating

Silver nanoparticles were synthesized exploiting the reactivity of freshly etched porous silicon towards Ag$^+$ cations. Typically, a 10^{-2} M silver nitrate aqueous solution was prepared and heated at 50°C in a water bath. Different procedures were adopted for the two sample typologies:

- As prepared pSi/Si samples were directly immersed into the beaker for 60 s.

- A pre-treatment in a 10% HF aqueous solution was instead necessary for pSi-PDMS membranes (PSD). Concerning the immersion plating, higher temperatures and dipping time were employed (55°C for 5 minutes). In a modified plating solution, the effect of the addition of 2.5% ethanol and very small percentages ($6\ 10^{-4}$ %) of HF to the $AgNO_3$ solution was studied. In this case, the synthesis was performed at 50°C for 2.5 minutes.

After that samples were immersed in water to quench the reaction and dried with a nitrogen stream.

4.2.2 Inkjet printing

Different ink formulations were tested. Water:ethanol 1:1 (WE), water:DMSO 3:1 (WD) and water:DMSO 3:1 + ethanol 10% vol (WDE) mixtures were used to prepare $AgNO_3$ solutions at variable concentration ($2.5\ 10^{-2}$ M, $5\ 10^{-2}$ M). The inks were printed at room temperature (for WE) and at 65°C by heating the substrate plate of the inkjet printer (for WD and WDE), using a piezoelectric Jetlab 4-XL printer from MicroFab Technologies Inc. (Plano, TX, USA) equipped with a 60-µm nozzle diameter MJ-AT-01 dispenser. For the WE ink, the waveform of the electrical bias used to eject a single droplet was a 35 V pulse lasting 24 µs, followed by a −35 V pulse lasting 80 µs as echo dwell with the rise, fall, and final rise time of 13, 23, and 10 µs, respectively; for the WDE and WD mixture, the waveform consisted in a 26 V pulse lasting 20 µs, followed by a −35 V pulse lasting 40 µs as echo dwell with the rise, fall, and final rise time of 21, 13, and 5 µs, respectively. The effect of the step size (drop-to-drop distance) and the number of printhead passes on the obtained nanostructures morphology was studied.

4.3 Optical and Morphological Characterization

Specular reflectance spectra were recorded by means of a CARY5000 UV-Vis-NIR spectrometer, both to extract (i) the thickness and porosity of the etched pSi layers and (ii) to check the optical response of the SERS substrates after the synthesis of the nanoparticles. To the first aim, spectra were acquired in a wide spectral range (200-3000 nm) in order to maximize the number of the Fabry-Perot interference fringes due to the presence of a thin pSi layer. SCOUT 2.3 software was employed for the reflectance spectrum simulation, setting the porosity and thickness as fit parameters. Spectra of the silvered samples were instead recorded in the 200-1500 nm range.

Morphological characterization was performed by the SUPRA 40 FESEM system. Typical imaging parameters for conductive samples were 5 kV as acceleration tension, 5 mm as working distance and 30 µm as aperture. An In Lens detector for secondary electrons was employed.
In case of PSD membranes, where the insulating PDMS layer is present, the Ag-coated samples were covered with a copper grid anchored to the FESEM stub to allow discharging.

4.4 Raman Characterization

Raman measurements were performed by a Renishaw InVia Reflex Raman Microscope, in a backscattering configuration. 4-mercaptobenzoic acid (4-MBA), Rhodamine 6G (Rh6G), and Cyanine-5 (Cy5) were employed as Raman probe molecules to investigate different properties of the SERS substrates. The experimental conditions of the Raman tests are reported in the followings.

4.4.1 4-mercaptobenzoic acid Raman detection and mapping

Samples were incubated in 4-MBA according to two different protocols. The first one (protocol 1) was developed at Bonifacio’s lab in Trieste as systematic tool for the comparison of the performances of different SERS substrates (as an example, Ag-PDMS obtained by DC sputtering of silver onto PDMS slices and paper fibers impregnated with silver and gold colloids were also subjected to this protocol). Protocol 2 was tailored for the high resolution Raman mapping of inkjet printed and pSi-PDMS membranes.

During the tests performed in Trieste (protocol 1), 4-MBA was dissolved in methanol at 10^{-3} M concentration. Aqueous 4-MBA solutions were prepared by dilution in water and used to incubate the Ag-pSi SERS substrates for 5 minutes. Samples were gently rinsed with water after the incubation. Three laser sources were used to excite the samples: a 785 diode laser (Toptica) with a 500 mW output power, a 632.8 nm HeNe laser (Melles-Griot, 35 mW) and a 514.5 nm Ar-ions laser (Modulaser, 50 mW). A 50 x objective was employed for single point measurements.

As for protocol 2, the dissolution of crystalline 4-MBA was attained in ethanol at 10^{-2} M concentration. Dilutions were also performed in ethanol and used for the incubation of the samples (printed Ag-pSi and Ag-PSD) for 30 minutes. After that, the SERS substrates were rinsed with ethanol before the SERS measurements at 514.5 nm under a 50 x objective.

The uniformity of the SERS enhancement was assessed by mapping measurements. Samples incubated with protocol 1 were analysed under a 10 x objective. This magnification was chosen in order to extend the applicability of the method to non-planar substrates such as paper substrates. Raman imaging was performed on 4 replicas at 514.5, 632,8 and 785 nm, reducing the laser power on the sample by filters (50% and 1%) for the two last wavelengths and by defocalization of the incoming beam by a factor of 70%, 80% and 90%, respectively. Maps were acquired on a 400 µm x 400 µm area with a 50 µm step, resulting in 89 collected spectra per map.

SERS substrates incubated according to protocol 2 were analyzed under a 50x objective. 50 microns x 50 microns Raman maps (5 µm step) were acquired. The laser power of the 514.5 nm line was filtered to 1-0.5%. 1 s of exposure time and 2 accumulations were used for the mapping measurements.

4.4.2 Rhodamine 6G detection

Rhodamine 6G dissolved in ethanol was diluted to prepare a set of solutions ranging from 10^{-6} M to 10^{-14} M. In a typical test, 0.2 µl/mm^2 of the selected solution were spotted on the SERS substrate surface. After drying, the Raman spectrum was recorded. Laser excitation was performed by a 514.5 nm line, namely in electronic resonance. Spectra were recorded under a 50x objective (0.75 numerical aperture).

4.4.3 Cyanine 5 detection

Cyanine-5 dissolved in ethanol at 10^{-4} M concentration was diluted to prepare 10^{-6} M solutions, used for the impregnation of printed Ag-pSi for 30 s. Samples were left to dry before the SERS measurements.

4.5 Biofunctionalization for miRNA detection

Before the development of the protocol for the biofunctionalization of nanoparticles, the compatibility of the three SERS substrate typologies with the buffers required for the bioassay was tested.

4.5.1 SERS substrates stability in buffers

As for the buffer resistance, the integrity of the SERS substrates was assessed by FESEM imaging and SERS efficiency measurements (with R6G, as explained in section 4.4.2) before and after the overnight incubation in the following buffered solutions: NaAc (1% BSA in 50 mM sodium acetate buffer pH 4.0), TE (10 mM Tris, 1 mM EDTA, pH 7.5), TE-t (TE, 0.05 % tween20™, pH 7.5), TE-NaCl (TE, 1M NaCl, pH 7.5), TE-NaCl-t (TE-NaCl, 0.05 % tween20™, pH 7.5), SSC 4x (from stock 20x (60 mM trisodium citrate, 600 mM NaCl, 0.1 % SDS, pH 7.5)) and SSC 1x (diluted from SCC 4x). The samples were rinsed with milliQ water and dried with a stream of nitrogen before the repetition of the Raman and FESEM measurements.

4.5.2 Bioassay protocol

Samples were first pre-treated to reduce the nonspecific binding of the oligo probe and the target to the porous silicon and silver substrate. To this end, they were incubated in 1% BSA NaAc buffer for 1 h. After that, the SERS substrates were washed in TE buffer to remove the excess protein.

5’-alkylthiol-capped DNA probes (probe222, 5’-C6SH-ACCCAGTAGCCAGATGTAGCT-3’), corresponding to the antisense sequence of the miRNA222, were used to detect the complementary RNA sequence. The thiolated probe was reduced with DL-dithiothreitol (DTT), separated from the reductant by size-exclusion in a Illustra MicroSpin G-25 column and quantified by means of UV spectroscopy using the Cary5000 UV-Vis-NIR spectrophotometer equipped with a TrayCell (Hellma GmbH & Co., Müllheim, Germany).

Just after the reduction with DTT, the probe was diluted to the working concentration (100-1 µM) in Te-NaCl buffer. 5 µl of this solution were used for the overnight drop-incubation of each SERS substrate at room temperature. Subsequently the samples were washed three times in TE-t for 5 minutes and further blocked with BSA for 1 h.

The hybridization step was performed by incubation of 25 µl of the target miRNA, diluted in SSC 4x at different concentrations, for 1 hour, followed by washings in SSC 1x and milliQ water.

All the employed volumes were 4 µl in case of the application of the bioassay to the optofluidic chip.

4.5.3 Raman analysis

SERS spectra of the functionalized and hybridized samples were acquired with the 514.5 nm laser. The laser power was reduced to 0.05% in order to avoid the degradation of the biological samples. Raman mapping (100 µm x 100 µm maps, 5 µm step size) was performed to average the signal over a larger area. Data analysis was carried out by the hyperSpec[190] R[191] package.

Chapter 5

Silver coated porous silicon SERS substrates

5.1 Introduction

This chapter deals with a critical analysis on the SERS properties of silvered porous silicon substrates (Ag-pSi), both at the fundamental and at the application level. Indeed, although previous works have demonstrated the ultrasensitivity of Ag-pSi SERS substrates, other important features have to be considered for practical applications in analytical and bioanalytical chemistry, such as the Raman signal intra-substrate uniformity and inter-substrate reproducibility. Moreover, a better understanding of the SERS response of the substrate is needed to optimize the detection conditions and to avoid misleading interpretations of the collected data. A systematic study of the Ag-pSi SERS performances at excitation wavelengths spanning from the visible to the NIR range (514.5 nm, 633 nm and 785 nm) is therefore performed. The comparison between the experimental results with 3D finite element method (FEM) modeling, which shows a good agreement, provides new relevant insight into the plasmonic properties of Ag-pSi SERS substrates.

5.2 Application of a systematic protocol to probe SERS substrates

It is worth to underline that the assessment of the SERS properties of a SERS substrate doesn't rely on any standardized protocol, as thousands of publications appear presenting diverse strategies. This is particularly problematic due to the strong influence of the experimental conditions, including how the analyte is delivered onto the NPs surface, the adsorption and optical properties (Raman cross sections and the possibility of electronic resonance) of the probe molecule and the chosen excitation wavelength, on the reported results. A careful design of the experiments is therefore needed to minimize the above mentioned variability. In the followings, after the choice of a suitable analyte, a systematic study, comprising the morphological and optical characterization of the SERS substrate, the assessment of its Raman efficiency and the determination of the average SERS signal intensity, uniformity and reproducibility in the widest range of wavelengths achievable aims to give a comprehensive description of Ag-pSi SERS substrate properties.

5.2.1 Analyte selection: Rhodamine 6G vs 4-mercaptobenzoic acid

Figure 5.1 shows the absorbance spectra of two typical SERS probe molecules, Rhodamine 6G (Rh6G) and 4-mercaptobenzoic acid (4-MBA). The first one is characterized by an intense absorption band around 520 nm, thus enabling resonant excitation with the 514.5 nm laser line. On the contrary, 4-MBA, being representative of a class of mercaptobenzenes, only displays two absorption bands in the UV region at 217 and 271 nm. Consequently, small variations of 4-MBA Raman cross section are expected in the visible-NIR range. SERS spectra of Rh6G and 4-MBA acquired on Ag-pSi substrates at increasing concentrations are shown in Figure 5.2. Peak assignments are reported in Table 5.1. It can be noticed that Rh6G provides a Raman signal starting

4-MBA

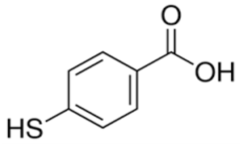

Raman shift (cm^{-1})	Assignment
1075	ring breathing (ν_{12}, a_1) +ν C-S[192]
1137	δC-H (ν_{15}, b_2)[193]
1180	δC-H (ν_9, b_1)[40,193]
1380	COO^- stretching[192]
1584	ring breathing (ν_{8a}, a_1)[192]

Rh6G

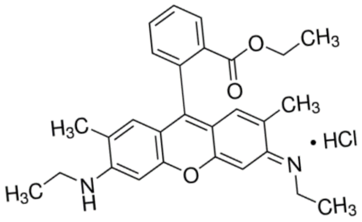

Raman shift (cm^{-1})	Assignment
612	C−C ring in-plane bending in xanthene/phenyl rings[194,195]
774	C−H out-of-plane bending[194,195]
1127	C−H in-plane bending in xanthene/phenyl rings[194,195]
1184	C−H plane bending in xanthene ring[195]
1204	C−H plane bending in xanthene ring[195]
1275	hybrid mode (xanthene/ phenyl rings) [195]
1309	hybrid mode (xanthene/ phenyl rings and NHC_2H_5 group) [195]
1364	C−C stretching in xanthene ring[195]
1449	C-N stretching in NHC_2H_5 group[195]
1509	C−C stretching in xanthene ring[195]
1575	C−C stretching in phenyl ring[195]
1595	hybrid mode (phenyl ring with $COOC_2H_5$ group) [195]
1650	C−C stretching in xanthene ring[195]

Table 5.1. Band assignments for 4-MBA and Rh6G SERS spectra.

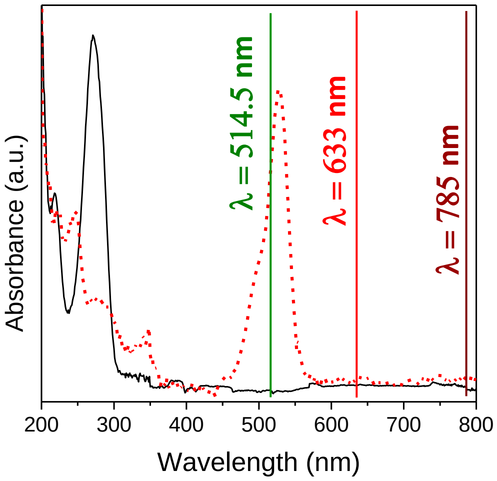

Figure 5.1 UV-Vis absorbance spectra of 10^{-3} M 4-MBA acid (black solid line) and 10^{-4} M Rh6G (red dashed line). Vertical lines mark the excitation wavelengths employed in this study. Spectra were normalized to the maximum intensity

from 10^{-12} M under 514.5 nm excitation. Note that Rh6G peak relative intensities are characterized by fluctuations at low concentrations, ascribed to local chemical enhancement effects in single molecule SERS[1]. In agreement with rough calculations, which show that for a micrometric laser spot and 0.2 µl/cm^{2} of solution, single molecule regime is expected at concentrations lower than 10^{-11} M, this result underlines the few/single molecule detection capabilities of the Ag-pSi substrate. On the other hand, 4-MBA is detected at concentrations as low as 5 10^{-8} M, since the absence of the analyte electronic resonance contribution. The External Amplified Raman Efficiency (see section 1.2.3) of Ag-pSi is derived from the experimental data to estimate its Raman enhancement. As the Raman spectra of Rh6G and 4-MBA on bare pSi can only be acquired at 10^{-4} M and 10^{-1} M concentration for the two analytes, the EARE is 10^{8} and 2 10^{6}, respectively. Although the huge difference observed for the lowest detectable concentration of the two probe molecules is mitigated by the calculation of the EARE, which is independent of the Raman cross section of the analyte, the residual discrepancy is difficult to explain, but has been already reported in the

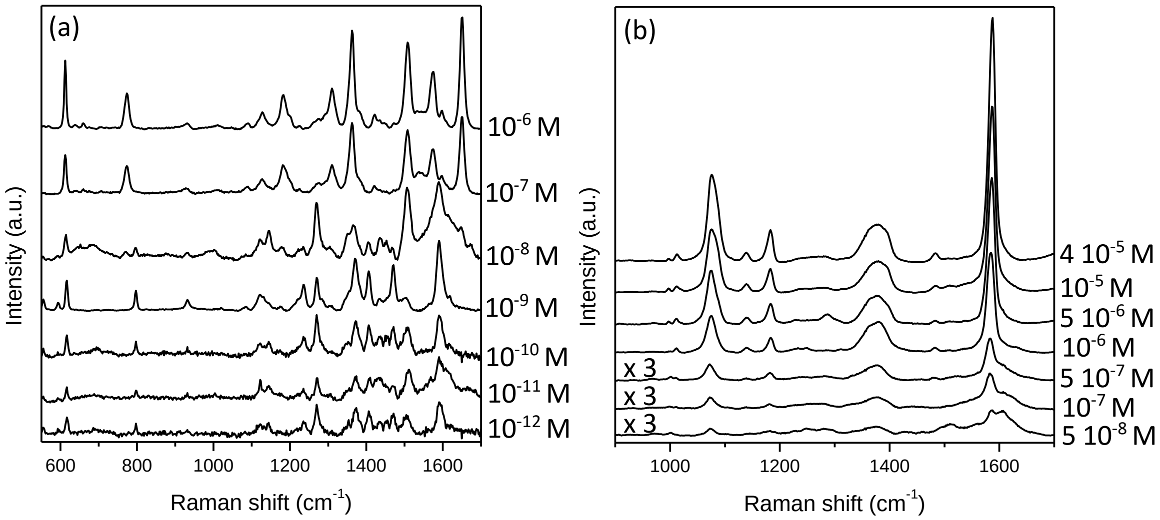

Figure 5.2. SERS spectra of (a) Rh6G and (b) 4-MBA at several concentrations acquired at 514.5 nm. Spectra are rescaled by the factors indicated on the graph.

---

[1] The origin of this phenomenon has been analysed in detail elsewhere[43] and is not the focus of this discussion.

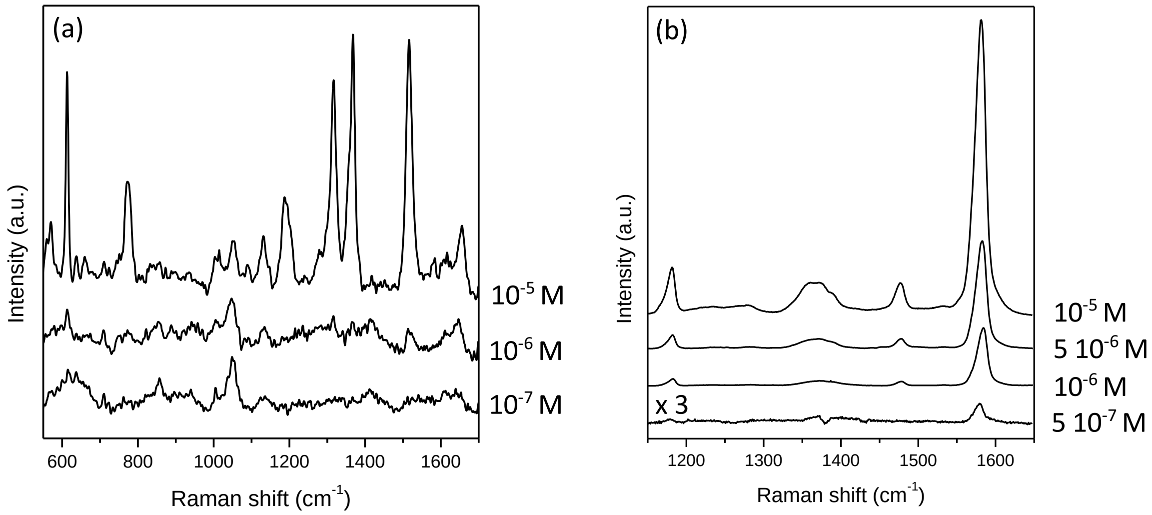

Figure 5.3. SERS spectra of (a) Rh6G and (b) 4-MBA at several concentrations acquired at 785 nm. Spectra are rescaled by the factors indicated on the graph.

literature.[196] It can be tentatively ascribed to an additional contribution of the chemical enhancement for Rh6G in electronic resonant conditions. Figure 5.3 displays a similar series of spectra for the two analytes excited at 785 nm. In this case the probe molecules are detected almost at the same concentration in the SERS experiment. 4-MBA spectrum on bare pSi is again detected after incubation with the 10^{-1} M solution. As for Rh6G, concentrations higher than 10^{-3} M were not available, however many works agree on its resonant vs non-resonant Raman cross section and estimate the difference as 3 orders of magnitude.[16,197] Taking into account this information, the EARE calculated for Rh6G and 4-MBA at 785 nm is 10^5 and 2 10^5. This result suggests that far from the analyte electronic resonance the EARE is a reliable estimation of the SERS efficiency of the substrate. The factor 2 observed as discrepancy between the two values is reasonably due to the approximations made for the EARE calculation.

It should be noted that Rh6G provides information about the best possible sensitivities for a SERS substrate. Nevertheless, the result is not easily comparable to practical SERS analysis. Indeed, many analytes and bioanalytes cannot benefit from an electronic resonant excitation in the Vis-NIR range (SERS under UV excitation cannot always be applied as samples can undergo photodegradation). Rh6G can be however a useful probe molecule for substrates being applied in the framework of assays employing dye-labelled probes. On the other side, 4-MBA non-resonant behaviour shares similarities to the case of label free detection. Moreover, two important advantages indicate 4-MBA as the analyte of choice to test the properties of the SERS substrate: first, it is suitable for comparative studies at different wavelengths, as only the intrinsic SERS response of the nanostructures is responsible for the observed Raman enhancement upon excitation at the most commonly employed excitation energies. Secondly, the thiol group of 4-MBA should ensure a stable bonding to the silver surface. For this reason, after the incubation in the analyte solution, the sample can be gently rinsed with the solvent to avoid the formation of multilayers or aggregates, improving the reproducibility of the test. Further systematic analysis on Ag-pSi employs therefore 4-MBA as probe molecule.

5.2.2 Wavelength dependence of Raman efficiency

The previous section has highlighted the variations in the SERS enhancement due to the electronic properties of the probe molecule. Now, the discussion will focus on the intrinsic properties of Ag-

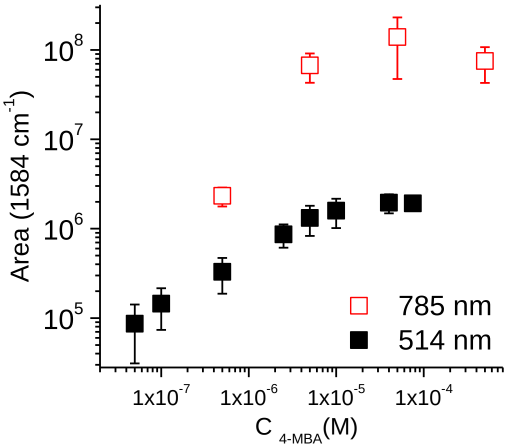

Figure 5.4 Integrated areas of 4-MBA peak at 1584 cm^{-1} vs analyte concentration, calculated for Ag-pSi excited at 514.5 and 785 nm. Y axis is plotted in log-scale to allow a better comparison.

pSi substrates. The calculated EARE for 4-MBA at 514.5 and 785 nm (2 10^6 vs 2 10^5) points out that Ag-pSi is characterized by a higher SERS efficiency upon visible excitation. Further inspection of the data reveals however an unusual SERS response. Figure 5.4 reports a plot of the SERS intensity of 4-MBA 1584 cm^{-1} peak (the integrated area of the peak is calculated) versus the analyte concentration at 514.5 and 785 nm. The TO-LO c-Si peak intensity (520 cm^{-1}) measured at the two wavelengths is taken as a reference in order to normalize the spectra. This method enables a reliable comparison between the measurements with different laser lines, as it considers both the wavelength dependence of Raman effect (whose efficiency is directly proportional to $1/\lambda^4$) and the spectral response of the spectrophotometer. Surprisingly, the SERS intensity is more than one order of magnitude higher at 785 nm for all the measured solutions. Moreover, despite the low number of measurements, it can be noticed that the spatial SERS signal variability is higher for NIR excitation. These issues are addressed in detail in the next sections.

5.2.2.1 Morphology and optical analysis of Ag coated pSi

Figure 5.5 (a) shows the FESEM micrograph of a typical Ag-pSi sample, synthesized by immersion plating of pSi (average pore dimension ~2–20 nm) in a 10^{-2} M silver nitrate aqueous solution. The size and inter-particle gap distribution histograms were extracted through the numerical analysis of the images (100 kx magnification), covering an area of 10 µm^2. A wide polydispersion of the Ag NPs, characterized by an average equivalent diameter of around 100 nm is observed. The particle

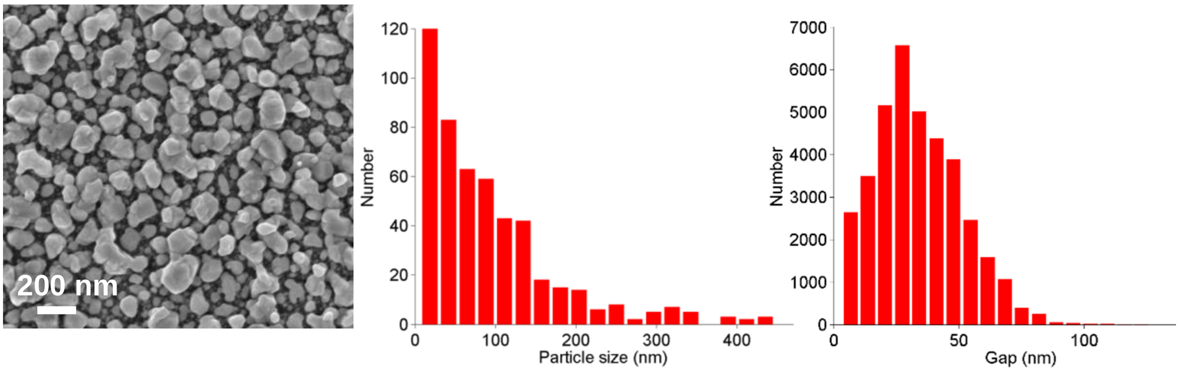

(a) (b) (c)

Figure 5.5 (a) FESEM image of Ag NPs synthesized on mesoporous silicon by dipping in a $AgNO_3$ 10^{-2} M solution for 60 s at 50°C; (b) Particle size (expressed as equivalent diameter) and (c) inter-particle gap distribution histograms.

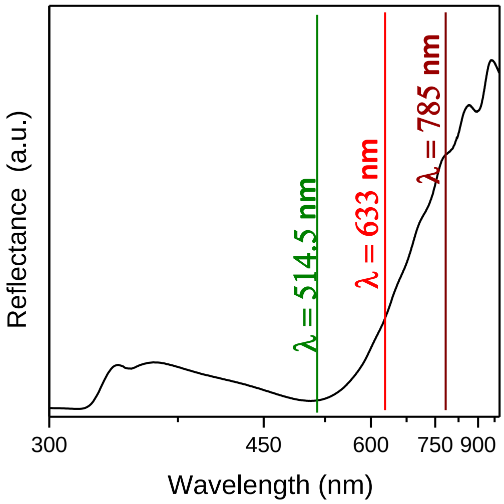

Figure 5.6 Typical specular reflectance spectrum of Ag-pSi samples shown in figure 5.5.

sizes cover a large range (5 nm-400 nm), as witnessed by the histogram distributions in Figure 5.5 (b). Such a large dispersion can be justified taking into account the immersion plating growth mechanism: after the first nucleation steps, most of the particles increase their size, after which new populations with small size appear within the interstices between the larger particles. An average inter-particle gap of around 25 nm with a RSD=48% can be instead calculated. Following the literature, inter-particle interactions in the gaps occur under light excitation when the particles separation is shorter than their radius.[81] An optical response of the substrates dominated by LSPRs coupling is therefore expected. Moreover, a certain fraction of nanometric-sized gaps can be identified on the left side of the histogram in Figure 5.5 (b), suggesting the presence of efficient Raman hot-spots due to the huge electric field concentration in very small gaps.

UV-Vis specular reflectance spectra (Figure 5.6) of Ag-pSi are in agreement with the detected morphology. A broad dip around 500 nm, due to the enhanced absorption and scattering of the plasmonic NPs, is observed. The large width reflects the heterogeneity of particle size and inter-particle interactions, being the convolution of the many LSPRs associated to the different NPs families and assemblies. In the past, the optical response of metal-dielectric nanostructures has been considered as an optical fingerprint, to be used in SERS experiments as a tool for the selection of a suitable excitation wavelength. On the other hand, SERS substrates were also optimized by matching the LSPR band with the available laser lines. According to Ag-pSi reflectance spectrum, the maximum SERS enhancement is expected at 514.5 nm, with a weakening when the excitation wavelength is red-shifted. It is however important to note, that the optical response of a SERS substrate measured by UV-Vis-NIR spectroscopy results from the observation of far-field propagating plasmonic modes, but cannot give information about near-field electromagnetic processes. Indeed, the recent literature has analyzed the dark plasmons in strongly coupled nanostructures[198] underlining in some cases their contribution to huge SERS enhancements.[33]

3D-Finite Element Method can provide an insight into the EM near-field features of plasmonic assemblies. A simple model consisting in dimers of Ag hemispheres deposited on porous silicon is selected to simulate the near field response of Ag-pSi substrates. The contribution of the semiconductive matrix is taken into account through the dispersion of the dielectric function of pSi, while different particle sizes (50 nm and 100 nm) and inter-particle spacings are considered (from 300 to 1 nm). The EM near field spectra calculated within the gap for a hemisphere diameter = 100 nm, which is representative of the average NPs size on pSi, are collected in Figure 5.7 (a) for several

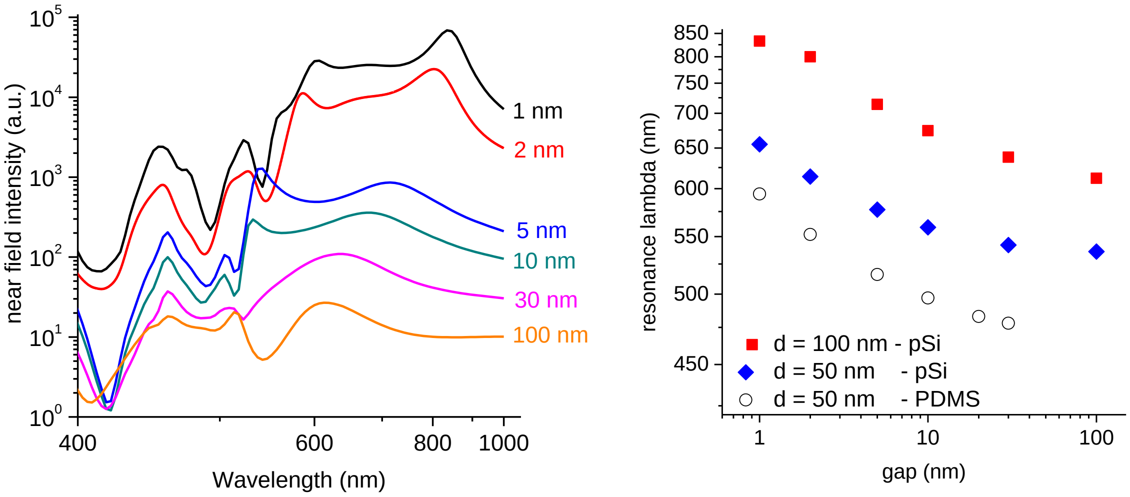

(a) (b)

Figure 5.7 (a) EM near field intensity spectra for a dimer of Ag hemispheres supported on porous silicon (sphere diameter = 100 nm) with different nanogap sizes. (b) Lowest energy resonance wavelength, extracted by the modelled spectra, for hemispheres supported on pSi (sphere diameter =100 and 50 nm) and PDMS (sphere diameter = 50 nm), versus the dimer inter-particle spacing.

inter-particle distances. Multiple resonances are observed, spanning over the visible and NIR wavelength range. The highest EM near field intensities are found for the smallest gaps. Moreover, the resonance featured by the lowest energy undergoes a red shift by reducing the inter-particle spacing. On the contrary, for gaps larger than 100 nm an asymptotic value is reached both for the resonance positions and intensity (data not shown). Figure 5.7 (b) highlights this shift for the maximum wavelength position as a function of the inter-particle gap at d=100 nm and 50 nm. The same trend is observed for the different particle sizes, but a lower maximum wavelength is attained for smaller NPs. It should be noted that for gaps below 5 nm and d=100 nm the main resonance is located in the NIR range, around 800 nm. This marked red-shift is higher than those found for PDMS supported closely spaced dimers characterized by the same geometrical parameters.[199] A third series of calculations, extracted from the recent work of Giorgis' group about silver-coated PDMS SERS substrates, is also reported in the plot of Figure 5.7 (b). Data were obtained by the same simulation method for a hemispheres dimer with d=50 nm. The comparison between the two matrixes reveals a blue shift of the maximum wavelength of PDMS supported dimers for all the calculated gaps. It can be therefore concluded that the higher refractive index of porous silicon with respect to other common supports, such as glass slides, silica or polymers, influences the plasmonic properties of the supported NPs, contributing to an additional red shift of the resonance wavelength, in agreement with previous literature[37,38], and to the wide tunability of the LSPRs, typical of Ag-pSi.

Although the dimer representation is an extreme simplification with respect to the complexity of the real morphology of the nanostructures, it evidences the possibility of plasmon resonances in the NIR range, that couldn't be observed by UV-Vis-NIR spectroscopy. However, as stated before, the reflectance spectra can typically detect far-field propagating light, while the near-field modes evidenced by the FEM modeling in terms of intense high-wavelength resonances in the range of 700-850 nm could be responsible for the experimentally determined higher SERS intensity under excitation at 785 nm.

5.2.2.2 Raman mapping

SERS signal intensity and uniformity are probed by Raman mapping of Ag-pSi after samples incubation in aqueous 4-MBA solutions at 10^{-5} M concentration. Four SERS substrates, sharing a common optical response and prepared under the same synthesis conditions, were tested at each wavelength. A 10x objective was employed, because it shows a wider applicability both for non-planar samples and for on-site measurements, where a high resolution is not possible. An integration of the intensity over the area of 4-MBA most intense peak at 1584 cm^{-1} was performed to compare the measurements. Figure 5.8 displays a box-plot representation of the data extracted by the SERS maps along with a histogram showing the average SERS intensity at the different laser energies (averaged over the 4 repetitions). In detail, the graphical representation is a Tukey's box plot, where the SERS intensity data are depicted through their quartiles.

It can be inferred from these plots that the enhancement provided by Ag-pSi under the specific experimental conditions is the lowest at 514.5 nm, weakly increases at 633 nm and reaches its maximum value by irradiation at 785 nm. However, the rise in the signal intensity is associated to a higher intra-substrate variability, as also shown in figure 5.9, where three representative false colour images, derived from the SERS maps acquired at 514.5, 633 and 785 nm, depict the integrated intensity of 4-MBA peak centered at 1584 cm^{-1}. These images qualitatively inform about the heterogeneity of the SERS signal throughout the surface of the substrate, and thus about the intra-substrate repeatability of the collected spectra. A normalization by the average SERS intensity of an arbitrarily chosen sample was performed to plot the false colour maps in the same intensity range. This operation emphasizes the differences in the intensity variability among the three excitation wavelengths, which clearly increases moving from 514.5 nm to 785 nm. It is worth to underline that the SERS intensities don't exhibit a Gaussian distribution. A similar behaviour has been reported by Brolo's group for self-assembled multilayers of NPs.[82] In their paper the non-gaussian profile was explained by an incomplete coverage of the support surface, leading to a non-homogenous particle arrangement. Indeed, a normal distribution of the intensities was attained

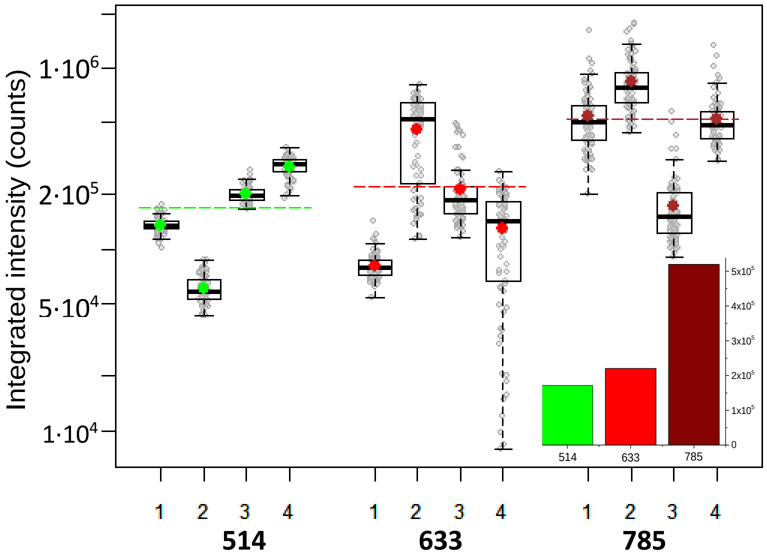

Figure 5.8 Box-plot representation of the SERS intensity distributions calculated at the three investigated wavelengths for four Ag-pSi samples. The line within each box is the median and the lower and upper boundaries of the box indicate first and third quartiles respectively. Error bars (whiskers) indicate the 1.5-fold interquartile range (IQR). Intra-substrate and inter-substrate means are marked by the dots and the dashed lines respectively. The inset shows the SERS intensities histogram at the three wavelengths

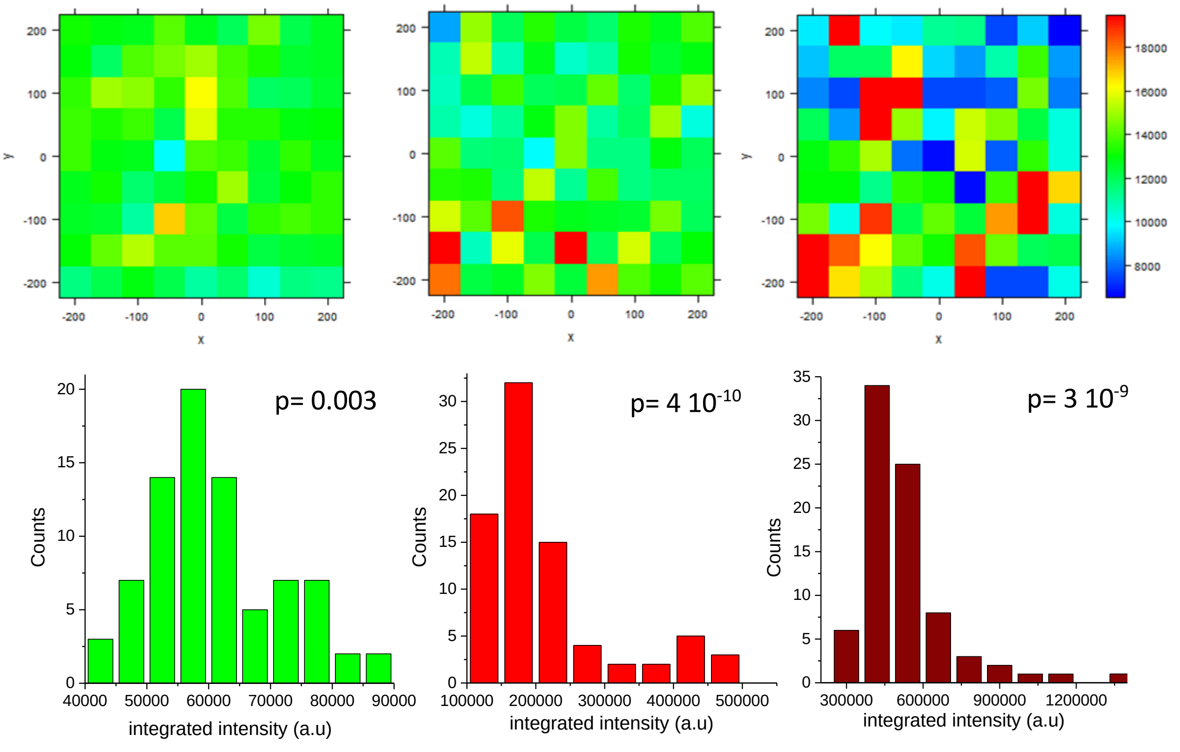

(a) (b) (c)

Figure 5.9 False colour maps of the integrated area of the 1584 cm^{-1} 4-MBA peak and relative intensity distribution histograms obtained by the SERS maps acquired at (a) 514.5 nm, (b) 632.8 nm and (c) 785 nm. p-values extracted by the Shapiro normality test are reported for each distribution.

after an optimized number of self-assembly cycles. In case of Ag-pSi the non-normality is therefore probably due to the heterogeneity of plasmonic assemblies giving rise to the SERS effect. The application of the Shapiro-Wilk test for normality underscores however remarkable differences between the investigated excitation energies. The deviation from a normal distribution is higher at 633 and 785 nm. The calculated Shapiro p value, which assesses the normality of the tested distribution if > 0.05, is found to be extremely low at these wavelengths (around 10^{-5} /10^{-6} at 633 nm and 10^{-11}/10^{-9} at 785 nm), while it is in the 0.5-0.001 range at 514.5 nm. Although this aspect is not considered in most of the studies about SERS substrates, it suggests that the Relative Standard Deviation may not be a suitable descriptor of the SERS signal variability for some nanostructures, as in the case of Ag-pSi samples. However, the RSD is commonly reported in papers, thus it is the only tool to compare the uniformity of Ag-pSi to other SERS substrates. For this reason, despite the lacking of statistical significance, Table 5.1 lists RSDs, along with means, medians and IQRs values for the integrated SERS intensities at all the employed laser lines. According to the recent literature, SERS signal intensity fluctuations in the range of 10-20% are usually considered a good result[108,200,201], while the RSD around 5% required for analytical grade quantitative detection is still a very challenging target.[154] In this framework, Ag-pSi samples exhibit an acceptable RSD of 12.3% only under 514.5 nm excitation, while values around 40 % are observed for the 633 and 785 nm wavelengths. In conclusion, from the point of view of practical applications, quantitative or semi quantitative measurements can only be foreseen for excitation at 514.5 nm. Irradiation of Ag-pSi samples at 785 nm enables instead very high sensitivities, but the analysis should be strictly qualitative.

	replica	mean	RSD	median	IQR
514	1	136294	9.3	135771	13836
	2	61253	17.1	59030	15081
	3	201788	10.3	198301	26071
	4	286649	12.8	294496	42259
633	1	81100	17.1	78696	14361
	2	455269	46.5	518662	409120
	3	215234	44.1	185590	63279
	4	129250	53.7	143508	117367
785	1	541379	40.8	502752	227685
	2	839864	35.9	778342	309176
	3	174691	48.3	152661	82075
	4	522325	34.5	481802	171643

Table 5.1 Summary of means, relative standard deviations, medians and inter-quartile ranges calculated from the SERS maps at the three excitation wavelengths

On the basis of the presented data, an explanation of the behaviour of Ag-pSi samples can be attempted, taking into account the complex morphology and heterogeneity of the nanostructures. FESEM image analysis shows that these SERS substrates are characterized by a large fraction of inter-particle gaps in the 20-30 nm range and by a smaller number of gaps below 10 nm. On the other side, FEM modelling evidences that only for very short inter-particle gaps strong near-field enhancement over 700 nm can occur. Hot-spots which can be resonantly excited at 785 nm are therefore only a minor part of the total scatterers. When samples are incubated at 4-MBA concentrations like 10^{-8}-10^{-7} M, the density of molecules adsorbed on the silver surface is quite low and thus the probability of molecular adsorption in the nanometric gaps and crevices between NPs, can be extremely low. Thus, despite the huge enhancement potentially provided by the smallest inter-particle gaps, the scattering system cannot yield a detectable Raman signal. On the contrary, if Ag-pSi is excited at 514.5 nm, the density of the resonant scatterers is much higher, including particle assemblies with larger spacing (20-30 nm) or smaller particle sizes. Consequently, even if the contribution to the overall enhancement of each inter-particle junction is lower, a detectable SERS signal can be collected starting from lower analyte concentrations. For 4-MBA high concentration regimes, the adsorption of the analytes occurs both in the nanosized and larger inter-particle gaps. In this case the higher amplification provided by the hot-spots between closely spaced nanostructures ensures a major 4-MBA SERS intensity for excitation at 785 nm than under excitation at 514.5 nm. The trend observed for the SERS intensity fluctuations also supports this hypothesis. Indeed, hot spots are characterized by an extremely high enhancement variability, because of the huge sensitivity of the EM near field intensity and distribution to the geometrical features of the inter-particle gap. High RSD can thus be related to this kind of SERS scatterers. More homogenous amplifications are instead obtained for excitation at 514.5 nm, due to the higher averaging degree. Finally, the proposed mechanism, which correlates the SERS behaviour of Ag-pSi at 514.5 and 785 to different SERS active nanostructure populations agrees well with the increased heterogeneity observed for the SERS intensity distributions in the NIR range. Actually, the long tail of sparse events characterized by huge and diverse SERS intensities, which are mainly responsible for the high RSDs, reflects the spatial heterogeneity of the more efficient SERS hot-spots.

5.3 Conclusions

In summary, the SERS properties of Ag-pSi substrates have been analysed by a combination of tools which are able to provide important information about both the origin of the SERS enhancement and on the practical use of these SERS substrates. From the first point of view, it was demonstrated that the SERS response at several wavelengths is consistent with the coupling of closely spaced nanostructures characterized by different geometrical features, showing LSPRs and therefore SERS activity under specific excitation energies. This determines a lower limit of detection (LOD) for Ag-pSi under 514.5 nm irradiation at low analyte concentration, while for 785 nm the LOD increases (despite the higher SERS intensity), as well as the increased SERS intensity variability in the NIR range. From the applicative point of view, reliable analysis with good SERS efficiency (EARE 2 10^6), as well as intrasubstrate uniformity (12.3 %) is only feasible at 514 nm, while qualitative highly sensitive detection can be performed under 785 nm excitation. Finally, this study highlights the complexity of the SERS response of a polydisperse multiple particle system, which therefore needs an accurate characterization to be used for real applications and provides a method that can be applied to the analysis of other SERS substrates.

Chapter 6

Inkjet Printed Arrays on Porous Silicon

6.1 Introduction

As discussed in the section 2.3.2.1, inkjet printing represents a low-cost, additive patterning technique suitable for the deposition of metal nanoparticles assembled in functional arrayed elements. In the framework of biosensing and bioanalytical applications this feature can be exploited to prepare efficient SERS active plasmonic arrays. This chapter presents a study on the development and optimization of SERS substrates consisting in ink-jet printed stripes on porous silicon. The AgNPs are synthesized in situ by printing silver nitrate based inks on the reducing freshly etched pSi surface. The influence of the printing parameters and of the ink composition on the obtained morphology is analysed and correlated to the observed SERS response.[202] Characterization of the optimized SERS substrates is performed using Rhodamine 6G regarding the SERS efficiency and 4-MBA to assess the intra substrate and inter-substrate repeatability at 514.5 nm.

6.2 In situ synthesis of silver nanoparticles via ink-jet printing

Contrary to most of the ink-jet printing applications, in which the pre-synthesized nanoparticles are suspended in the ink and simply deposited onto a substrate, direct writing on porous silicon samples has to consider that the reduction of silver cations occurs during the printing process. In this case the choice of the printing modalities or the solvents used are not only affecting the quality of the pattern, but also the NPs formation. Two main printing modes are usually available in commercial ink-jet printers, the “on the fly” and “Drop On Position” (DOP) ones. As for the first modality, the stage of the printer is continuously shifted under the printhead, while the dispensing position is controlled either by the set ejection frequency or by a quick check of the coordinates. In the second case, the stage is first moved to the desired point, where the drop is dispensed, and then moves towards the next point. Both modalities were tested, but only DOP, which allows a better control over the amount of ink dispensed at each spot, provides reproducible results. For the DOP modality two main printing parameters can be identified, namely the number of printhead passes repetitions and the distance between two adjacent printed drops. Their effect on NPs morphology is analysed in the following section.

6.2.1 Influence of printhead passes repetition and drop-to-drop step size

FESEM micrographs showing inkjet printed stripes of AgNPs on pSi are shown in figure 6.1. The pattern in Figure 6.1 (a) was drawn with an increasing number of printhead passes (from top to bottom, 1 to 6 passes). Continuous lines form as a consequence of adjacent droplet coalescence and the linewidth exhibits only a minor broadening upon addition of several passes. The stripes in Figure 6.1 (b) were printed instead at several drop-to-drop step sizes. Uniform lines are first attained at 1000 dpi (dots per inch), whereas the single drop spots are observed below this value. In contrast to the increase of the number of passes, the linewidth is almost tripled moving from 130 to 1300 dpi.

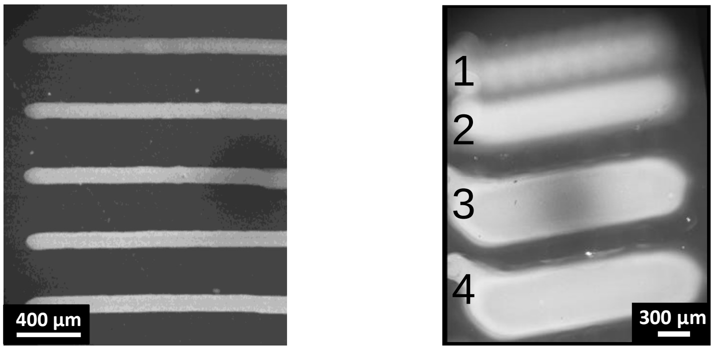

(a) (b)

Figure 6.1 FESEM images of patterned sample. Effect of (a) the number of printhead passes (1-6 from top to bottom) and (b) the inkjet step size: (1) 130 dpi, (2) 260 dpi, (3) 1000 dpi and (4) 1300 dpi.

Actually, taking into account the effect on nanoparticles morphologies, a similar trend is found for an increase in the number of passes or by reducing drop-to-drop distance. Due to discussed influence of the two parameters on the pattern quality, it is therefore convenient to fix the drop-to-drop step size at 1000 dpi, the limit for droplet coalescence, and to vary the number of passes. FESEM images acquired at high magnification on each stripe of the resulting pattern are displayed in Figure 6.2 (a) and show the morphological evolution associated to the increased number of passes from 1 to 6. The coverage percentage, expressed as the fraction of the image area coated by AgNPs, and the average inter-particle gap distribution were extracted by numerical analysis of the FESEM micrographs. Due to the morphology of these nanostructures, which show a significant degree of coalescence at high number of passes, the average particle diameter cannot be reliably calculated, but visual inspection clearly reveals bigger NPs sizes when the number of passes is increased. The plot in Figure 6.2 (b) summarizes the results of the image analysis. For each added printhead pass an increase of the Ag coverage is observed. At the same time, the interparticle gap distance is reduced, approaching an average values of ~ 28 nm for 6 printhead passes. Interparticle coupling can be therefore expected to provide Raman hot-spots for these samples, characterized by particle sizes over 100 nm. The decrease in the average interparticle gap is indeed reflected in

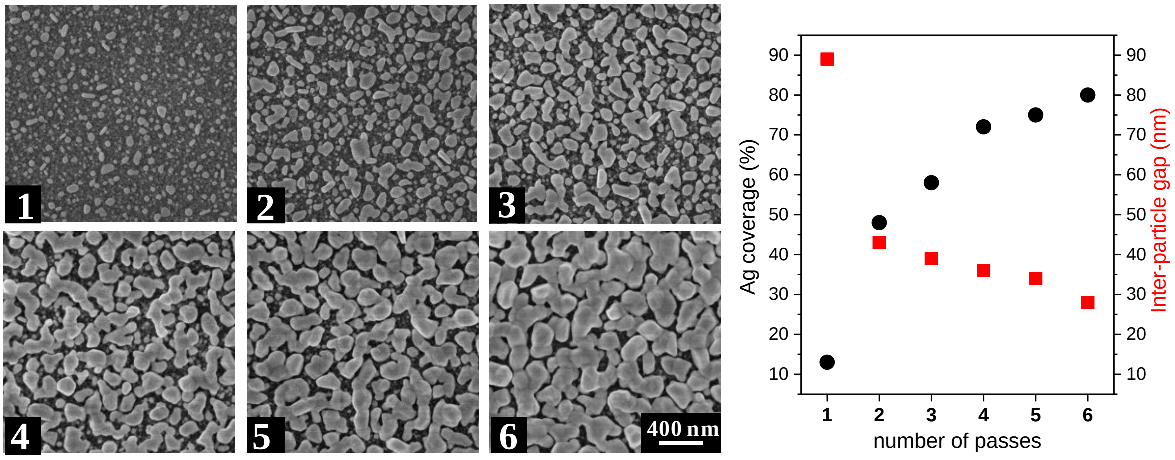

(a) (b)

Figure 6.2 (a) FESEM images of Ag NPs printed with water-ethanol (WE) ink, 2.5 10^{-2} M $AgNO_3$ concentration, 1000 dpi and variable number of passes (1 to 6) of the printhead on the porous silicon substrate. (b) Plot representing the trend of the Ag coverage (%) and of the average inter-particle gap vs. the number of passes

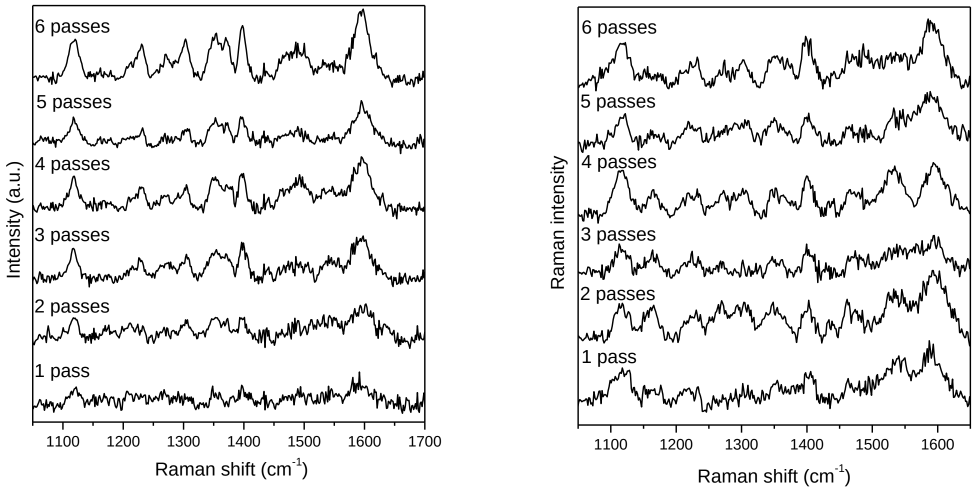

(a) (b)

Figure 6.3 SERS spectra of Cy5 (10^{-6} M) adsorbed on NPs synthesized at increasing number of passes (1 to 6) with (a) the 2.5 10^{-2} M and and (b) 5 10^{-2} M ink.

the SERS spectra acquired on the different stripes (Figure 6.3 (a)). Cyanine 5, excited in off-resonant electronic conditions at 514.5 nm, is used as probe molecule. After impregnation of the pattern in the dye solution, all the spectra are characterized by the typical Cy5 bands at 1605, 1500, 1230, and 1120 cm^{-1} corresponding to $v(C{=}N)_{stretch}$, $v(C{=}\ C)_{ring\text{-}stretch}$, $v(C\text{-}N)_{stretch}$, and $v(C\text{-}H)_{ip\text{-}bend}$ modes of the dye, respectively. However, while the spectrum is hardly emerging from the noise for the 1 pass stripe, the SERS signal intensity exhibits a monotonic increase and reaches its maximum for the 6 passes one, namely for the morphology characterized by the smallest interparticle gap sizes.

6.2.2 Influence of silver nitrate concentration

In addition to printing parameters, the composition of the ink can be varied to tune the morphological features of the inkjet printed Ag-pSi samples. The nanostructures shown in Figure 6.2 were synthesized employing an ink based on a 2.5 10^{-2} M $AgNO_3$ solution. Higher and lower metal precursor concentrations (10^{-2} M and 5 10^{-2} M) were also tested.

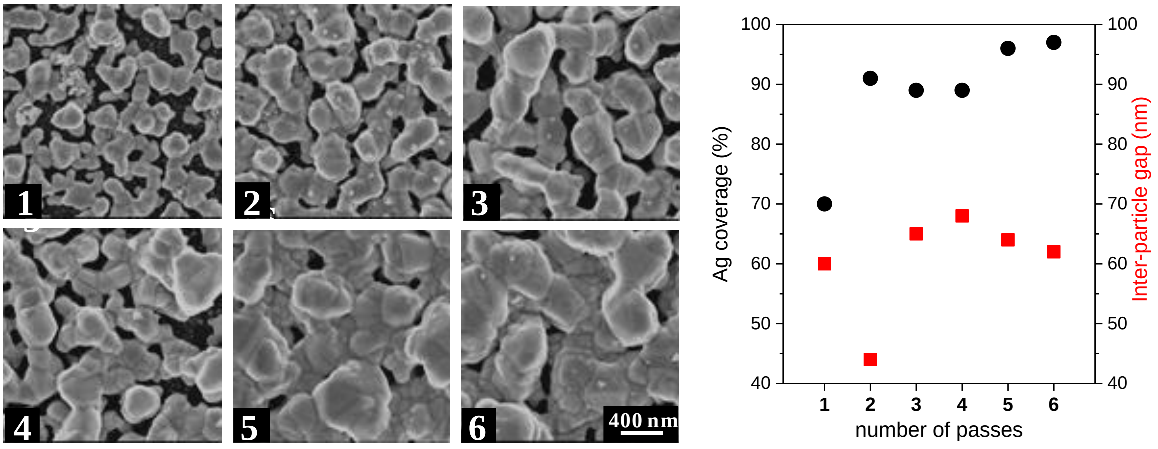

(a) (b)

Figure 6.4 (a) FESEM images of Ag NPs printed with water-ethanol (WE) ink, 5 10^{-2} M $AgNO_3$ concentration, 1000 dpi, and variable number of passes (1 to 6) of the printhead on the porous silicon substrate. (b) Plot representing the trend of the Ag coverage (%) and of the average inter-particle gap vs. the number of passes

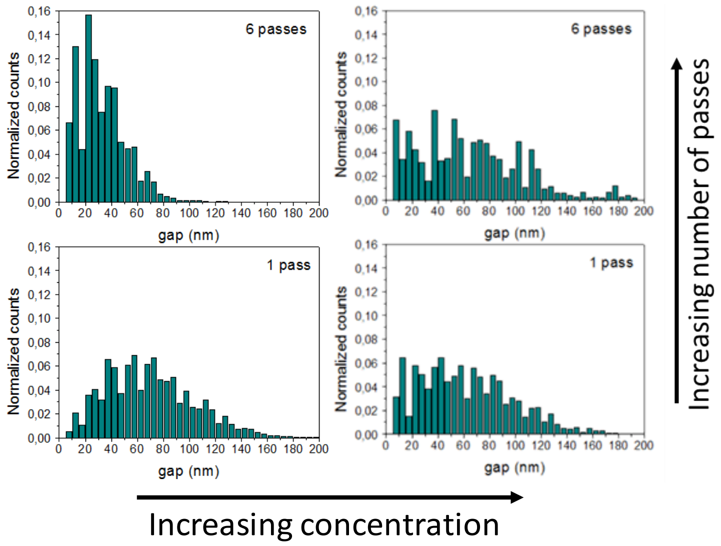

Figure 6.5. Inter-particle gap distributions of stripes printed at 2.5 10^{-2} M (left) and 5 10^{-2} M (right) $AgNO_3$ concentration with 1 and 6 passes; histograms are normalized to the total number of counts.

While the 10^{-2} M concentration provides very low particle densities also for a high number of passes, SERS active NPs can be synthesized with the 5 10^{-2} M ink. The FESEM micrographs of the obtained nanostructures are reported in Figure 6.4 along with the corresponding plot of the image analysis results as a function of the number of passes. Although the Ag coverage and the particle size increase moving from 1 to 6 passes, the average interparticle gap oscillates around 60 nm, without showing any trend. Histogram representations of the interparticle gap distributions calculated at 1 and 6 passes are compared in Figure 6.5 for the lower and higher concentrated inks. Indeed, at lower $AgNO_3$ concentration (2.5 10^{-2} M), the interparticle gap distribution is quite wide for a single printhead pass and it becomes narrower and narrower as the number of passes increases, shifting towards smaller gap values. On the contrary, for higher $AgNO_3$ concentrations (5 10^{-2} M) the gap size distributions are almost independent on the number of passes for what concerns the large width and the average value (the absolute number of gaps is however lower). This finding suggests a different growth mechanism at the two concentrations. While the small NPs enlarge their size by the addition of new silver atoms at the surface in case of the 2.5 10^{-2} M ink, coalescence of closely spaced NPs is probably the main growth process at the higher concentration.

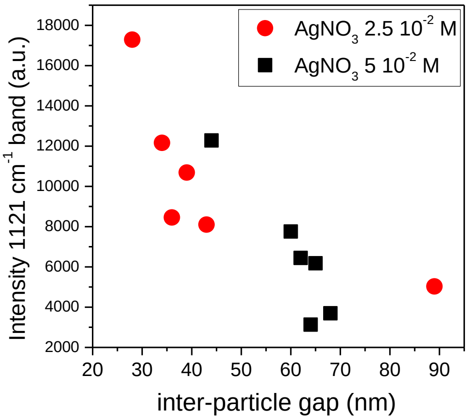

Figure 6.6 Integrated area of the 1121 cm^{-1} band of Cy5 *vs.* the average interparticle gap for stripes synthesized at 2.5 10^{-2} M (red circles) and 5 10^{-2} M (black squares) concentrations, shown in figures 6.2 and 6.4.

As expected, the SERS response of the six stripes synthesized with the 5 10^{-2} M ink is quite similar, showing only few apparently random fluctuations of the SERS signal intensity of Cy5 (Figure 6.3 (b)). However, if the area of the 1121 cm^{-1} peak is integrated for all the spectra presented in Figure 6.3 and plotted against the average interparticle gap size, regardless of the concentration and the number of passes employed, the data follow a common trend (see Figure 6.6). The SERS efficiencies of the synthesized nanostructures are therefore mainly determined by the average distance between nanoparticle protrusions. Although this is known for particle dimers[29] and well-ordered systems[31], this is verified also on such discussed complex morphology.

6.2.3 Influence of ink properties

Table 6.1 collects the experimentally determined properties of the three tested inks. The solvent mixtures were optimized to allow a good printability, reducing the risk of satellite drop formation due to the low viscosities of the starting components (2 cP for DMSO, ∼ 1 cP for water and ethanol). Moreover, ink properties also determine the quality and resolution of the pattern and influence the synthesis process of the NPs. First of all, the wettability behaviour of the substrate with respect to the used inks has been assessed and compared to standard liquids. Freshly etched porous silicon shows a very high water CA of 135°, in agreement with the almost superhydrophobic behavior reported in previous articles for electrochemically etched mesoporous silicon prepared in high current density regimes.[186] Standard liquids, characterized by a major non-polar contribution to their surface tension, such as diiodomethane, provide instead very low contact angles. After the impact on the surface the drop quickly percolates into the pores reaching a steady CA of 15.6° in few milliseconds. This combined behavior towards the two test liquids has been previously observed for spongiform aggregates of carbon nanotubes[203], which show superhydrophobicity related to the extremely high roughness of the nanostructured surface, but have good affinity to low-polarity fluids, as can be also reasonable for the Si-H_x rich porous silicon surface. ARCA measurements on pSi highlight moreover the existence of a huge hysteresis between the advancing CA (147°) and the receding one (19°). This result is indicative of a strong pinning of the three phase contact line, typical of such rough surfaces characterized by a Wenzel wetting regime (pores are filled by the liquid). The formation of continuous stripes is therefore expected for high water content ink formulations due to the sticky behavior of the drop.

Figure 6.7 reports the snapshots of the ink drops deposited on porous silicon along with the corresponding printed patterns. The contact angle values follow the trend of the ink surface tensions, with the highest CAs associated to the WD ink (123.9 $\pm$ 0.9%) followed by WDE ink (109.3° $\pm$ 1.3%). An accurate estimation of WE CA was not possible, because a complete splash of the ink drop occurs in a very short time interval. Although the WDE CA tends to decrease after some seconds, this phenomenon doesn't influence the inkjet printing process as solvent evaporation precedes the onset of droplet lateral percolation. The features of the patterns clearly depend on the initially wetted area. Indeed, WE printed stripes are characterized by the largest widths (400-500 µm) and sometimes present ill-defined profiles, while WDE and WD inks produce well resolved patterns with linewidth ranging from 80 to 120 µm. The ethanolic components plays an important role in the acceleration of the percolation of the ink into the porosity, however FESEM cross sections

Ink composition	Viscosity (cP)	Surface Tension (N/m)
water:ethanol 1:1 (WE)	2.96	31.4
water:DMSO 3:1 (WD)	1.97	54.9
water:DMSO 3:1, 90% vol+ethanol 10 % (WDE)	2.4	49.7

Table 6.1 Viscosity and surface tensions (Cahn balance method) of the inks determined at 20°C.

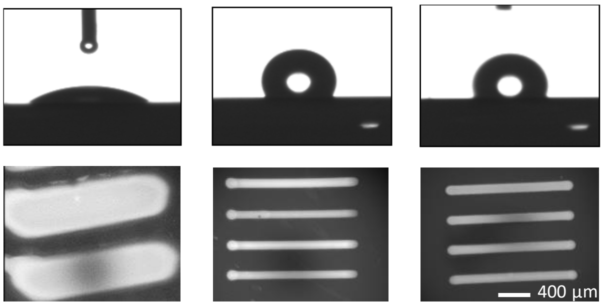

(a) (b) (c)

Figure 6.7 Images of the ink drops on pSi surface acquired with the camera of the optical contact angle set-up and corresponding inkjet printed patterns for (a) WE, (b) WD and (c) WDE inks.

of the printed samples evidence that a pore filling occurs for all the inks, because Ag NPs are synthesized throughout the thickness of the pSi layer (Figure 6.8, bottom).

On the other side, a complex morphological variation is observed for the different solvent compositions. As shown by top view FESEM images in Figure 6.8, particles size increases with a higher ethanol percentage, while the use of DMSO containing inks results in nanostructures with sharper edges. WD ink doesn't provide however a suitable particle density. This is probably due to the chemical properties of DMSO, which competes with Ag^+ cations for the oxidation of the reducing Si-H_x species on porous silicon surface.[204]
The optical (specular reflectance) and SERS responses of the nanostructures synthesized with the WE and WDE ink are analyzed in Figure 6.9. UV-Vis specular reflectance spectra collected from dense patterns of stripes display LSPRs in the 400-500 nm range. The dip is however red-shifted towards 500 nm for the WDE printed NPs, while it is centered around 400 nm for the WE ink. It should be noted that due to the shifted dip, the plasmonic resonance condition is almost fulfilled for the WDE prepared substrates irradiated at 514.5 nm. As for the NPs synthesized with the WE ink, the excitation concerns instead only with the reflectance dip tail, resulting in a halved SERS intensity of Cy5 spectrum under the same experimental conditions (Figure 6.9 (b)).

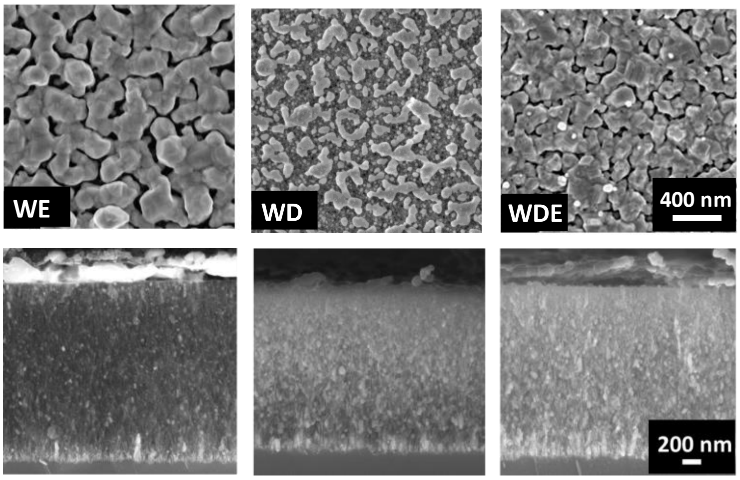

(a) (b) (c)

Figure 6.8 FESEM top view and cross section images of silver coated pSi obtained printing a $AgNO_3$ 2.5 10^{-2} M (a) water/ethanol, (b) water/DMSO and (c) water/DMSO/ethanol ink, with 6 passes and 1000 dpi step size.

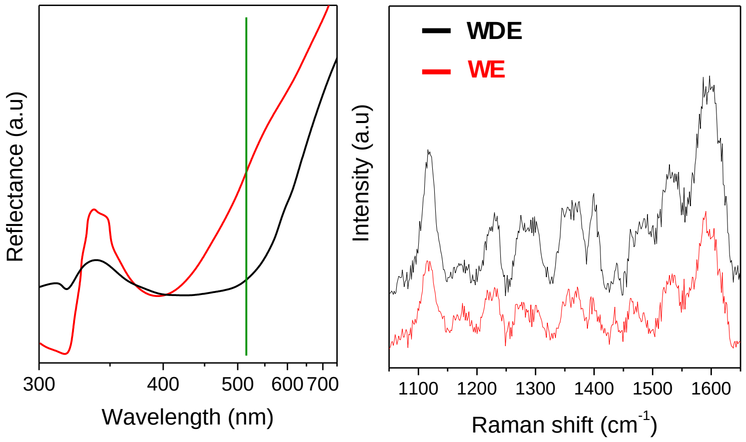

(a) (b)

Figure 6.9 (a) UV-vis specular reflectance spectra showing the LSPRs dips of the lines, printed with the WE and WDE inks, whose FESEM images are reported in figure 6.8. The dashed line indicates the excitation laser wavelength at 514.5 nm used in the Raman experiment. (b) SERS spectra of Cy5 (10^{-6} M) adsorbed on the same lines.

6.3 Raman efficiency and uniformity

The discussed study on the correlation of the synthesis conditions to the obtained morphology and SERS response points out that the best SERS intensities, in combination with good pattern qualities, can be attained employing the stripes synthesized by means of the water/ethanol/DMSO ink with 6 passes, 1000 dpi and a $AgNO_3$ concentration of 2.5 10^{-2}M. SERS efficiency and uniformity of these SERS substrates are therefore tested. Figure 6.10 reports the SERRS spectra of Rhodamine 6G spotted on the printed substrates at several concentrations. The 1647 and 1509 cm^{-1} modes, assigned to the C-C stretching of the xanthene ring, are easily detected until 10^{-12} M concentration. Moreover, also at the lower concentrations, the whole vibrational pattern of Rh6G is still present, although some changes in the intensity ratios are observed for bands in the 1200 to 1400 cm^{-1} range. Taking into account that the minimum detectable concentration of Rh6G on bare pSi is 10^{-4} M, the EARE calculated for the inkjet printed NPs is 10^8 under excitation at 514.5 nm. This result is

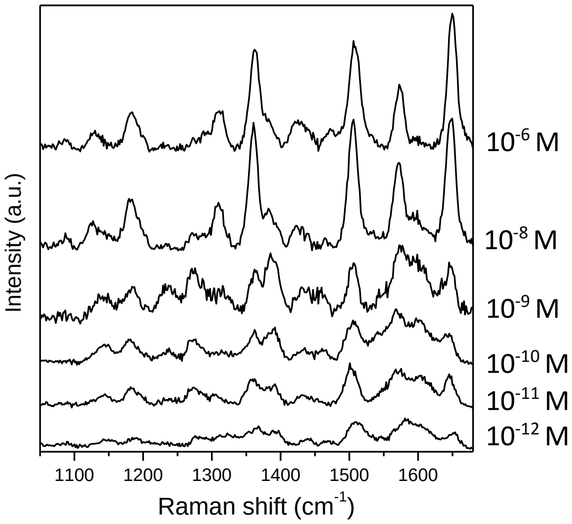

Figure 6.10 SERRS spectra of Rhodamine 6G adsorbed from solutions at different dye concentrations (10^{-12} to 10^{-6} M) on a line printed with WDE ink, $AgNO_3$ 2.5 10^{-2} M, 1000 dpi, six passes.

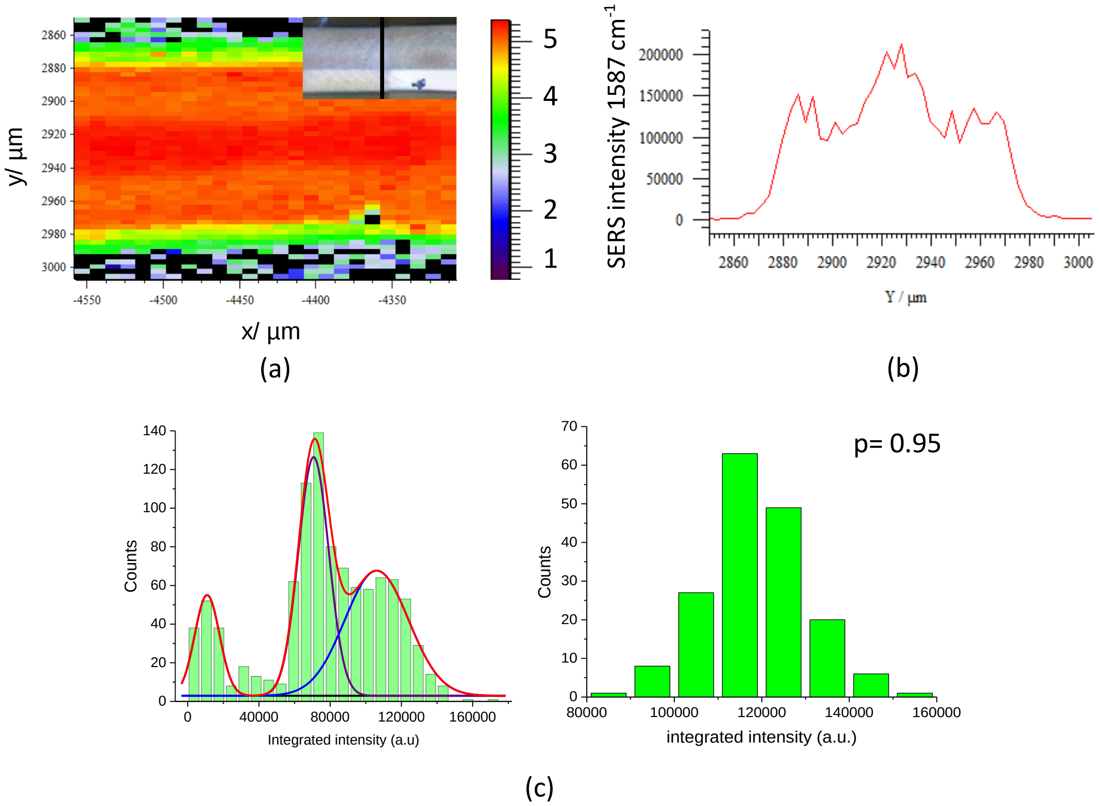

(a)

(b)

(c)

Figure 6.11 (a) False colour image of the integrated area of the 1587 cm^{-1} 4-MBA peak obtained by SERS maps acquired at 514.5 nm. The inset shows the investigated area, acquired with an optical microscope. (b) SERS intensity profile along y (extracted for x=-4430 µm). (c) Histograms representing the SERS intensities distributions for the whole stripe (left) and the central region only.

comparable to the SERS efficiency obtained for immersion plated Ag-pSi, which approached single-molecule detection in the SERRS regime.

The uniformity and reproducibility of the SERS substrates was instead assessed by incubation in 4-MBA solutions and subsequent Raman mapping. A typical false color map, covering the area shown in the optical micrograph in the inset, is depicted in Figure 6.11 (a). Excluding the outer parts, which comprise points outside of the AgNPs stripe, three intensity regions can be identified if the y profile of the printed line is concerned. As evidenced in Figure 6.11 (b), showing the SERS intensity along the marked black line, the three zones correspond to a low signal transitory region at the borders of the stripe, a medium intensity area and a high enhancing central region. On the contrary, the SERS signal is very homogeneous along the x axis. The y profile can be again rationalized if the morphological variation of the sample along this axis, which in turn depends on the wetting properties of porous silicon surface towards the WDE ink, is considered. The drop profile is in fact reflected in the particle density, with lower densities at the borders of the drop and higher particle density in the center. Figure 6.11 (c) reports the histograms of intensity distributions for the whole SERS map (left) and the central region only (right). Although the overall intensities are clearly not normally distributed, a fit with three normal distributions is possible. Each curve roughly correspond to the intensities due to the three regions. The advantage of printed stripes is that the different morphologies are spatially localized. In particular, an exceptionally high p-value of 0.95 is derived from the Shapiro-Wilk normality test for the core region. Moreover, if the measurements are taken in the central part of the stripe, a very homogenous SERS signal can be recorded with an average RSD of 11.5%. It should be noted that Raman maps were acquired with a high resolution 50x objective, which provide a lower signal averaging and therefore higher RSDs than lower numerical aperture objectives (as the one used for the immersion plated Ag-pSi). Inter-substrate variability was instead calculated for 7 different stripes, being 14.2%.

6.4 Conclusions

Arrayed SERS active stripes of silver nanoparticles have been synthesized by inkjet printing on mesoporous silicon. The optimization of the nanostructure morphology is attained by means of the variation of the ink formulation and inkjet printing parameters aiming to the synthesis of densely packed silver NPs. Due to the low polydispersion of the sizes of the nanostructures, the SERS response of printed substrates is indeed found to mainly depend on the inter-particle gap size. Huge Raman enhancements (EARE > 10^8), comparable to the ones observed for immersion plated Ag-pSi, are obtained exploiting hot spots located in between the particles. The printed plasmonic patterns also show a good uniformity and reproducibility, making the discussed fabrication technique suitable to develop active sensing platforms for multiplexed label free biodetection.

Chapter 7

Integration of Ag-coated porous silicon membranes in all-PDMS optofluidic chips

7.1 Introduction

Ink-jet printed Ag-pSi patterns are suitable open platforms for multianalyte detection. Integration of SERS substrates in microfluidics offers however additional advantages (section 2.3.2.2). Moreover, due to porous silicon intrinsic reactivity towards silver cations, an all-microfluidic process can be envisioned, in which the synthesis of the NPs, their functionalization and the detection of the analyte are performed in the chip. A method for the integration of porous silicon membranes in PDMS microfluidic systems is presented in this chapter.[205,206] Porous silicon is etched according to a pattern defined by the cover of the device and transferred to a PDMS substrate which is finally bonded to the cover. The chip takes advantage of the flexibility and transparency in the Vis-NIR range of the elastomeric matrix. The synthesis of silver NPs is attained either before or after the sealing of the device, in static or dynamic conditions. SERS characterization of the immersion plated pSi-PDMS membranes is first performed with Rh6G and 4-MBA. The in-flow growth of NPs is then monitored by UV-Vis spectroscopy on ultrathin pSi membranes, allowing the comparison of nanostructures synthesized by dipping and in flow for what concerns the optical and the SERS response.

7.2 Chip fabrication

The fabrication of a multianalyte PDMS chip containing a silver coated pSi membrane in each microfluidic chamber as SERS active elements requires first the patterning of the pSi layer. To this aim several techniques have been developed in the past, which act either at the etching level, such as the deposition of silicon nitride masks and photoresists, or by selectively removing parts of the synthesized porous layer, as in the case of dry removal soft lithography.[207] Some of these methods enable the realization of submicrometric pattern features[208,207,209,210], which are however far from the scope of a portable device for on-field measurements with fiber optic probes that doesn't

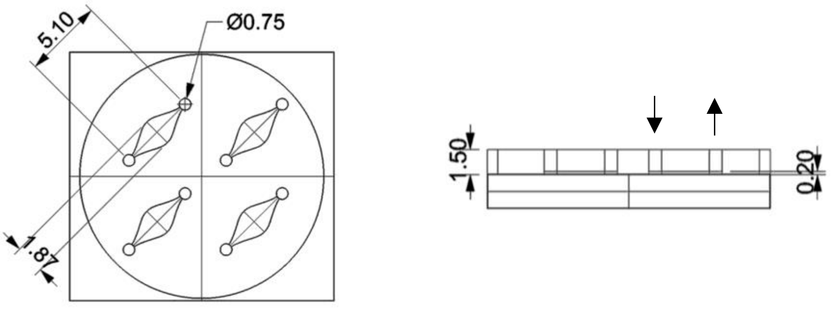

Figure 7.1 Schematic top view and cross section of the cover mold. Heights and widths of the chambers and inlet/outlet channel are expressed in millimetres.

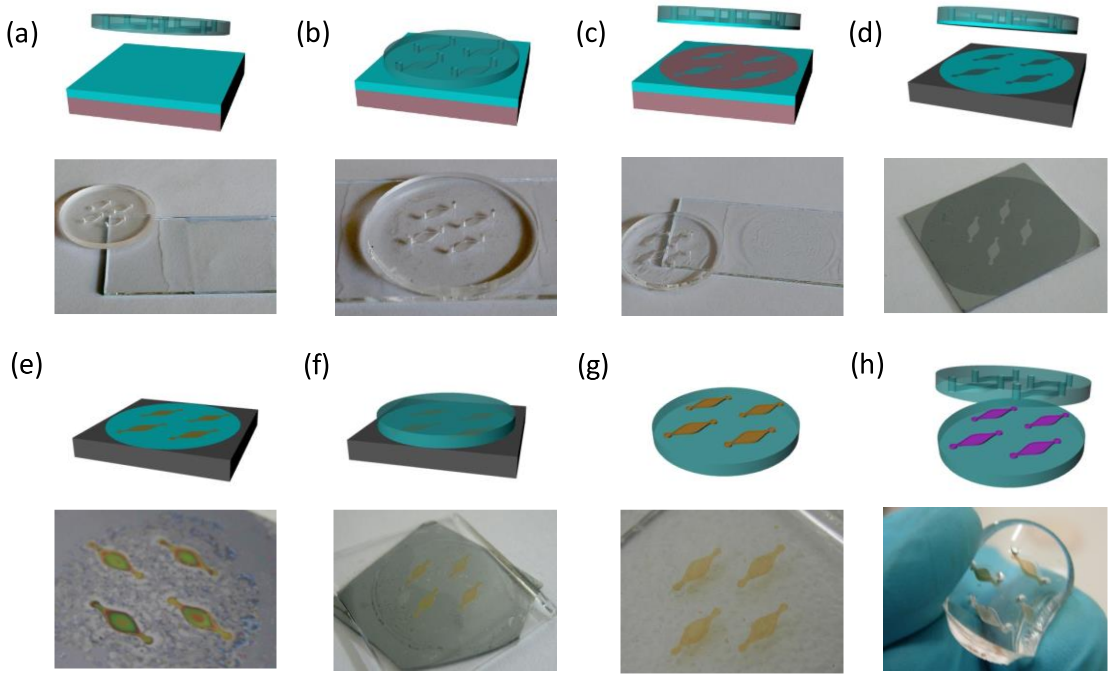

Figure 7.2 Scheme of fabrication. (a) PDMS precursors mixture spread on a smooth surface (i.e. glass slide); (b) PDMS cover placed on the mixture; (c) cover removal; (d) stamp of the cover pattern on the silicon dice; (e) patterned pSi membranes after HF anodization; (f) partially cross-linked PDMS on the pSi membranes; (g) pSi membranes transferred onto the PDMS substrate; (h) expanded vision of the silver-coated optofluidic chip. Each step is shown along with the corresponding digital photograph.

provide such resolutions; moreover, they require high cost and complex technologies. Here, an alternative method inspired by micro-contact printing is applied, providing an easy, versatile and inexpensive patterning technique.

7.2.1 Porous silicon patterning and transfer

In the presented approach, the cover of a prototypical device, hosting four drop shaped chambers, each equipped with inlet and outlet channels, is used as a stamp for the electrochemical patterning of a p^+-type silicon dice with a micrometric layer of hydrofluoric resistant PDMS. In detail, the inverse design of the cover is obtained in a PMMA mold by standard micromachining (Figure 7.1), which is then employed to cast and polymerize (at 80°C for 20 minutes) a mixture of PDMS oligomer and curing agent, previously prepared in 20:1 weight ratio and degassed. The main steps of the chip fabrication are reported in Figure 7.2. A thin layer of unpolymerized PDMS is spread onto a glass slide (Figure 7.2 (a)). The PDMS cover is then placed onto the mixture (Figure 7.2 (b)). After the cover detachment, an uncured PDMS layer is caught only in those regions, external to the chambers, that were in contact with the unpolymerized PDMS (Figure 7.2 (c)). Subsequently the PDMS film is transferred onto a silicon dice by stamping the cover on it for few seconds (Figure 7.2 (d)). The so-prepared mask needs to be cured in oven (1 h at 80°C) to allow the crosslinking of the PDMS precursors, thus stabilizing it against the successive anodization in HF, which yields the mesoporous nanostructure (Figure 7.2 (e)). The etchant is then replaced by a low concentration HF electrolyte and a second electrochemical attack is performed in order to attain the enlargement of the pores at porous silicon/silicon interface until a sufficient weakening of the connections between them. pSi still lays on the silicon support until a 1 mm thick partially cross-linked PDMS membrane (curing time reduced to 10 minutes at 80°C) is placed in contact with the etched layers to complete the detachment (Figure 7.2 (f)). Porous silicon membranes are readily immobilized onto the PDMS substrates thanks to the enhanced adhesive properties of the non-fully cured material, rich of free chains, which allow an efficient bonding. Contemporarily, the connections with silicon are finally broken, leading to an easy lift-off of the pSi-PDMS membranes from the initial substrate (Figure 7.2 (g)), which are cured for 10 minutes at 80°C to complete the crosslinking reaction of the elastomeric material and reinforce the bonding. The proposed method enables the transfer of ultrathin pSi layers (down to 300 nm or less), since the membranes are always supported throughout the process, improving the handling of the ultra-fragile material. Figure 7.2 (h) finally depicts an expanded view of the silvered Ag-pSi-PDMS (PSD) sample along with the digital photograph of the sealed chip, where the bonding has been achieved by adding a thin PDMS precursor mixture at the interface between the two components, followed by crosslinking at 60 °C for 1h.

7.2.2 Immersion plating of pSi-PDMS membranes

It is worth noting that the porous silicon surface, which is exposed to the air on the pSi-PDMS membranes, is actually the previously discussed pSi/Si interface and could therefore present different chemical and morphological properties with respect to the other side of the layer, which is usually the platform for silver NPs synthesis. A higher degree of oxidation is indeed expected, due to HF concentration gradient established in the pore thickness. Moreover, an increasing porosity along the z profile has been previously observed.[97] FESEM top view and cross sectional images, reported in Figure 7.3, were therefore acquired on the detached membranes to assess the quality of the obtained porous layer. Despite the detachment process a quite smooth surface is observed. A homogeneous pore size is also found along the thickness of the membrane, which is measured to be around 870 nm for pSi anodized at a current density of 30 mA/cm^2 for 50 s. This value also agrees with the one extracted by the simulation of the experimental specular reflectance spectrum of pSi-PDMS membranes (Figure 7.4 (a), dashed line) characterized by typical Fabry-Perot interference fringes. A thickness of 0.9 microns and a porosity of 64% are obtained by the fitting.

In order to avoid reactivity losses due to the oxidation of pSi, both during the electrochemical detachment and the PDMS curing, the pSi-PDMS membranes are pre-treated in a 10% aqueous solution of HF, that dissolves the oxidized regions, refreshing the surface with new Si-H$_x$ species. The reducing abilities of the pSi-PDMS substrates are however decreased with respect to the non-detached pSi, as it is demonstrated by the longer reaction times needed for the synthesis of silver nanostructures showing comparable particle densities and sizes. The inset of Figure 7.4 (a) shows the FESEM micrograph of the typical morphology obtained after 5 minutes of immersion plating in

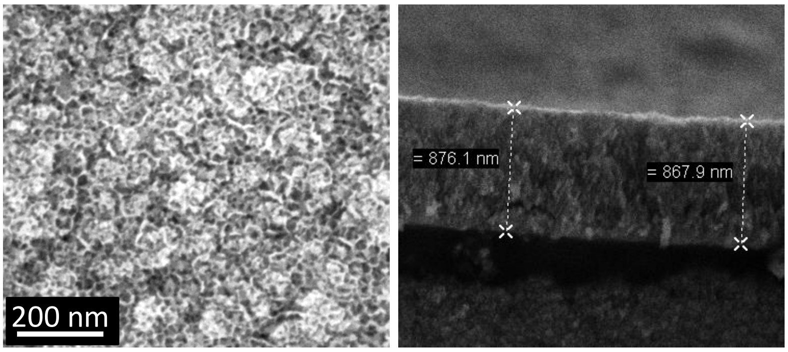

(a) (b)

Figure 7.3 FESEM micorgraphs of the porous silicon membrane. Images were acquired on the membrane directly transferred onto the conductive tape used for FESEM measurements. (a) Top view (b) Cross section.

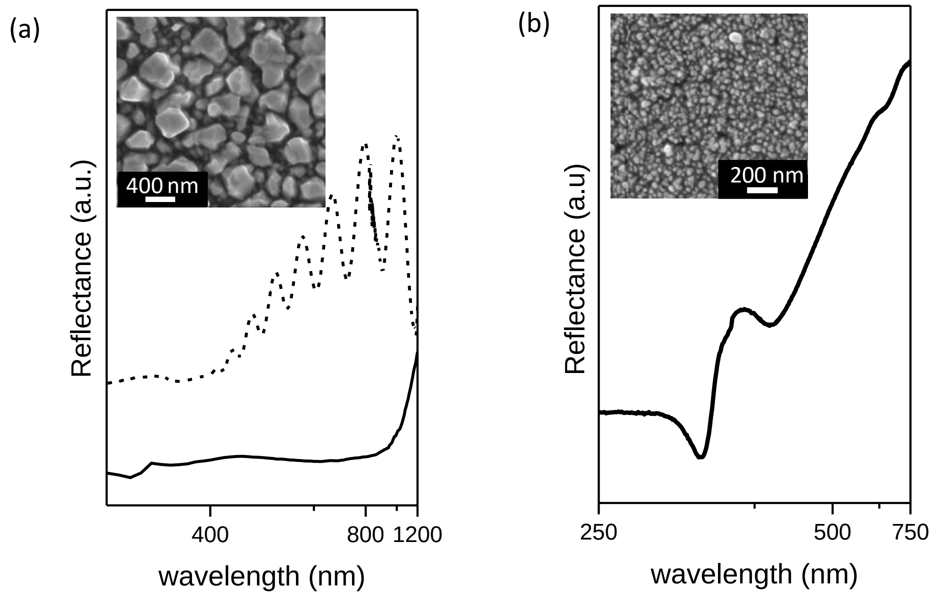

Figure 7.4 (a) Specular reflectance spectra of the silvered (solid line) and bare (dashed line) pSi-PDMS membrane. The morphology of the synthesized AgNPs is shown in the inset. (b) Specular reflectance spectra of the silvered pSi-PDMS membrane prepared by addition of very small percentages of ethanol and HF to the plating mixture. The morphology of the synthesized AgNPs is shown in the inset.

10^{-2} M aqueous $AgNO_3$. As it can be inferred by the analysis of FESEM images, silver NPs are characterized by a certain size polydispersion. Despite the irregular morphology, small interparticle gaps of few nanometers are distributed overall the pSi membrane surface, showing an average separation of 26 nm $\pm$ 48%, thus ensuring the presence of hot spots. The appearance of an extremely broad LSPR dip, covering the visible and part of the NIR wavelength range, is observed after immersion plating, which is consistent with the heterogeneous morphology.

A different set of substrates was prepared by adjusting the composition of the plating solution. Very small amounts of HF and few microliters of ethanol were added in order to recover the reactivity of pSi and to enhance the wettability of the highly hydrophobic pSi-PDMS membranes (static water CA = 150°) respectively. These changes result in a completely varied morphology (inset of Figure 7.4 (b)) characterized by quite small and densely packed silver NPs. The size distribution, showing an average diameter around 30 nm, is extremely reduced in this system. Although the UV-Vis reflectance spectrum (Figure 7.4 (b)) displays no detectable plasmonic features besides the dip at 395 nm, a huge amount of small inter-particle gaps is present, which are expected to give rise to strong SERS enhancements.

7.3 Raman efficiency and uniformity

The SERS performances of the synthesized silver nanostructures on PSD samples are tested using Rh6G and 4-MBA probe molecules. In agreement with the morphological similarity to Ag-pSi samples discussed in the previous section, the substrates characterized by bigger particle sizes allow the detection of Rh6G at 10^{-12} M concentration (Figure 7.5 (a)), giving an EARE of 10^{8}.
As shown in Figure 7.5 (b), the dense arrangement of the smaller silver NPs provides a huge concentration of the EM filed between particles which enables the ultrasensitive detection of Rh6G at concentrations as low as 10^{-14} M under excitation at 514.5 nm. The random intensities observed

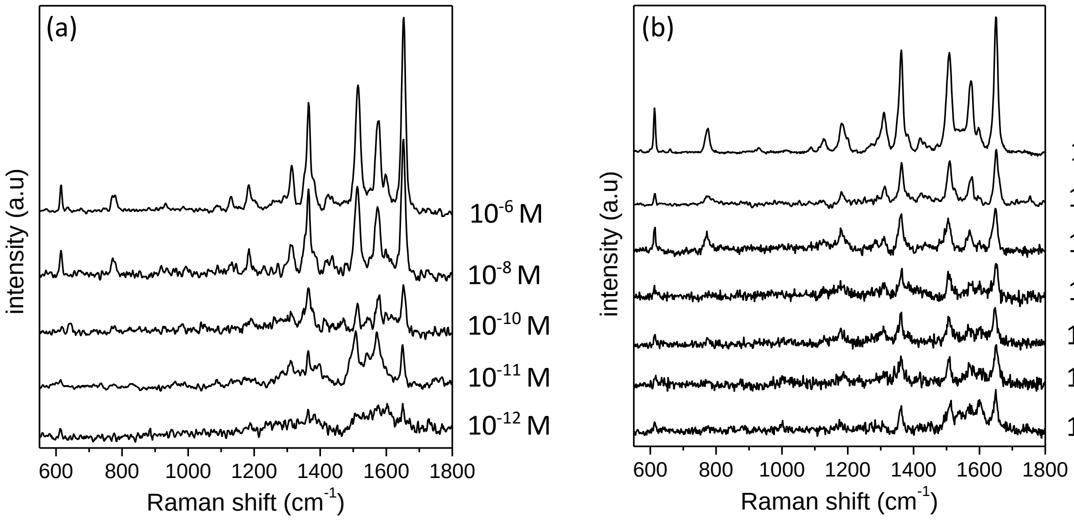

Figure 7.5 Rh6G SERRS spectra at several concentrations acquired on Ag-PSD membranes with average particle size (a) around 100 nm and (b) around 30 nm.

for the spectra collected from samples spotted with concentrations lower than 10^{-10} M are due to the combination of the hot-spot nature of the ultra-efficient SERS scatterers and the single/few molecules regime. The presented result is the best obtained for Ag-pSi samples probed under the same experimental conditions and approaches the 10^{-15} M limit of detection reported by Kosovic et al.[106]

The elaboration of SERS mapping on the two substrates after incubation in 4-MBA is reported in figure 7.6. The SERS intensities were normalized to an arbitrary value and plotted in the same range to compare the variability provided by the two substrates. From the Raman maps, a higher signal fluctuation for the big NPs is inferred. The calculated RSDs agree with the visual inspection of the images, being 39% and 15% for the big and the small NPs morphologies. The reduced particle size heterogeneity and the more regular arrangement of the second sample account for the better

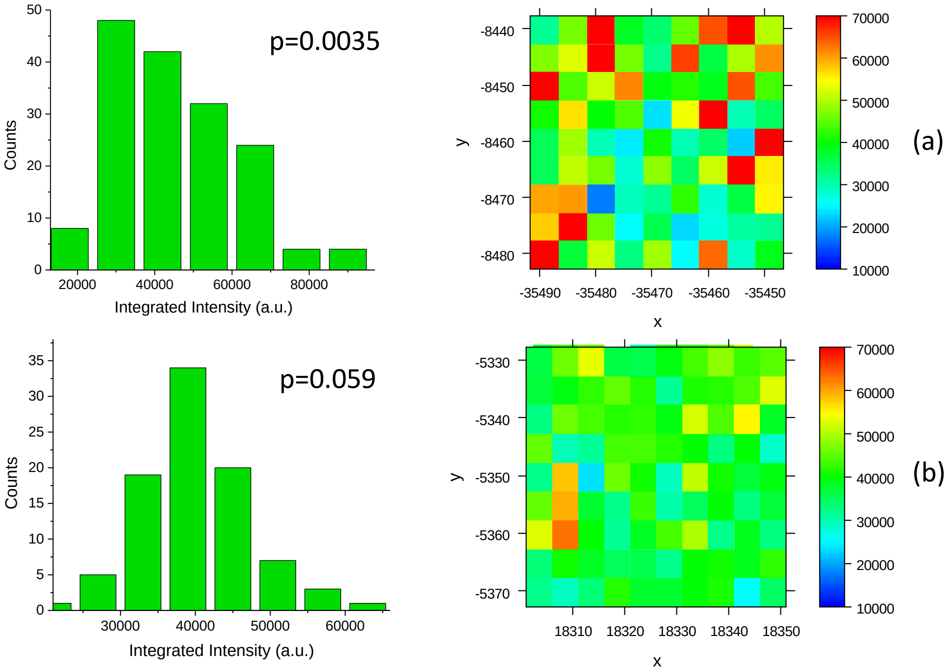

Figure 7.6 Intensity distribution histograms and false colour images of the integrated area of the 1584 cm^{-1} 4-MBA peak obtained by SERS maps acquired at 514.5 nm for (a) Ag-PSD with average particle size of 100 nm and (b) Ag-PSD with average particle size 30 nm

uniformity. Actually, normal intensity distributions are found for this sample typology, while the Shapiro-Wilk test applied to the substrates characterized by big NPs often provides p values lower than 0.05.

7.3.1 Chip calibration

Besides the study of the open Ag-PSD membranes, SERS measurements in the sealed chip were performed. Ag-pSi-PDMS samples were tested by filling the chambers of the optofluidic device with 4-MBA ethanolic solutions at increasing concentrations, starting from 10^{-9} M up to 10^{-2} M, followed by Raman mapping. Selected spectra extracted from SERS maps are reported in Figure 7.7 (a). 4-MBA vibrational fingerprint, dominated by the ν_{8a} ring mode, can be already identified with a good signal-to-noise ratio after incubation with the 10^{-8} M solution. A PSD chip sample without nanoparticles was also incubated with 4-MBA solutions as a reference, without the final washing step to avoid the removal of the non-specifically adsorbed thiol. In the absence of the plasmonic enhancement 4-MBA signal is first detected at 10^{-1} M concentration, thus resulting in an EARE of 10^{7}, which is slightly higher than the one observed for Ag-pSi SERS substrates.

Moreover, the average integrated area of the 4-MBA peak centered at 1584 cm^{-1} is plotted against the analyte concentration (Figure 7.7 (b)). A monotonic increase of the SERS intensity is observed by increasing 4-MBA concentration, which results in a trend that can be well fitted by a Langmuir isotherm with a very good R^2 value of 0.99. The Langmuir model only applies to equilibrium process which involve the chemisorption of the analyte on a fixed number of surface adsorption sites. It is reasonable that 4-MBA, whose thiol group binds to the silver atoms with a high affinity[40], shows such a behaviour. The saturation of the SERS signal at 4-MBA concentrations over 10^{-3} M is also well explained by the saturation of adsorption sites due to the formation of a monolayer of molecules on the silver NPs surface. Actually, the possibility to reliably fit SERS intensity data implies that the chip could be calibrated and therefore employed in quantitative analysis. The use of small NPs PSD membranes is under study, in order to further reduce the intra-substrate variability.

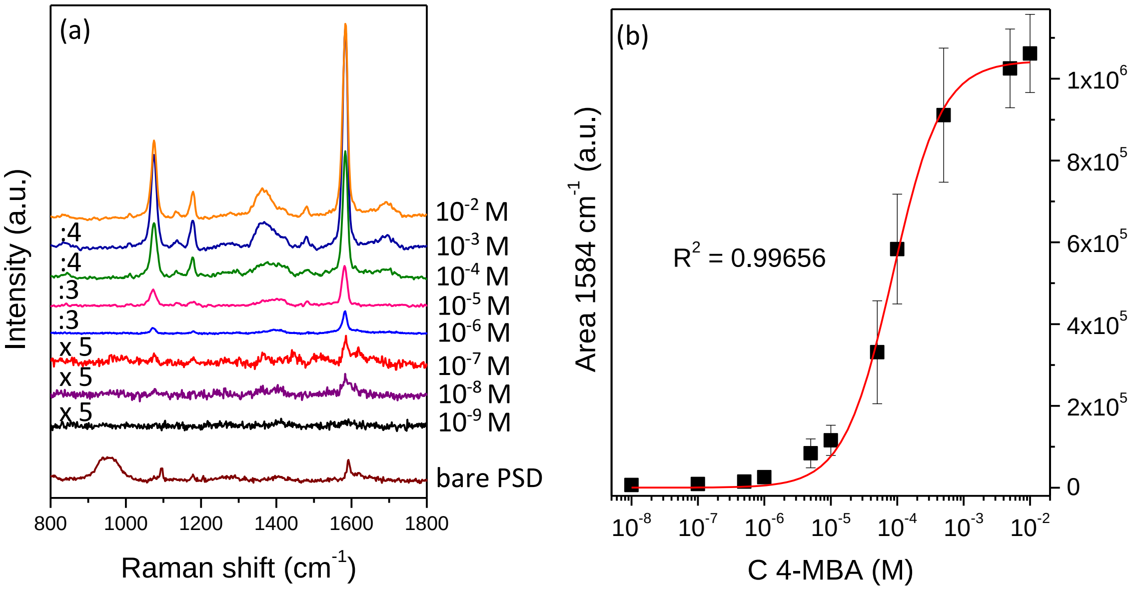

Figure 7.7 (a) 4-MBA spectra acquired in the chip at several concentrations. The spectrum of 10^{-1} M 4-MBA on bare pSi-PDMS is reported as comparison (the intense feature around 950 cm^{-1} is the second order c-Si peak). Spectra were rescaled by the factors indicated on the left side of the plot. (b) Langmuir fit of the integrated area data extracted by SERS mapping *vs.* 4-MBA concentration.

7.4 Towards an all-microfluidic process

So far, silver NPs have been synthesized before the cover bonding. However, the reducing properties of the porous silicon surface can be exploited to grow the nanostructures directly in the optofluidic chip (in-flow synthesis). This is attractive as it allows the development of entirely microfluidic processes, including both the preparation of the SERS substrate and the detection steps. Moreover, the synthesis can take advantage of the intrinsic improvements related to a microfluidic reaction occurring under dynamic conditions in a controlled environment. Finally, the real-time monitoring of the growth of the NPs is feasible through UV-Vis spectroscopy, thanks to the transparency of the PDMS scaffold. In the following sections, the synthesis of silver NPs under flow conditions in PSD chips is studied and compared to static immersion plating.

7.4.1 Dynamic synthesis of silver nanoparticles and in situ monitoring

PSD membranes were prepared following the fabrication scheme presented for the multi chamber chip (section 7.2.1), unless that the patterning step was not necessary. Single membrane chips were indeed employed, due to the millimetric-sized light spot of the UV-Vis spectrophotometer. Ultrathin porous silicon membranes were etched in order to enhance the transparency of the final device. To this end, the anodization time was reduced to 6 s, producing 300 nm thick pSi layers. The set-up used for the in-flow synthesis is illustrated in Figure 7.8. A motorized syringe with tunable flow rate is connected to the microfluidic chip hosting the porous silicon membrane and drives the injection of the silver nitrate solution into the reaction chamber from a capillary immersed in a reservoir beaker. The chip is mounted into the sample compartment of a UV–Vis spectrophotometer (Perkin-Elmer) leaving the drop-shaped chamber exposed to the light beam.

The UV-Vis transmission spectrum of the PSD chip is shown in Figure 7.9 (a) as a reference. The observed spectral features are the superposition of the optical response of the PDMS chamber and of the pSi membranes, which are responsible for a strong absorption below 400 nm. A slight modulation over 450 nm is also related to the Fabry-Perot interference fringes of the porous layer, that are however very broad due to the reduced thickness. As the silver nitrate solution is injected in the chamber (Figure 7.9 (b)), a sudden increase of the transmittance occurs. This phenomenon is well-known, being explained by the reduced light scattering due to the flattening of the roughness of the PDMS walls. Besides the enhanced transmission, the appearance of a weak dip around 400

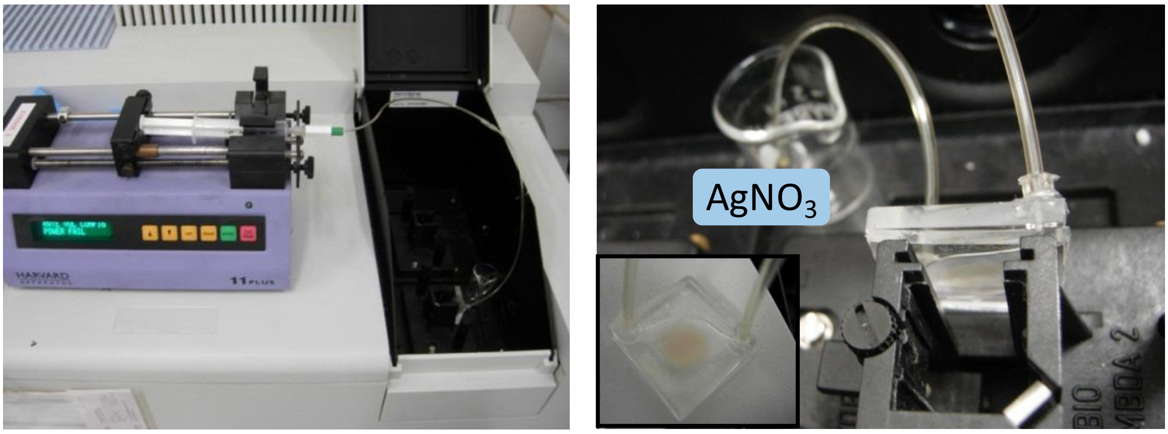

(a) (b)

Figure 7.8 (a) Set-up for in-situ monitoring of the synthesis of AgNPs on PSD samples. (b) Enlarged view of the spectrophotometer sample compartment. The inset shows the microfluidic chip hosting a 300 nm thick pSi membrane with the inlet and outlet channels connected to capillaries.

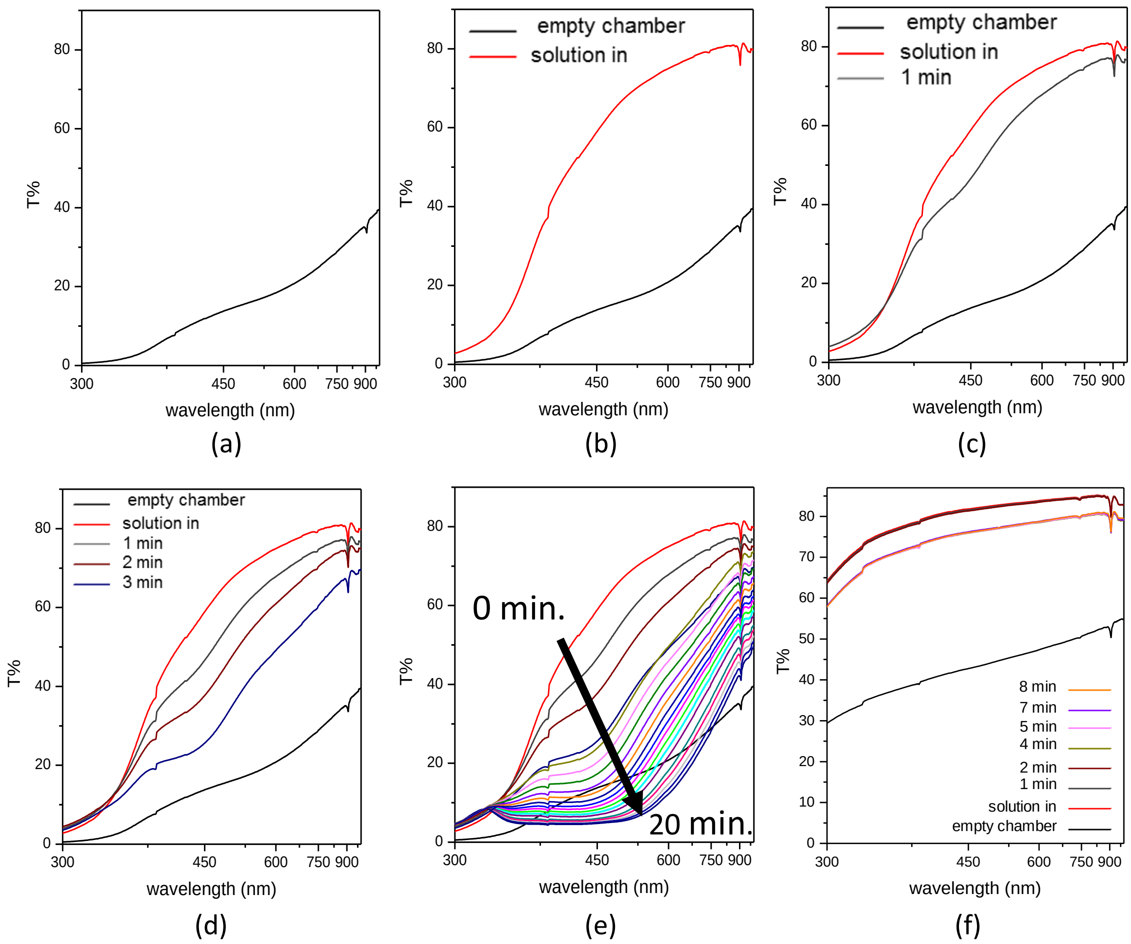

(a) (b) (c)

(d) (e) (f)

Figure 7.9 Real time UV-Vis transmission spectra acquired during the synthesis of AgNPs on the PSD chip. (a) bare chip; (b) after filling with the $AgNO_3$ solution; (c) reaction time =1 min; (d) reaction time =3 min (e) reaction time =20 min. (f) Real time UV-Vis transmission spectra acquired during the exposure of a chip without the pSi membrane to a silver nitrate flowing solution.

nm can be noticed, which is more evident after 1 minute of reaction (Figure 7.9 (c)). Spectra are then recorded continuously to monitor any change in the transmittance of the PSD membranes, with a delay of about one minute between each other, due to the acquisition time of the instrument. Figure 7.9 (d) collects the spectra obtained after 3 minutes after the first injection. The initial slight dip has clearly developed, witnessing the synthesis of silver NPs giving rise to LSPRs. Moreover, the plasmonic resonance red shifts at longer times, both due to the bigger size and the higher density of the growing NPs. After 20 minutes, a saturation condition is reached. The spectrum is characterized by an extremely broad dip, which probably convolutes different plasmonic contributions. As comparison Figure 7.9 (f) reports the spectra of a PDMS chip subjected to the same silver nitrate flow. In the absence of the pSi membranes no variations in the transmission profile are detected. The weak lowering of the transmittance after 5 minutes is due to the refilling of the chamber once the solution from the syringe is recovered and re-injected in the chip.

In order to understand the differences between silver NPs synthesis under dynamic and static conditions, an open PSD membrane is attached to the wall of a plastic cuvette and then covered with a 10^{-2} M silver nitrate solution. UV-Vis transmission spectra acquired during the immersion plating are compared in Figure 7.10 with the ones obtained by the fluidic process. It can be noticed that the development of the plasmonic dip, which in this case it is centered between 400-450 nm,

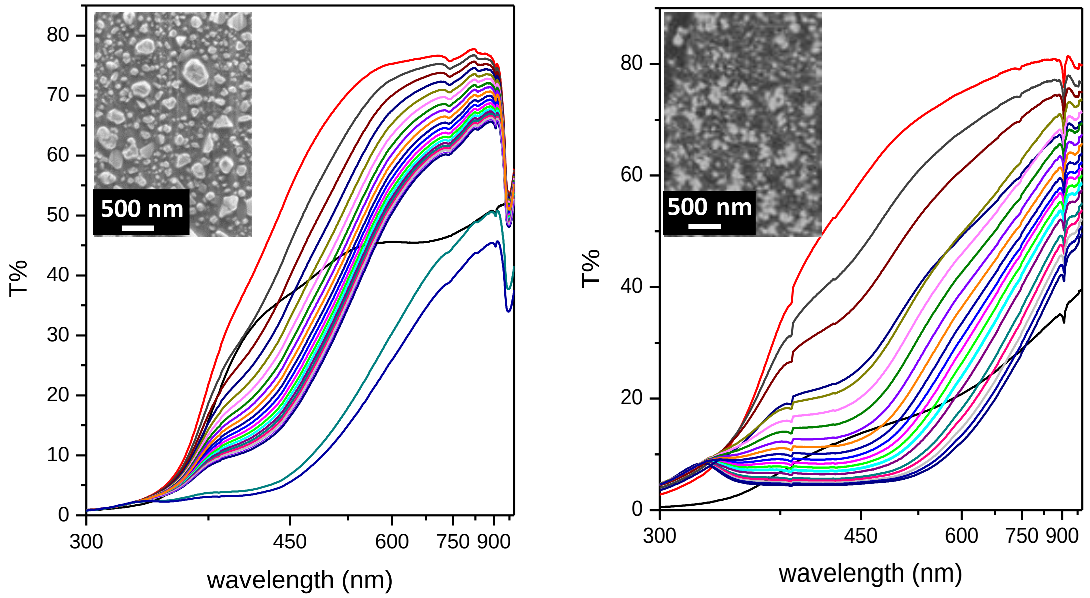

(a) (b)

Figure 7.10 Real time UV-Vis transmission spectra acquired during the synthesis of AgNPs (a) by immersion plating and (b) in the microfluidic chip (reaction time from 0 to 20 minutes) and corresponding FESEM micrographs of the AgNPs after quenching of the reaction at 20 minutes. The dark cyan and navy curves in plot (a) were recorded after 80 and 110 minutes.

is quite slower for the static synthesis. Indeed, the saturation is still not attained after more than 1 hour and 30 minutes. A slower particle growth rate is therefore foreseen. The inspection of FESEM images acquired on the two Ag-PSD samples helps the interpretation of the spectrophotometric analysis. Despite their bad quality due the thick PDMS insulator layer, causing a marked charge-up effect, a dense arrangement of particles characterized by sizes in the 50-100 nm range accounts for the observed large width of the plasmonic dip obtained in flow. On the contrary, the immersion plated sample is characterized by isolated big NPs with diameters over 100 nm, which determine its optical response. The presence of smaller particles (d < 20 nm) cannot be excluded, but their size is below the instrument resolution under the harsh working conditions. In summary, the synthesis of NPs in flow leads to a more homogeneous particle distribution, probably due to the more

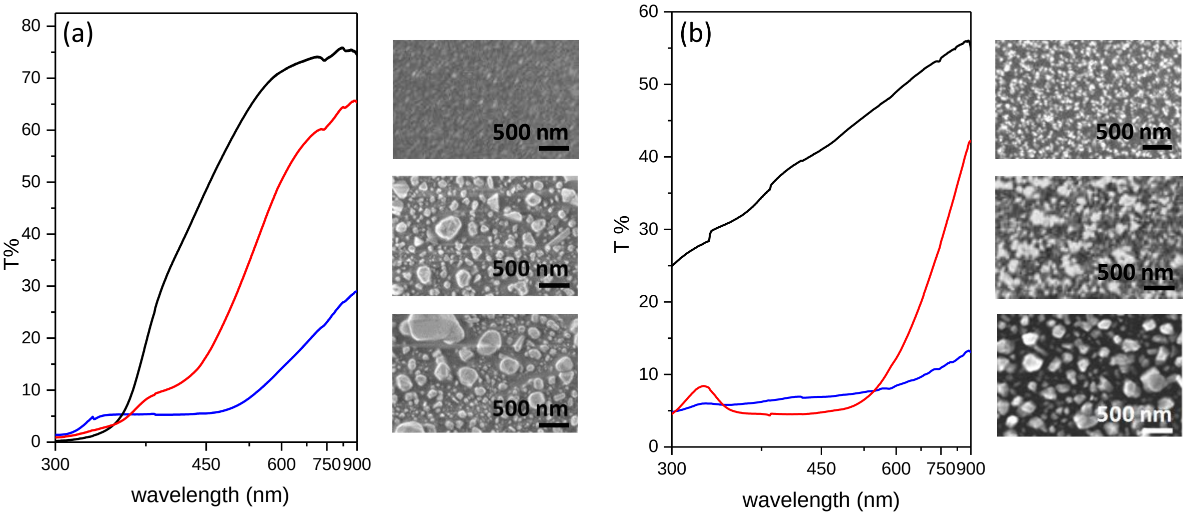

Figure 7.11 UV-Vis transmission spectra of Ag-PSD samples synthesized at 10^{-3} M, 10^{-2} M and 10^{-1} $AgNO_3$ concentration (a) by immersion plating and (b) in the microfluidic chip (reaction time = 20 minutes) and corresponding FESEM images.

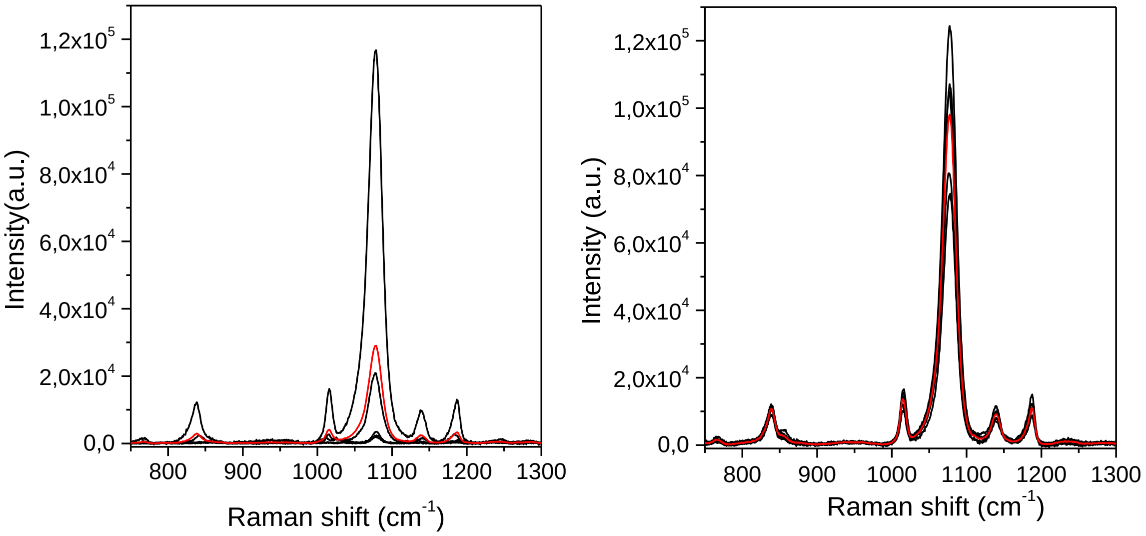

(a) (b)

Figure 7.12 SERS spectra of 4-MBA measured under the same experimental conditions on Ag-PSD membranes prepared (a) by immersion plating and (b) in the microfluidic chip. The red spectrum represents the average.

efficient supply of silver cations to the pSi surface, which allows a balanced growth of all the nucleation centers and avoids the formation of local concentration gradients caused by the even slight changes in reactivity of different sample regions.[211] Figure 7.11 confirms this trend for three different investigated $AgNO_3$ concentrations. Broader and more pronounced LSPR dips, associated to higher particle densities, are always observed for the dynamic synthesis. In both the processes an increase of silver nitrate concentration results in bigger particle sizes. It is worth to underline that the presented morphologies are not optimized. However, a clear improvement of the uniformity and density of the NPs distribution is observed with the aid of the microfluidic process at room temperature, in absence of the HF pre-treatment and using a non-optimal porous silicon thickness (very thin membranes are usually characterized by a higher amount of defects).

The observed morphological features are reflected in the SERS response, as it is demonstrated by preliminary SERS measurements performed after the incubation of the synthesized samples with 4-MBA. Figure 7.12 depicts the spectra acquired in 5 different points along the Ag-PSD surface of the substrates prepared in dynamic and static conditions. The average spectrum drawn in red highlights a major SERS intensity for microfluidic synthesized particles, combined with a moderate signal fluctuation. On the contrary, immersion plated substrates show spectra whose intensities span over two orders of magnitude.

7.5 Conclusions

This chapter has presented a fabrication procedure for SERS active microfluidic chips, characterized by a multi-chamber configuration. Such devices show excellent and good enhancement efficiencies under SERRS and electronic off-resonant SERS excitation, respectively. The calibration of the SERS response of the chip is possible through a Langmuir fit of the spectral intensity data of 4-MBA probe molecule. Moreover, a single microfluidic chamber was used to demonstrate the benefits of silver NPs synthesis in dynamic conditions. The process was followed by UV-Vis spectroscopy and paves the way to an entirely microfluidic assay. The chip, in the multichamber form, is a promising portable and isolated platform for multianalyte point of care SERS analysis.

Chapter 8

Label free miRNA detection

8.1 Introduction

This last chapter presents the optimization of a Surface Enhanced Raman Scattering based bioassay for the detection of microRNAs tumor biomarkers, applied to the developed silver-coated porous silicon nanostructures. miRNA222 was chosen as a model miRNA because of its implication in numerous neoplastic diseases, such as renal, prostatic and pancreatic cancer.[212] First of all, the stability of the SERS substrates in physiological conditions is checked as an essential pre-requisite. Subsequently, to specifically capture the miRNA target, the immobilization of a DNA probe on the AgNPs, is studied. A labelled miRNA-cy5 is employed for the optimization steps, while the final bioassay is performed in a label-free configuration, exploiting the multi-chamber Ag-PSD chip. The results are confirmed by a well-established technique, the ELISA, Enzyme Linked Immuno-Sorbent Assay, which is here applied to the metal-dielectric substrates.

8.2 Biocompatibility of the SERS substrates

Most of the tests on the performances of SERS substrates are performed in aqueous and ethanolic solutions. However, in a bioassay, parameters such as pH and ionic strength have to be strictly controlled to improve the efficiency of each immobilization and binding step. Buffered solutions are therefore employed to incubate the biomolecules. Moreover, if the detection of circulating miRNAs is concerned, samples may be directly incubated in biofluids, such as serum or blood, which are known for their high salt content. The compatibility of a SERS substrate with these particular environments has therefore to be assessed before starting any optimization on the real bioassay. In the following section, silver nanostructures on porous silicon are studied in terms of their SERS efficiency and morphology (determined by FESEM) both before and after overnight incubation in the buffers needed in the subsequent biofunctionalization protocol.

8.2.1 SERS substrates stability in buffer solutions

The set of buffers was selected on the base of the previous optimization of an ELISA protocol for miRNA detection in maleimide-activated plates (unpublished results). Ag-pSi, printed stripes and Ag-PSD open membranes were subjected to the overnight incubation. The results are reported in the followings for each substrate.

8.2.1.1 Ag-pSi

FESEM micrographs of Ag-pSi SERS substrates before (left) and after (right) overnight incubation in the TE-NaCl buffered solutions are shown in Figure 8.1 at low and medium magnification. The silver NPs layer is clearly damaged by the long contact with the solution. Big aggregates of NPs, as well as empty regions are seen in the 10kx image as a consequence of the detachment of the NPs from the pSi substrate. The higher magnification evidences instead the origin of these phenomena: marked failures in the porous layers are observed in the areas without NPs, besides the enlargement of the pores. Silver NPs loss, which for some samples results in a naked eye-detectable exfoliation of the

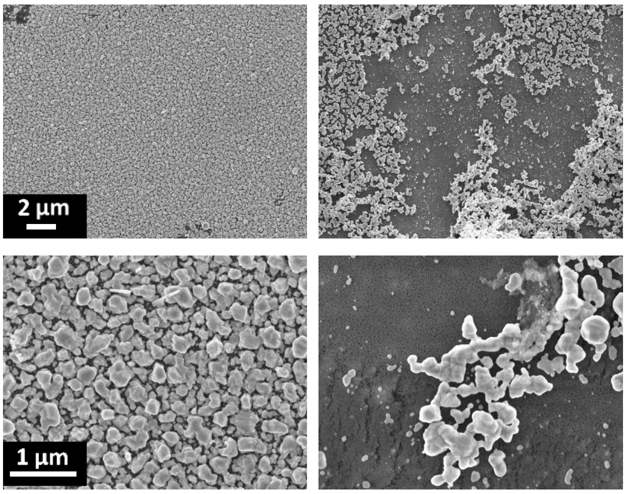

(a) (b)

Figure 8.1 Stability of Ag-pSi samples in TE-NaCl. FESEM micrographs of Ag-pSi (a) before and (b) after the overnight incubation in the buffer at 10kx (top) and 50kx (bottom) magnification.

silver coating, is thus related to the damage of the pSi support. Indeed, pSi suffers of mechanical strains produced during the electrochemical etching and the subsequent silver nanoparticles synthesis, due to the extended dense particle coverage and surface oxidation. It is also known that porous silicon can be chemically attacked by the buffers containing Tris or other amines.[213]

As for the SERS efficiency test, the lowest detectable concentration of Rh6G before and after incubation does not change. This finding is explained by the presence of the agglomerated NPs, which can locally provide hot-spots. However, the signal over a large area is expected to be non-homogenous due to the wide regions depleted of NPs.

8.2.1.2 Ink-jet printed Ag-pSi

Printed NPs show a higher resistance to the buffer solutions. From the FESEM images in Figure 8.2 it can be inferred that the printed stripes are totally preserved after the incubation. Furthermore,

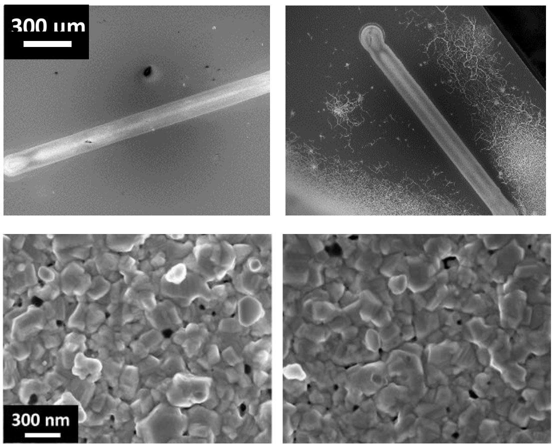

(a) (b)

Figure 8.2 Stability of printed Ag-pSi in TE-NaCl. FESEM micrographs of the silver NPs stripes (a) before and (b) after the overnight incubation in the buffer at 200x (top) and 100 kx (bottom) magnification.

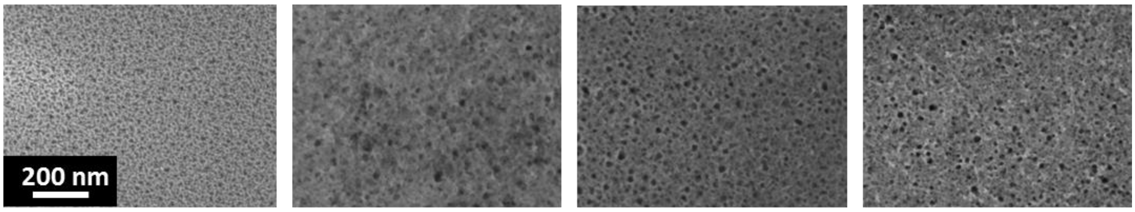

Figure 8.3 FESEM images of the exposed pSi: (a) as prepared; incubated in (b) SSC4x-SDS, (c) TE-NaCl, (d) TE-tween

no changes in the morphology are observed. The large non-coated area of these samples allows a better understanding of porous silicon behaviour during buffer incubation. Figure 8.3 highlights the enlargement of the porosity after contact with TE, SSC 4x+SDS and TE-Tween buffers. However, cracks are not observed for the surfactant containing solution, pointing out that these are probably formed during the drying process, because of the high surface tensions of surfactant-free buffers. Moreover, cracks only appear in the porous silicon regions far from the silver NPs line (Figure 8.2 (b), top), indicating that the printing process is involved in the stabilization of the metal-dielectric nanostructures. Indeed, the presence of a certain amount of DMSO in the ink can play this role. Such molecule is a mild oxidizing agent for porous silicon, which attacks preferentially the most strained regions, thus reducing the mechanical instability of the structures.[204] As a consequence , the printed Ag-pSi samples were subjected to a pre-treatment in DMSO:ethanol 1:1 mixtures before their use in the bioassay.

Finally, after the overnight incubation, Rh6G is still detectable at 10^{-12} M concentration, meaning that also the SERS efficiency is not affected by this long treatment in the buffer solutions.

8.2.1.3 Ag-pSi-PDMS membranes

Ag-PSD membranes of the small-NPs type are employed due to their superior SERS efficiency and uniformity. The nanostructures are particularly stable in the buffer solutions, as evidenced by the FESEM micrographs in Figure 8.4. An enhanced mechanical stability is probably provided by the flexible PDMS substrate. Rh6G ultrasensitive detection at 10^{-14} M concentration is also preserved after incubation.

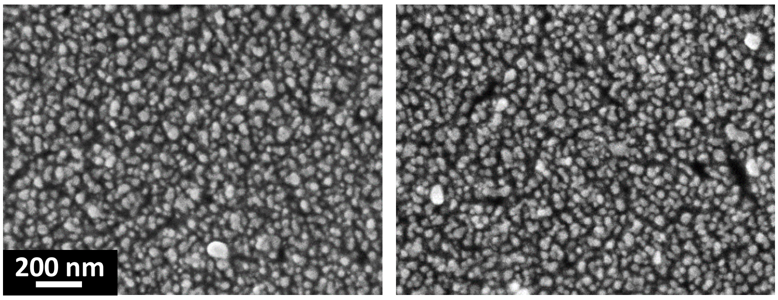

(a) (b)

Figure 8.4 Stability of Ag-PSD membranes in TE-NaCl. FESEM micrographs of the silver NPs (a) before and (b) after overnight incubation.

8.3 Functionalization protocol on printed and PDMS-supported Ag-pSi

The functionalization protocol for miRNA222 detection is depicted in Figure 8.5. Each step will be addressed in the following sections. The core of the bioassay relies on miRNA222 hybridization with a complementary DNA sequence immobilized on the silver NPs. To this end, the SERS substrate is functionalized with customized oligo-probes, modified at the 5' end with a C6 alkyl-thiol group (Figure 8.5 (b)). miRNAs are thus detected on the silvered surface through the highly specific interaction with the probe. (Figure 8.5 (c)). However, one of the main issues in a bioassay is the nonspecific binding, which occurs when the targets are retained at the surface through interactions which do not involve the recognition event with the probe. For example, oligonucleotides may bind to the silver NPs via electrostatic interactions or by means of the donor groups of the nucleobases.[137] Moreover, their easy adsorption onto the porous silicon matrix[214] is particularly problematic. An appropriate surface blocking (Figure 8.5 (a)), combined to a careful choice of the buffers is necessary. The reduction of the nonspecific binding will be discussed in the next section.

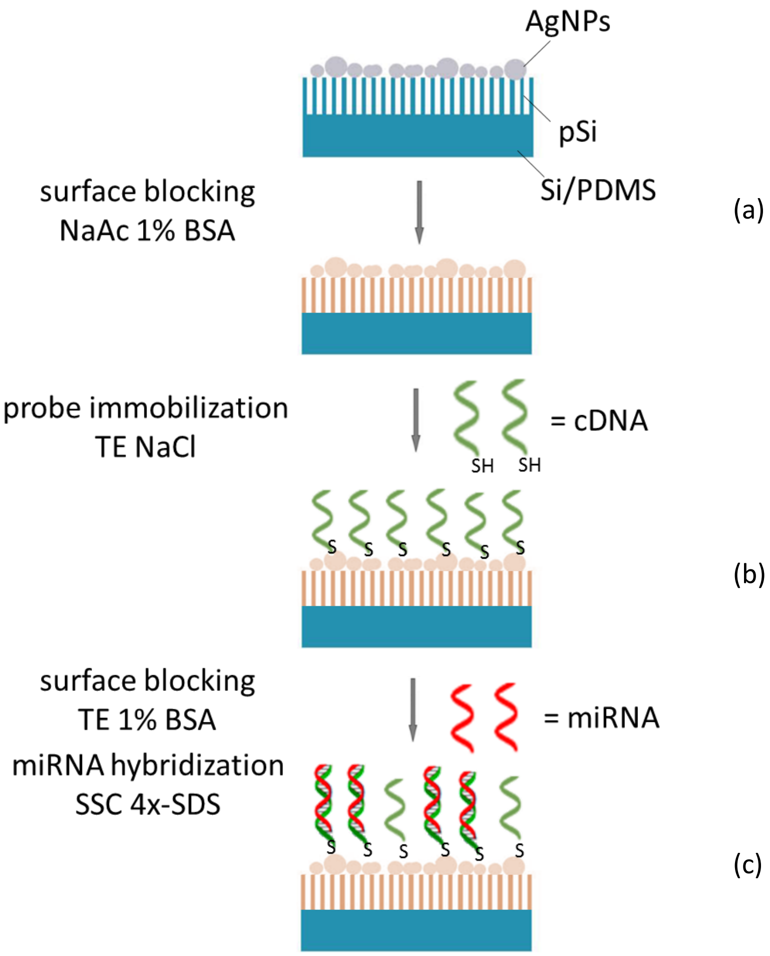

Figure 8.5 Scheme of the functionalization protocol. (a) Ag-pSi substrates, either supported on Si (printed samples) or on PDMS membranes (Ag-PSD) are passivated with BSA. (b) Overnight immobilization of the complementary DNA probe in TE NaCl buffer. (c) Hybridization with the target miRNA by one-hour incubation in SSC 4x-SDS.

8.3.1 Nonspecific signal removal

The presence of nonspecific interactions has always to be considered in a bioassay. For this reason, a "negative control" substrate, where the miRNA is incubated in absence of the oligo-probe should be part of the set of the analysed samples. Moreover, the minimization of the non-specific binding has to be considered at the bioassay optimization level.

As far as the buffers are concerned, TE, TE-tween, SSC 1x and SSC 4x+SDS solutions were tested. The nonspecific binding was evaluated by incubation of the SERS substrates with a cyanine-5 labelled miRNA222, dissolved in the different buffers. After washings in the same buffered solutions SERS measurements were performed. The comparison of the spectra with the vibrational fingerprint of miRNA-cy5 spotted on the SERS substrate surface (Figure 8.6) clearly points out that in absence of a surface passivation a certain degree of nonspecific binding exists. Although after washings the SERS signal intensity is reduced with respect to the spotted oligonucleotide, typical peaks, mainly ascribed to the Cy-5 SERS label, are detected. It should be noted that the addition of surfactants improves the nonspecific binding removal. Buffers containing tween 20 or SDS are therefore employed for the washings steps. On the other hand, the use of surfactants in the immobilization/hybridization steps is detrimental for the specific binding and should be avoided. Besides the choice of the buffers, a surface passivation pre-treatment is required. Bovine Serum Albumin (BSA) is a 66.4 kDa molecular weight protein, which is widely exploited as blocking agent in immunoassays.[215] Moreover, its adsorption on porous silicon surface has been studied in the past.[216,217] Based on these previous literature works, the protein is selected for the passivation of the metal-dielectric nanostructures. In order to maximize the adsorption of the BSA molecules on the pSi surface, the pretreatment was performed in NaAc at pH 4.0, a pH value just below the isoelectric point of the protein. Figure 8.7 shows the effect of the introduction of a passivation step (1 h) before the overnight incubation with the miRNA-cy5 solution in TE-NaCl. The results, illustrated both for the printed samples and the Ag-PSD membranes, show that a huge nonspecific signal is obtained from the second substrate type without any pretreatment. The increased intensity is however likely to be due to the higher SERS efficiency of Ag-PSD samples which is roughly estimated to be around 2 orders of magnitude greater than the one of the printed NPs, if the EARE of the two nanostructures is compared. On the contrary, after blocking with BSA, the

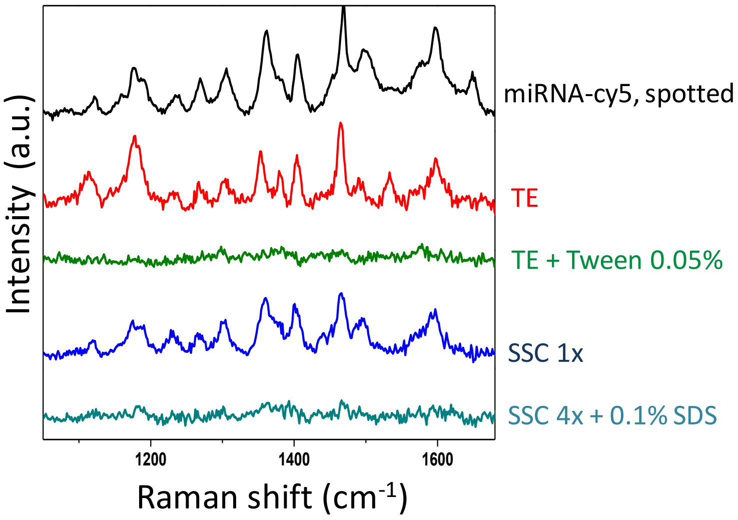

Figure 8.6 SERS spectra of printed Ag-pSi after incubation with miRNA-cy5 in TE, TE-t, SSC 1x and SSC4x+ SDS, followed by washings in the same buffers. The spectrum of the spotted miRNA-cy5 is reported on the top as a reference.

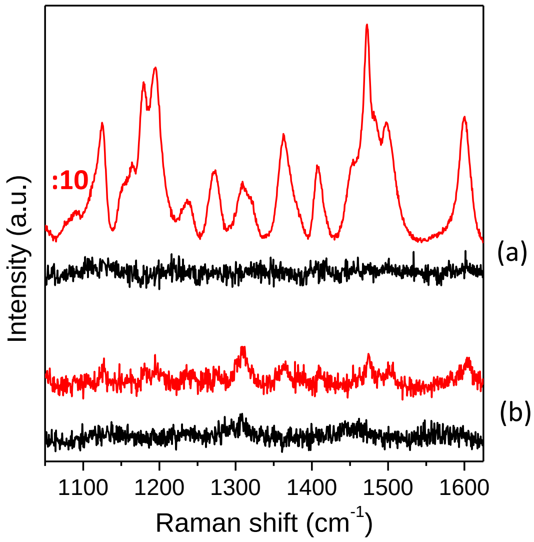

Figure 8.7 SERS spectra of (a) Ag-PSD membranes and (b) printed Ag-pSi incubated with miRNA-cy5 in TE-NaCl, followed by washings in the same buffer, in presence of BSA surface passivation (bottom black spectrum) and without any blocking pretreatment (top red spectrum). The spectra were rescaled by the factors indicated on the left side of the plot.

spectra are characterized by flat features, indicating that the protein successfully passivates pSi and AgNPs surfaces, avoiding the nonspecific interaction of the miRNA-cy5 strand. The presence of a layer of BSA molecules is also evidenced by the increased wettability of the pretreated substrates with respect to the non-pretreated ones.

8.3.2 DNA probe immobilization

A reproducible probe immobilization is essential for the subsequent capture of the target. Furthermore, the probe surface density is really important for an optimal miRNA hybridization: a low surface coverage yields a low hybridization signal, but an impaired hybridization can be also obtained with a too high coverage, due to steric hindrance.[128] As revealed by previous reports, in order to maximize the amount of well-packed probe on a surface, a certain amount of salt is required to shield the negative charges carried by the phosphate of the backbone.[218,219] Indeed, as shown by ELISA tests, the addition of NaCl to the TE buffer clearly improves the amount of immobilized probe, with a saturation around 1 M salt concentration. Moreover, as oligos linkage to the NPs surface is based on the semi-covalent sulphur-silver bond, alkylthiol capped DNA sequences were reduced with DTT to ensure the presence of free and reactive –SH. The separation of the freshly reduced oligos from the DTT molecules is performed in size exclusion microcolumns. These microcolumns contain a colloidal solution of microparticles that are packed by means of a centrifuge to create the column bed. Finally, the sample is applied to perform the separation. This step, the so-called desalting, is found to be critical for the success of the bioassay and will be discussed in the followings.

8.3.2.1 Optimization of the desalting process

Although the reduction of the thiol groups is known to increase the immobilization yield, the subsequent desalting process is not trivial. The understanding of this separation step was possible through the analysis of the SERS spectra of the collected fractions and their comparison with UV absorption spectra. Three fractions are collected at the end of the column. According to the size exclusion principle, the bigger oligonucleotides should be retained in the column for a shorter time with respect to DTT, which is a small C 4 dimercapto-diol. SERS spectra of the collected fractions

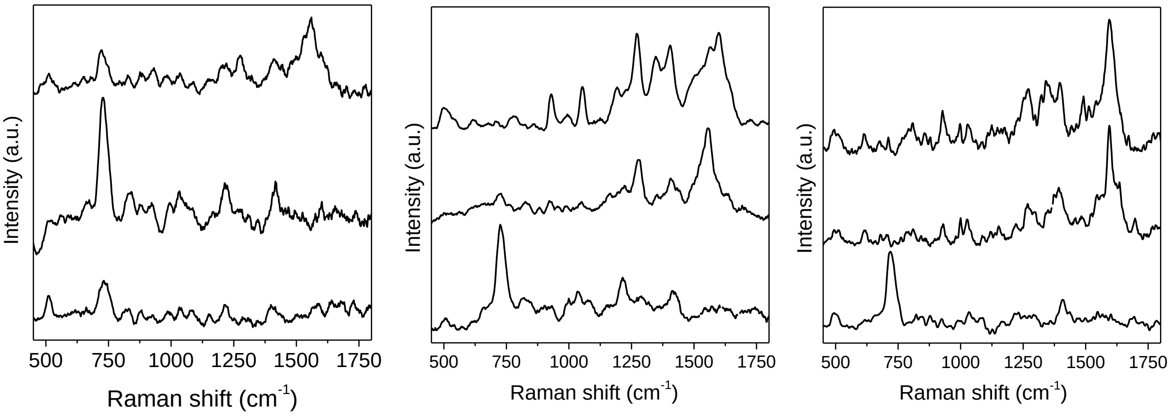

(a) (b) (c)

Figure 8.8 SERS spectra of the three fractions (1- top, 2- center, 3 - bottom) obtained by size exclusion separation of the DTT-DNA mixture, spotted onto Ag-PSD membranes under different conditions: (a) non well-packed column (b) excessive sample volume (c) optimized separation with pre-washings of the column, drop-by-drop sample dispensing and 50 µl volume

are reported in Figure 8.8, for different elution optimization levels. It can be noticed, that the separation output can be very different, depending on the obtained column packing, sample injection rate and employed volumes. The spectrum of the third fraction is the most reproducible one and can be easily assigned to DTT molecules, being characterized by an intense C-S stretching band at 720 cm^{-1} and weaker peaks related to C-C stretching (1008 cm^{-1} and 1080 cm^{-1}) and to C-H deformations (1218 and 1410 cm^{-1}) at typical Raman shifts of aliphatic thiols.[220,221] If column preparation is not optimized, DTT fingerprint dominates the spectrum both of the third and second fractions (Figure 8.8 (a)). Moreover, it can be already present in the first one, besides few additional peaks, detected at 1275 and 1557 cm^{-1}. These bands can be associated to the DNA probe immobilized in a vertical conformation with respect to silver surface, as better discussed in the next section. It should be noted that UV quantitation of the DNA content of fractions 1 and 2 (based on the nucleobase absorption at 260 nm) provides a remarkable probe concentration. However, the two thiolated molecules compete for adsorption on the silver surface, but DTT takes advantage of its 1000 times greater concentration in the initial mixture, which favours its surface adsorption. Figure 8.8 (b) shows that when the column is well-packed a better separation is possible. An intense DNA spectrum is observed in fraction 2, in addition to a weak DTT fingerprint. Although the complex spectrum collected from fraction 1 cannot only be ascribed to the oligonucleotides, it recalls some features of the coupled C-N, C-C stretchings and C-H/N-H bending of the nucleobases heterocycles in the 1200-1500 cm^{-1} region. Indeed, a methyl-chloro isothiazolinone (MCI) based biocide is present in the columns, whose structure is consistent with the detected vibrational pattern. Finally, spectra in Figure 8.8 (c) were obtained thanks to the introduction of a number of elutions before the mixture separation, in order to clean the column from the residual storage buffer. Although MCI is still detected in fraction 1, its fingerprint is less evident. Moreover, volumes are slightly reduced, resulting in the concentration of the oligo-probe in fraction 2, as also demonstrated by the UV quantification of the DNA concentrations. Fraction 2 is used in the subsequent experiments. Next section focuses on the interpretation of DNA spectrum.

8.3.2.2 Interpretation of probe Raman signal

Although the SERS detection of oligonucleotides is broadly discussed in the literature, different and contrasting findings have been reported. Such diversity concerns with the vibrational spectra

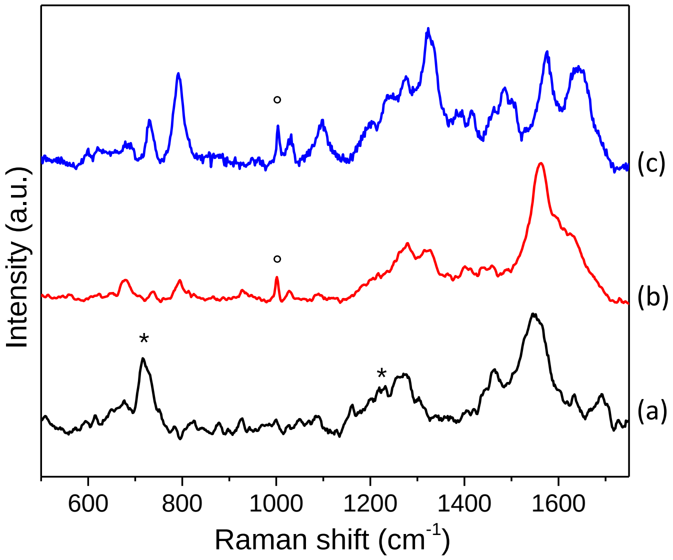

Figure 8.9 SERS spectra of (a) vertically oriented DNA, (b) intermediately oriented DNA, (c) tilted or surface lying DNA. The asterisks mark the DTT peaks, while the circles highlight BSA peaks.

dependence on the molecular conformation. Generally, all the studies agree on the observation that oligos spectra are dominated by the nucleobases modes. Among the reports dealing with thiol-immobilized oligos, however, few examples of the differences encountered can be given. Bahroumi et al. obtained spectra dominated by of adenine bands, ascribing this behaviour to the higher Raman cross section of this base.[133] On the contrary, Abell et al. were able to observe the vibrational fingerprint of all the different components.[135] According to our results, the observed DNA spectra vary between two extremes. The two types of vibrational patterns are depicted in Figure 8.9, along with an intermediate spectrum, probably arising from the simultaneous presence of the two conformations. On the one hand, a highly reproducible spectrum, characterized by few peaks around 830 cm^{-1}, 1275 cm^{-1}, 1460 cm^{-1}, 1556-60 cm^{-1} and 1690 cm^{-1} is recorded in presence of a partial surface coverage with DTT molecules or for very high probe concentrations. Although this whole pattern was never reported in the literature, few studies assign the 1275 cm^{-1} band to an out-of-plane deformation of the amino group of adenine[119], while the 1460 cm^{-1} and 1556 cm^{-1} bands can be ascribed to the C2-N3, N1-C6 stretching combined to C2-H bending and NH_2 scissoring of the same nucleobase. The peak at 830 cm^{-1} is instead a backbone mode related to the O-P-O stretching.[222] Finally, thymine carbonyl stretching can be observed at Raman shifts as high as 1690 cm^{-1} if the Raman spectrum rather than the SERS one is concerned.[118] Interestingly, ring breathing modes are not present. According to the selection rules of the electromagnetic mechanism, this occurs if the nucleobases lie parallel to the silver surface. Breathing is indeed an in-plane vibration, giving rise to high intensities only if the molecule is tilted or in a standing up orientation with respect to the surface. The sum of these observations indicates that the oligonucleotide is immobilized in a backbone vertical, hence nucleobase horizontal, conformation. On the other hand, spectra very similar to the ones presented by Abell et al., showing typical contributions by all the nucleobases, can be observed if the DNA is immobilized in absence of short chain spacers. In detail, adenine (730 cm^{-1}), cytosine and thymine (790 cm^{-1}) breathing modes are visible in the low frequency range[122], deoxyribose mode and PO^-_2 stretching are detected at 1030 and 1096 cm^{-1} [125] and C-N ring stretching of thymine (1246 cm^{-1}), cytosine (1270 cm^{-1}) and adenine (1325 cm^{-1}) are well resolved. Moreover, typical guanine bands are found at 1480 cm^{-1} and 1580 cm^{-1}, attributed to C-N stretching/N-H bending and NH_2 scissoring.[8] Partial convolution of the second one to the corresponding adenine 1577 cm^{-1} peak is expected. Finally, a distinct band at 1636-1640 cm^{-1} represents the carbonyl

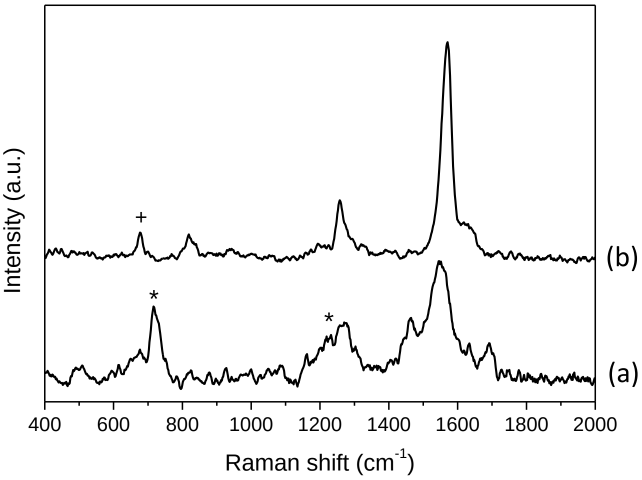

Figure 8.10 SERS spectra of the immobilized DNA (a) on Ag-PSD membranes in presence of DTT and (b) on printed Ag-pSi. The asterisks mark the DTT peaks, while the + sign indicates a typical contaminant of printed NPs.

stretching of the pyrimidine bases, interacting with the metal surface.[118] Note that, unlike the SERS spectra reported in Figure 8.8, these ones are recorded on Ag-PSD membranes after dilution in buffers of the separated fractions and overnight immobilization of the probe. Samples were therefore pre-treated with BSA, whose peak at 1001 cm^{-1} due to the aromatic aminoacids[114] is visible in spectra (a) and (b) but hardly detectable in the profile of spectrum (c). This observation suggests that DTT is able to completely replace BSA as blocking agent of the silver surface, causing the vertical orientation of the probe also for low probe surface densities. Despite the very good effectiveness of BSA passivation, the protein does not induce a vertical conformation, as its size is quite bigger than the oligo-probe one.

Furthermore, the vertically oriented probe spectrum is not only observed in presence of DTT, but also after immobilization of the thiolated DNA on printed Ag-pSi SERS substrates. Slight peak shifts are detected, which are related to the different nature of the silver NPs (4-MBA peaks are also found at lower Raman shifts for Ag-PSD membranes), but the overall pattern is easily recognized, as shown in Figure 8.10. Changes of the intensity ratios are probably related to differences in the conformation, but further analysis with deuterated water exchange is needed for a more reliable assignment of these features. The vertical orientation of the probe can be rationalized as a consequence of a higher DNA surface density, due to the concentration of the oligonucleotides in the limited area of the printed stripe (the same probe concentration was used).

8.3.2.2.1 Effect of probe concentration

The above discussion has highlighted that the detected SERS spectral features of the probe show a surface-density dependence. Due to the importance of this parameter for a proper hybridization and for the interpretation of the SERS measurements, the immobilization of DNA in a concentration range between 1 µM and 50 µM is evaluated. Figure 8.11 reports the average spectra extracted by Raman maps acquired on Ag-PSD substrates. It should be noted that under these Raman measurement conditions, optimized for the biodetection, and due to signal averaging, the typical vibrational fingerprint of BSA protein emerges in the spectra of the passivated samples. Following the previous literature, amide I at 1660 cm^{-1}, protein side chain deformations at 1453 cm^{-1} and the contribution of the disordered α-helix structure of the BSA in the amide III bands (1252 cm^{-1}) are identified.[114] Intense peaks, related to the aromatic aminoacids, are present as well (1001 cm^{-1}, 1203 cm^{-1}, 1370 cm^{-1}, 1614 cm^{-1}), indicating a partial degree of unfolding. C-S stretching of cysteine

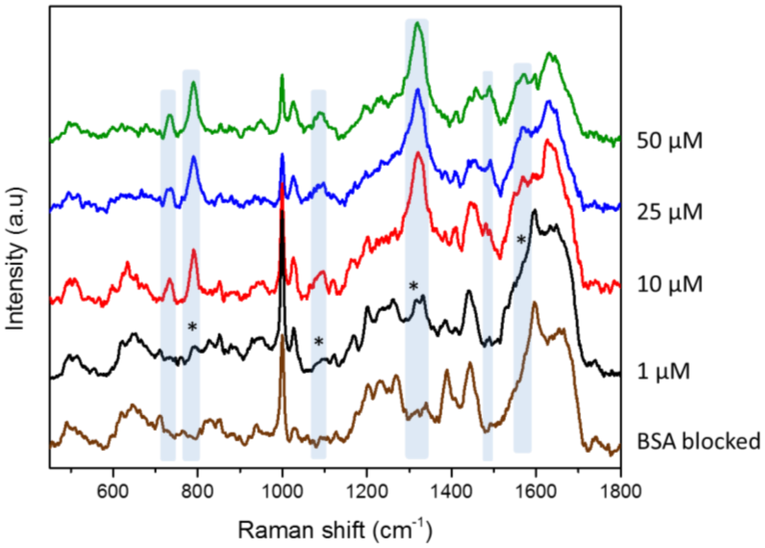

Figure 8.11 SERS spectra of the DNA probe immobilized on Ag-PSD membranes at several concentrations (1 to 50 µM). The spectrum of the BSA-passivated substrate is reported as reference.

residues are detected as a broad band around 656 cm^{-1} due to conformational variability, along with the disulphide peak at 505 cm^{-1}. This complex but reproducible background is expected to merge with the oligo spectral features, especially at low concentrations. Indeed, the immobilization of the probe from a 1 µM solution results in the appearance of oligo-related bands, which are marked by the asterisks. Assignments are the same as for the probe spectrum (c) in Figure 8.9. All the main oligonucleotide bands are clearly observed at 10 µM concentration (highlighted in blue). At the same time, a decrease of the BSA background is noticed, which evidences that the protein is gradually replaced by the DNA probe on the silver NPs surface, due to its specific binding through the free and freshly reduced thiol group. The presence of the BSA spectrum complicates a rough quantitative estimation of the probe signal intensity *vs.* DNA concentration. In fact, the integrated area of the 1325 cm^{-1} peak is affected by the background due to the protein, whose contribution is not the same for the prepared specimens. However, a first data visualization can be based on the normalization of the calculated values to the 1001 cm^{-1} peak of BSA, whose intensity should be proportional to the background contribution in the 1200-1500 cm^{-1} range. Based on this calculation, the SERS intensity of the DNA spectrum increases until 25 µM concentration, then it experiences a saturation, as confirmed by visual inspection of the spectra. It should be noted, that the saturation is already observed at 10 µM for the ring breathing modes (730 and 790 cm^{-1}), which is consistent with the orientational dependence of their intensities. As the probe surface density increases, the fraction of tilted or surface bound strands is reduced. Consequently, the overall contribution to the breathing modes is decreased, resulting in an apparent saturation due to the balance between the lowered intensity and the increased number of immobilized probes. Surprisingly, the saturation is however reached without a clear transition to the densely packed probe related SERS signal. The co-immobilization of short chain spacers is probably essential to achieve the vertical probe arrangement, unless an extremely high DNA excess is employed. The short thiols could be involved in the reorganization of the mixed DNA-BSA-thiol layer on the NPs surface, driving an easier displacement of the protein. It should be noticed that no comparative data about the performances of the tilted and vertical oriented DNA layers toward miRNAs hybridization are available at the moment, but they would be of interest to understand if the bioassay could benefit of the intentional addition of a short chain spacer such as mercaptohexanol or mercaptopropanol.

8.3.3 miRNA hybridization

The results of the previous section indicate that a probe concentration of 25 µM is enough to achieve a DNA monolayer on the silver NPs. Apparently, as suggested by the spectra of the immobilized oligos, enough space is left on the surface to allow miRNA hybridization. However, this can only be assessed by monitoring the hybridization efficiency. A cy5-miRNA222, whose detection is remarkably easier due to the presence of the SERS label, is employed to optimize the hybridization. Afterwards, the corresponding unlabelled miRNA222 is detected in the Ag-PSD chip.

8.3.3.1 Labelled miRNA222-cy5 detection

First, the dependence of the hybridization efficiency on the DNA concentration is studied. The spectra shown in Figure 8.12 are derived from the averaging of the SERS maps acquired on the samples functionalized with several DNA concentrations and subsequently incubated for 1 h with a 1 µM miRNA-cy5 solution. miRNA signal, dominated by the Cyanine 5 vibrational pattern, is detected for all the substrates, confirming the successful hybridization. As for the 1 µM DNA concentration the spectrum of BSA is still distinguished. At higher probe concentrations the signal of the miRNA-cy5 completely overwhelms the one of the other species. The high intensity of the SERS spectrum allows the calculation of the area of miRNA-cy5 1400 cm^{-1} band without any interference. The resulting integrated intensity is plotted in Figure 8.13 *vs.* the DNA concentration. Again, miRNA-cy5 signal increases until 25 µM, while for a higher probe concentration, a saturation is observed. These data agree very well with the ones reported for the DNA binding to the silver surface (Figure 8.13 (b)), showing that the amount of hybridized miRNA-cy5 is strictly correlated to the amount of immobilized probe. Although the estimation of the hybridization efficiency is not possible, as it requires that the Raman cross sections of the two detected species is similar (not the case for DNA and miRNA-cy-5, where the cyanine 5 cross section is higher), the observation of the same trend for the probe and the target SERS intensity is an important result. Moreover, 25 µM is indicated as a suitable concentration for probe immobilization and is consequently employed in the successive experiments. It should also be noted that the RSD value obtained by SERS mapping is around 15% at this concentration.

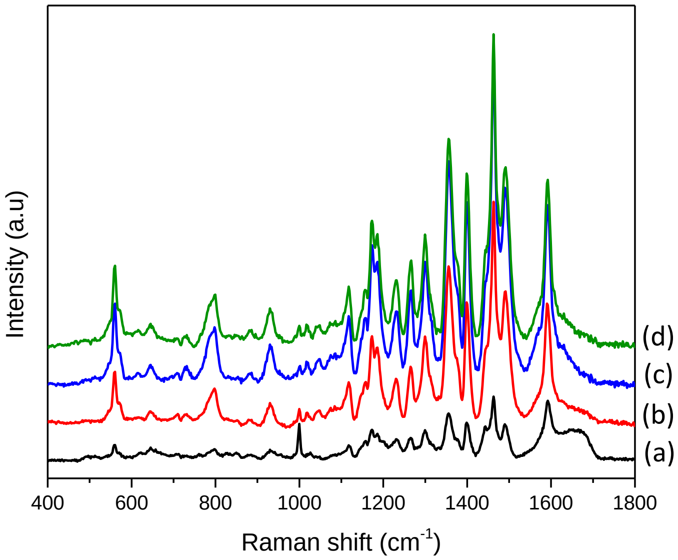

Figure 8.12 SERS spectra acquired after the hybridization step with miRNA-cy5 at 1 µM concentration on the substrates of Figure 8.11, functionalized with DNA at several concentrations: (a) 1 µM, (b) 10 µM, (c) 25 µM and (d) 50 µM.

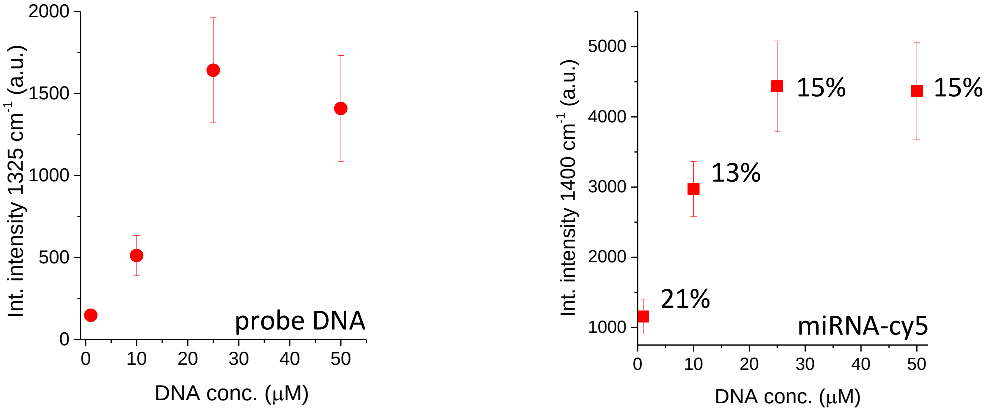

(a) (b)

Figure 8.13 SERS integrated intensity of (a) 1325 cm^{-1} band of DNA, normalized to the BSA peak and (b) 1400 cm^{-1} miRNA-cy5 peak. Relative standard deviations are evidenced for each point on the plot for the target detection.

The entire bioassay is then applied to Ag-PSD membranes, for several miRNA-Cy5 concentrations. Three control samples are included: A) passivated with BSA, B) incubated with the miRNA-cy5 but without the immobilization of the probe and C) incubated with the DNA probe. The spectra from these substrates are reported in the bottom of Figure 8.14. The comparison of the spectrum of sample A, which only presents BSA fingerprint peaks, with the one of sample B gives information about the nonspecific binding. Actually, if nonspecific interactions are occurring, miRNA-cy5 spectrum would be observed on sample B. This is not our case, where measurements taken on B are almost identical to the ones recorded on A. Such results furtherly confirm that BSA passivation prevents the binding of miRNA-cy5 at the silver surface. Spectrum C of the immobilized probe displays the usual features of tilted oligonucleotides. In addition to the control samples, miRNA-cy5 hybridized SERS substrates are studied in the 10^{-6}-10^{-9} M miRNA-cy5 concentration range.

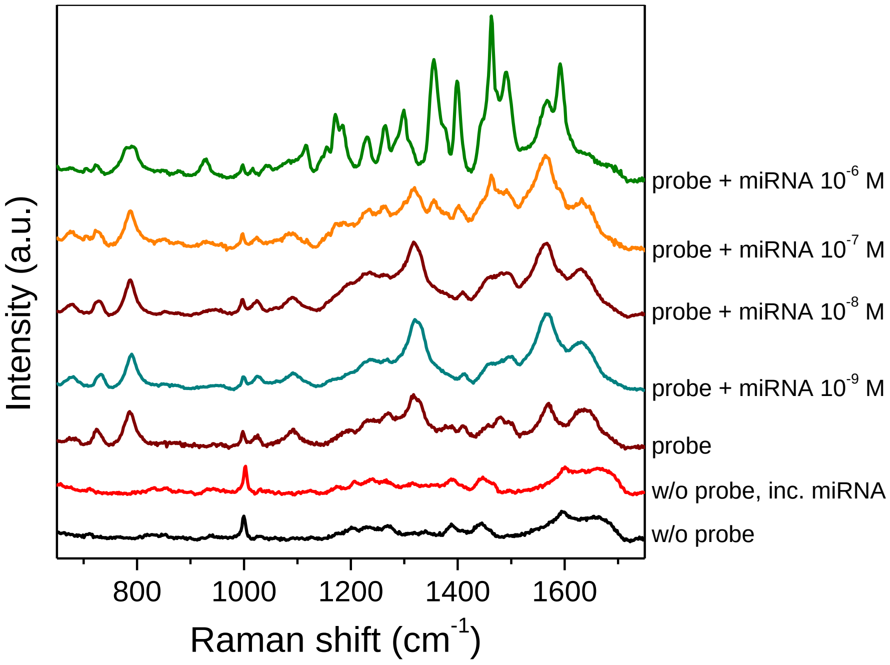

Figure 8.14 From bottom to top: SERS spectra of the control samples (1-3) and of the SERS substrates after immobilization and hybridization with miRNA-cy5 at 1 μM, 100 nM, 10 nM and 1 nM concentrations

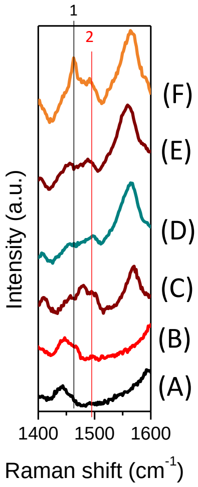

(a)

	I1 (1464) cm^{-1}	I1 (1495) cm^{-1}	I1/I2
miRNA 1 µM	365	231	1.58
miRNA 100 nM	53	36	1.47
miRNA 10 nM	45	51	0.88
miRNA 1 nM	45.6	59	0.77
cDNA	27.5	43.5	0.63

(b)

Figure 8.15 (a) SERS spectra of (A) control sample without probe, (B) control sample without probe, incubated with miRNA, (C) probe DNA, (D) probe DNA+miRNA-cy5 1 nM, (E) probe DNA+miRNA-cy5 10 nM, (F) probe DNA+miRNA-cy5 100 nM. The vertical lines mark the analysed miRNA-Cy5 bands. (b) Table reporting the intensity ratios between the 1464 and 1495 cm^{-1} bands for samples from (C) to (F) and the 1 µM miRNA-cy5 hybridized substrate.

The hybridization with 1 µM miRNA-cy5 is easily detected through the intense cy5 spectrum. Some features related to the probe spectrum can be identified by the inspection of the spectrum of the hybridized complex, as a marked shoulder at 1570 cm^{-1} and the broadening of the peak around 790 cm^{-1}. The miRNA-cy5 vibrational pattern, superimposed to the DNA one, appears after incubation in the 10^{-7} M solution. Below this concentration, a careful analysis of the spectra is necessary. The most intense miRNA-cy 5 peak is found at 1464 cm^{-1}. It is part of a doublet (with the band at 1495 cm^{-1}), which can be more easily identified, since the DNA spectrum is less crowded in this region. The intensity ratio between these two peaks can be used as a marker of the merging of miRNA-cy5 and DNA spectra. The calculated ratios are reported in Figure 8.15 (b). Although the lowest value is obtained for immobilized probe, it should be noted that for the 1 nM miRNA-cy5 concentration the difference is slight. Moreover, if the control sample (B) is concerned, the appearance of a weak shoulder on the right side of the BSA band can be noticed. This deeper inspection of the spectra reveals that a small amount of nonspecific signal could affect the measurements for very low miRNA-cy5 concentrations and suggests that a reliable detection cannot be performed below 10^{-8} M under these conditions, unless more sophisticated data analysis methods are considered.

Finally, taking into account that Cyanine 5 alone is first detectable after incubation in 10^{-9} M solutions on the Ag-PSD membranes, the observed miRNA-cy5 hybridization at 10^{-8} M concentration represents a good result. Indeed, the cy5 label is not directly in contact with the silver surface in this case and a reduction of the SERS enhancement is expected.

8.3.3.2 Unlabelled miRNA222 hybridization

The hybridization assay reported in the previous section exploits the presence of a high Raman cross section SERS marker conjugated to the miRNA, in order to aid the biomarker detection at lower concentrations. Such a detection scheme presents however many drawbacks, primarily the need of the chemical modification of the target with the label, and was therefore employed only to test the biofunctionalization protocol. The label-free detection of miRNA222 is instead the real target. In the approach presented in the followings, the miRNA222 hybridization to the immobilized

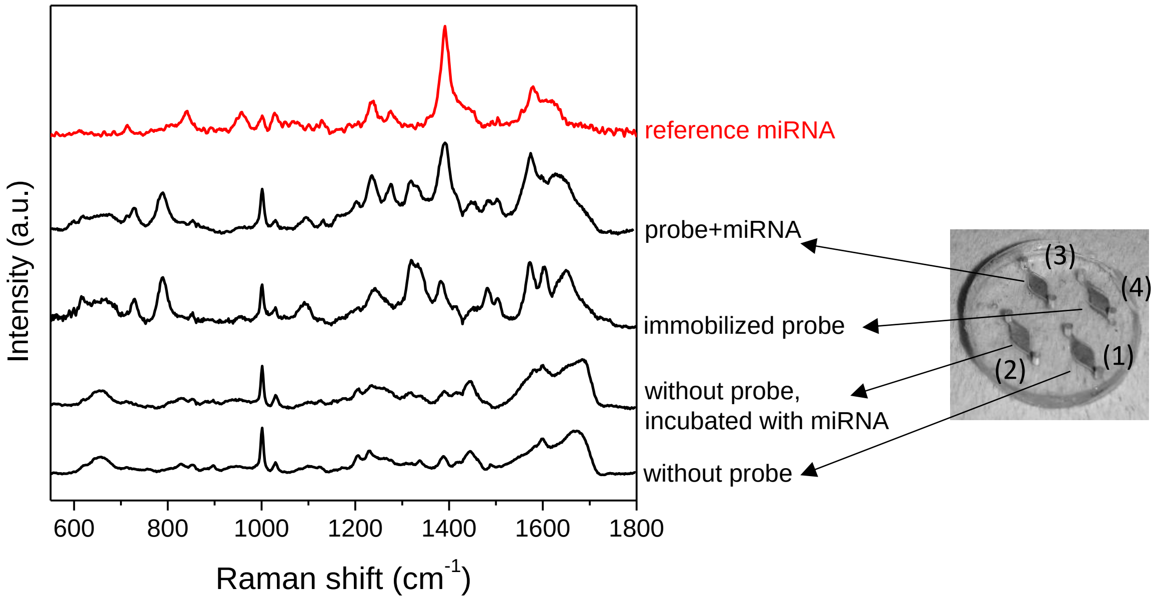

Figure 8.16 SERS spectra (from bottom to top) of negative control chamber without probe, negative control chamber without probe, incubated with miRNA, immobilized DNA and DNA+miRNA222 acquired in the chip. The reference spectrum of the spotted miRNA222 is drawn in red.

DNA probes will be assessed by the detection of their Raman fingerprint. The assay is performed in the multichamber microfluidic chip discussed in chapter 7, which allows the comparative analysis of the negative controls and the hybridized complex on the same platform. Note that this is a proof-of concept experiment, while a chip design including more chambers is needed to extend the number of screened sequences or miRNA concentrations. Nevertheless, this can be easily achieved by changing the cover design.

Figure 8.16 collects the measurements acquired on the chip and a reference spectrum of miRNA222. The observed vibrational pattern suggests that the miRNA is adsorbed in a particular conformation, with the nucleobases almost parallel to the surface. This results in a very low intensity of the ring breathing modes, as already observed for an RNA homopolymer analysed by TERS.[223] Moreover, the spectrum seems to be dominated by uracil vibrational modes detected at 713 cm^{-1}, 998 cm^{-1}, 1236 cm^{-1} (NH, CH bending)[224], 1275 cm^{-1}, 1390 cm^{-1} (NH, CH bending and NC–CN + CC–CN stretching), 1580 cm^{-1} (ring stretching involving the CO group)[224] and 1626 cm^{-1} (carbonyl stretching). Superposition of adenine and guanine NH_2 out of plane deformation and scissoring or cytosine C-N stretching in the 1250-1270 cm^{-1} range are also possible.

For what concerns the measurements in the chip, the negative controls exhibit the usual BSA spectrum, derived from the passivation of the surface. No bands of the miRNA222 are observed in the control chamber 2, thus highlighting the absence of nonspecific signal. A typical DNA spectrum is detected in chamber 3, unless that guanine modes at 1480 and 1580 cm^{-1} show an increased enhancement with respect to the previous experiments. After the hybridization with 1 μM miRNA222, an evident change in the spectral features occurs. The differences are mainly due to the superposition of intense miRNA-222 peaks to the ones of DNA. Variations of the intensity ratios of ring breathing modes, previously detected by Green et al. upon DNA-DNA hybridization, are indeed not observed. The very low contribution of these modes to the reference miRNA spectrum is likely to be responsible for this finding. Moreover, it is worth to underline that diverse surface preparation methods can lead to completely different results, although both systems are able to provide the detection of the hybridized complex.

8.3.4 Cross-check through ELISA assay

The ELISA is an established technique routinely applied in the bioanalytical field. Its specificity is determined by a high affinity recognition, while its sensitivity depends on the amplification of the initial event through an enzymatic reaction occurring only if the binding has taken place. A great robustness is attributed to the ELISA test, because interfering events can be better controlled.

An ELISA assay, optimized for the application to metal dielectric nanostructured substrates, is exploited to validate the protocol. In detail, the hybridization of miRNA222 to DNA can be assessed by an ELISA test as follows. The SERS substrates are functionalized with the oligo probes as previously discussed and blocked with BSA. Afterwards a 5'-biotinilated miRNA222 is employed for the incubation of the SERS substrates at room temperature. After washings, samples are incubated in a streptavidin-modified Horse Radish Peroxidase enzyme (Str-HRP) solution. As biotin strongly and specifically binds streptavidin, a certain amount of the conjugated enzyme is immobilized on the surface depending on the presence of the biotinylated miRNA. Finally, the so called development of the assay is performed by the addition of a TMB substrate solution which initiates an enzymatic colorimetric reaction. The assay is stopped at a certain reaction time adding H_2SO_4 (0.5 M), with a 1:1 TMB:H_2SO_4 ratio and the Optical Density (OD) of the solution is immediately measured at 450 nm and at 630 nm by means of a 2100-C microplate reader (Ivymen Optic System). Such value, properly compared to a calibration curve, provides quantitative data about the number of streptavidin molecules bonded to the surface. Figure 8.17 reports the results of an ELISA assay for the detection of several concentrations of miRNA222. The first four right columns refer to the control samples, including the three used in SERS, and a mismatch test. This fourth control sample is functionalized with the DNA and then incubated with a non-complementary miRNA21. The plot confirms that the whole optimized protocol allows the hybridization of miRNA222, as also assessed by SERS spectroscopy. Low signals are collected by the control samples, evidencing a high signal-to-noise ratio due to the biofunctionalization protocol. The LOD (limit of detection), specific to the ELISA test, is shown to be 2.3 x 10^{10} molecules/cm^2, thus enabling miRNA222 detection in a physiological range of concentrations (1-100 nM).

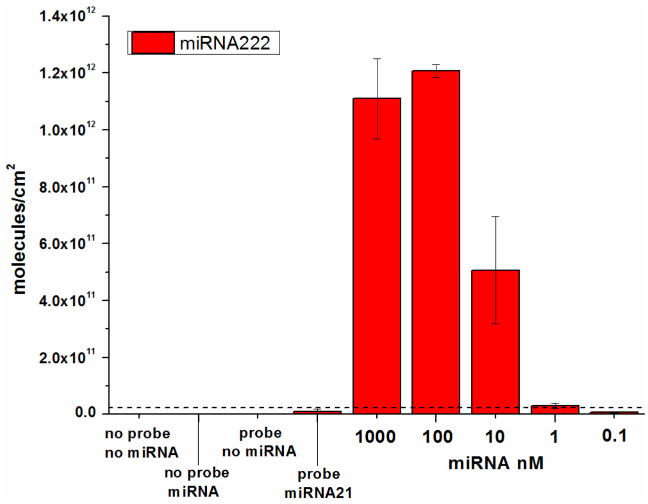

Figure 8.17 Detection of different concentration of miRNA by means of functionalized Ag-PSD samples. The dashed line represents the LOD (2.3 x 10^{10} molecules/cm^2).

8.3.5 Conclusions

In summary, a suitable protocol for miRNA detection on SERS substrates has been developed. Printed Ag-pSi samples and Ag-PSD membranes can be employed for biosensing purposes thanks to their stability in the required buffers and under physiological conditions. The different protocol steps were optimized, reducing non-specific interactions and tuning the probe surface density. miRNA detection was initially performed using a cy5 labelled sequence in order to achieve an easier identification of the hybridized complex through the intense and distinguishable signal of the dye. Ultimately, an unlabelled miRNA222 could be detected exploiting a multianalyte configuration in the four-chamber microfluidic Ag-PSD chip.

Conclusions and future perspectives

The aim of this thesis was to provide new metal-dielectric nanostructures based on silvered porous silicon, suitable for Surface Enhanced Raman Scattering applications in the biosensing and bioanalytical fields. Starting from previously developed Ag-pSi substrates, a full characterization has revealed new aspects of their plasmonic and SERS properties, enabling a better understanding of their Raman enhancement mechanisms under different excitation energies. Their SERS response, determined by the heterogeneous morphology, is suggested to depend on a wide population of nanoparticles under visible excitation, but mainly to be driven by near-field plasmonic modes in low-density hot-spots, when the wavelength is shifted towards the NIR range. A direct practical consequence of this behaviour is the high variability of the SERS intensities at 785 nm, which limits their use to qualitative analysis at this excitation energy, despite the higher efficiency.

Two approaches for the development of multiplexing SERS platforms have been presented. The first one concerns with silver NPs patterns synthesized by inkjet printing. Silver nitrate based inks were printed on the reducing surface of freshly etched porous silicon to synthesize silver nanostructures in situ. The SERS efficiency of the prepared substrates is mainly driven by the inter-particle separation, which has been tuned by the optimization of the inkjet printing and ink parameters. EARE of 10^8, comparable to values obtained for Ag-pSi substrates grown by immersion plating technique, have been assessed, while a better signal uniformity is attained. In the second approach, porous silicon membranes were patterned shielding the starting silicon wafer with a PDMS mask during the electrochemical etching. After transfer of the pSi membranes to a PDMS substrate, multichamber microfluidic chips were prepared by bonding the same PDMS cover used for the pattern definition. Silvered chips, decorated by immersion plating, were tested with 4-MBA, showing good enhancements of 7 orders of magnitude in off-electronic resonance conditions and a calibrated response versus the analyte concentration. The microfluidic synthesis of silver NPs in pSi-PDMS chips was demonstrated.

A bioassay for miRNA biomarkers detection has been finally applied to the Ag-pSi nanostructures. The integrity of the SERS substrates after buffer incubation was checked and confirmed for printed Ag-pSi samples and Ag-PSD membranes. Each step of the biofunctionalization protocol, including non-specific binding minimization, DNA capture probe immobilization and miRNA222 hybridization has been studied and optimized, proving the label-free detection of miRNA222.

The great potential of the prepared silver coated porous silicon nanostructures for sensitive multiplexed biodetection opens the way to several applications in the bioanalytical field. The exploitation of Ag-PSD chips is particularly attractive due to the excellent SERS efficiency and good intra-substrate uniformity that should allow reliable quantitative analysis. miRNA detection assay is expected to take advantage of two possible improvements, including the application of multivariate analysis methods to the label free assay and the boost of the SERS efficiency under electronic resonance conditions by means of the development of a sandwich assay, in which a resonant dye-labelled probe is employed.

References

1 S. Schlücker, *Angew. Chemie Int. Ed.*, 2014, **53**, 4756–4795.

2 C. Muehlethaler, M. Leona and J. R. Lombardi, *Anal. Chem.*, 2016, **88**, 152–169.

3 Y. Zhang, Z. Wang, L. Wu, Y. Pei, P. Chen and Y. Cui, *Analyst*, 2014, **00**, 1–7.

4 M. Fleischmann, P. J. Hendra and A. J. McQuillan, *Chem. Phys. Lett.*, 1974, **26**, 163–166.

5 Q. Li, B. Li and Y. Wang, *RSC Adv.*, 2013, **3**, 13015.

6 G. Turrel and J. Corset, *Raman Microscopy*, Elsevier Ltd, 1996.

7 K. Kneipp, H. Kneipp, I. Itzkan, R. R. Dasari and M. S. Feld, *J. Phys. Condens. Matter*, 2002, **14**, 597–624.

8 B. Giese and D. McNaughton, *Phys. Chem. Chem. Phys.*, 2002, **4**, 5171–5182.

9 N. Jayanth, S. Ramachandran and M. Puranik, *J. Phys. Chem. A*, 2009, **113**, 1459–1471.

10 P. Kukura, D. W. McCamant and R. a Mathies, *Annu. Rev. Phys. Chem.*, 2007, **58**, 461–488.

11 K. Kong, C. Kendall, N. Stone and I. Notingher, *Adv. Drug Deliv. Rev.*, 2015, **89**, 121–134.

12 V. Parchaňský, J. Kapitán and P. Bouř, *RSC Adv.*, 2014, **4**, 57125–57136.

13 M. Moskovits, *Rev. Mod. Phys.*, 1985, **57**, 783–826.

14 S. Nie and S. R. Emory, *Science (80-.).*, 1997, **275**, 1102–1106.

15 K. Kneipp, Y. Wang, H. Kneipp, L. T. Perelman, I. Itzkan, R. R. Dasari and M. S. Feld, *Phys. Rev. Lett.*, 1997, **78**, 1667–1670.

16 B. L. Darby, P. G. Etchegoin and E. C. Le Ru, *Phys. Chem. Chem. Phys.*, 2014, **16**, 23895–23899.

17 K. Kneipp, H. Kneipp, I. Itzkan, R. R. Dasari and M. S. Feld, 2002, **14**, 597–624.

18 J. Cao, T. Sun and K. T. V. Grattan, *Sensors Actuators B Chem.*, 2014, **195**, 332–351.

19 S. A. Maier, *Plasmonics: fundamentals and applications*, Springer, 2007, vol. 1.

20 G. Baffou and R. Quidant, *Laser Photonics Rev.*, 2013, **7**, 171–187.

21 P. N. Njoki, I.-I. S. Lim, D. Mott, H.-Y. Park, B. Khan, S. Mishra, R. Sujakumar, J. Luo and C.-J. Zhong, *J. Phys. Chem. C*, 2007, **111**, 14664–14669.

22 A. J. Haes, C. L. Haynes, A. D. Mcfarland and G. C. Schatz, *MRS Bull.*, 2005, **30**, 368–375.

23 A. Shiohara, J. Langer, L. Polavarapu and L. M. Liz-Marzán, *Nanoscale*, 2014, **6**, 9817–23.

24 J. P. Camden, J. a Dieringer, Y. Wang, D. J. Masiello, L. D. Marks, G. C. Schatz and R. P. Van Duyne, *J. Am. Chem. Soc.*, 2008, **130**, 12616–7.

25 S. Grésillon, L. Aigouy, A. Boccara, J. Rivoal, X. Quelin, C. Desmarest, P. Gadenne, V. Shubin, A. Sarychev and V. Shalaev, *Phys. Rev. Lett.*, 1999, **82**, 4520–4523.

26 C. J. Murphy, T. K. Sau, A. M. Gole, C. J. Orendorff, J. Gao, L. Gou, S. E. Hunyadi and T. Li, *J. Phys. Chem. B*, 2005, **109**, 13857–13870.

27 N. J. Halas, S. Lal, W. S. Chang, S. Link and P. Nordlander, *Chem. Rev.*, 2011, **111**, 3913–3961.

28 J. M. McMahon, S. Li, L. K. Ausman and G. C. Schatz, *J. Phys. Chem. C*, 2012, **116**, 1627–1637.

29 E. C. Le Ru and P. G. Etchegoin, *J. Chem. Phys.*, 2009, **130**, 4–7.

30 P. Nordlander, C. Oubre, E. Prodan, K. Li and M. I. Stockman, *Nano Lett.*, 2004, **4**, 899–903.

31 S. Kessentini, D. Barchiesi, C. D'Andrea, A. Toma, N. Guillot, E. Di Fabrizio, B. Fazio, O. M. Maragò, P. G. Gucciardi and M. Lamy De La Chapelle, *J. Phys. Chem. C*, 2014, **118**, 3209–3219.

32 M. Rycenga, X. Xia, C. H. Moran, F. Zhou, D. Qin, Z. Y. Li and Y. Xia, *Angew. Chemie - Int. Ed.*, 2011, **50**, 5473–5477.

33 J. B. Herzog, M. W. Knight, Y. Li, K. M. Evans, N. J. Halas and N. Douglas, *Nano Lett.*, 2013, **13**, 1359–1364.

34 C. Zhang, B.-Q. Chen, Z.-Y. Li, Y. Xia and Y.-G. Chen, *J. Phys. Chem. C*, 2015, **119**, 16836–16845.

35 P. Guo, D. Sikdar, X. Huang, K. J. Si, W. Xiong, S. Gong, L. W. Yap, M. Premaratne and W. Cheng, *Nanoscale*, 2015, **7**, 2862–2868.

36 Y. Hu, R. C. Fleming and R. A. Drezek, *Opt. Express*, 2008, **16**, 19579–19591.

37 H. Xu and M. Käll, *Sensors Actuators B Chem.*, 2002, **87**, 244–249.

38 A. Virga, R. Gazia, L. Pallavidino, P. Mandracci, E. Descrovi, A. Chiodoni, F. Geobaldo and F. Giorgis, *Phys. Status Solidi*, 2010, **7**, 1196– 1199.

39 M. W. Knight, Y. Wu, J. B. Lassiter, P. Nordlander and N. J. Halas, *Nano Lett.*, 2009, **9**, 2188–2192.

40 Y. Fleger, Y. Mastai, M. Rosenbluh and D. H. Dressler, *Surf. Sci.*, 2009, **603**, 788–793.

41 T. Shegai, A. Vaskevich, I. Rubinstein and G. Haran, *J. Am. Chem. Soc.*, 2009, **131**, 14390–14398.

42 Y. Chao, Q. Zhou, Y. Li, Y. Yan, Y. Wu and J. Zheng, *J. Phys. Chem. C*, 2007, **111**, 16990–16995.

43 A. Virga, P. Rivolo, F. Frascella, A. Angelini, E. Descrovi, F. Geobaldo and F. Giorgis, *J. Phys. Chem. C*, 2013, **117**, 20139–20145.

44 L. Zhao, L. Jensen and G. C. Schatz, *J. Am. Chem. Soc.*, 2006, **128**, 2911–2919.

45 E. C. Le Ru, E. Blackie, M. Meyer and P. G. Etchegoin, *J. Phys. Chem. C*, 2007, **111**, 13794–13803.

46 W. Meng, F. Hu, X. Jiang and L. Lu, *Nanoscale Res. Lett.*, 2015, **10**, 1–8.

47 A. Virga, P. Rivolo, E. Descrovi, A. Chiolerio, G. Digregorio, F. Frascella, M. Soster, F. Bussolino, S. Marchiò, F. Geobaldo and F. Giorgis, *J. Raman Spectrosc.*, 2012, **43**, 730–736.

48 W. Shen, X. Lin, C. Jiang, C. Li, H. Lin, J. Huang, S. Wang, G. Liu, X. Yan, Q. Zhong and B. Ren, *Angew. Chemie Int. Ed.*, 2015, **54**, 7308–7312.

49 M. Fan, G. F. S. Andrade and A. G. Brolo, *Anal. Chim. Acta*, 2011, **693**, 7–25.

50 M. Jahn, S. Patze, I. Hidi, R. Knipper, A. I. Radu, A. Mühlig, S. Yüksel, V. Peksa, K. Weber, T. Mayerhöfer, D. Cialla-May and J. Popp, *Analyst*, 2016, **141**, 756–793.

51 Y. Xia, Y. Xiong, B. Lim and S. E. Skrabalak, *Angew. Chemie Int. Ed.*, 2009, **48**, 60–103.

52 M. J. Mulvihill, X. Y. Ling, J. Henzie and P. Yang, *J. Am. Chem. Soc.*, 2010, **132**, 268–274.

53 P. C. Lee and D. Meisel, *J. Phys. Chem.*, 1982, **86**, 3391–3395.

54 J. A. Creighton, C. G. Blatchford and M. G. Albrecht, *J. Chem. Soc. Faraday Trans. 2*, 1979, **75**, 790.

55 N. Leopold and B. Lendl, *J. Phys. Chem. B*, 2003, **107**, 5723–5727.

56 C. Luo, Y. Zhang, X. Zeng, Y. Zeng and Y. Wang, *J. Colloid Interface Sci.*, 2005, **288**, 444–448.

57 D. Steinigeweg and S. Schlücker, *Chem. Commun.*, 2012, **48**, 8682–8684.

58 T. K. Sau and C. J. Murphy, *Langmuir*, 2004, **20**, 6414–6420.

59 J. E. Millstone, S. J. Hurst, G. S. Métraux, J. I. Cutler and C. a. Mirkin, *Small*, 2009, **5**, 646–664.

60 A. Mao, X. Jin, X. Gu, X. Wei and G. Yang, *J. Mol. Struct.*, 2012, **1021**, 158–161.

61 J. Spadavecchia, A. Barras, J. Lyskawa, P. Woisel, W. Laure, C. M. Pradier, R. Boukherroub and S. Szunerits, *Anal. Chem.*, 2013, **85**, 3288–3296.

62 C. G. Blatchford, J. R. Campbell and J. A. Creighton, *Surf. Sci.*, 1982, **120**, 435–455.

63 M. V Canamares, J. V Garcia-Ramos, J. D. Gomez-Varga, C. Domingo and S. Sanchez-Cortes, *Langmuir*, 2005, **21**, 8546–8553.

64 S. E. J. Bell and M. R. McCourt, *Phys. Chem. Chem. Phys.*, 2009, **11**, 7455–7462.

65 A. S. Urban, X. Shen, Y. Wang, N. Large, H. Wang, M. W. Knight, P. Nordlander, H. Chen and N. J. Halas, *Nano Lett.*, 2013, **13**, 4399–4403.

66 V. V. Thacker, L. O. Herrmann, D. O. Sigle, T. Zhang, T. Liedl, J. J. Baumberg and U. F. Keyser, *Nat. Commun.*, 2014, **5**, 1–7.

67 W. Li, P. H. C. Camargo, L. Au, Q. Zhang, M. Rycenga and Y. Xia, *Angew. Chemie - Int. Ed.*, 2010, **49**, 164–168.

68 V. Amendola and M. Meneghetti, *Phys. Chem. Chem. Phys.*, 2009, **11**, 3805–3821.

69 V. Amendola and M. Meneghetti, *Phys. Chem. Chem. Phys.*, 2012, **15**, 3027–3046.

70 V. Amendola, S. Scaramuzza, S. Agnoli, G. Granozzi, M. Meneghetti, G. Campo, V. Bonanni, F. Pineider, C. Sangregorio, P. Ghigna, S. Polizzi, P. Riello, S. Fiameni and L. Nodari, *Nano Res.*, 2015, **8**, 4007–4023.

71 T. Vo-Dinh, *Trends Anal. Chem.*, 1998, **17**, 557–582.

72 M. Kahl, E. Voges, S. Kostrewa, C. Viets and W. Hill, *Sensors Actuators B Chem.*, 1998, **51**, 285–291.

73 L. Gunnarsson, E. J. Bjerneld, H. Xu, S. Petronis, B. Kasemo and M. Kall, *Appl. Phys. Lett.*, 2001, **78**, 802–804.

74 I. Sow, J. Grand, G. Levi, J. Aubard, N. Felidj, J. C. Tinguely, A. Hohenau and J. R. Krenn, *J. Phys. Chem. C*, 2013, **117**, 25650–25658.

75 Z. Tian, B. Ren and D. Wu, *J. Phys. Chem. B*, 2002, **106**, 9463–9483.

76 J. L. Yao, G. P. Pan, K. H. Xue, D. Y. Wu, B. Ren, D. M. Sun, J. Tang, X. Xu and Z. Q. Tian, *Pure Appl. Chem.*, 2000, **72**, 221–228.

77 K. Long, X. Luo, H. Nan, D. Du and W. Zhao, *J. Appl. Phys.*, 2013, **114**, 183520.

78 D. Wu, J. Li, B. Ren and Z. Tian, *Chem. Soc. Rev.*, 2008, **37**, 1025–1041.

79 C. L. Haynes and R. P. Van Duyne, *J. Phys. Chem. B*, 2001, **105**, 5599–5611.

80 Y.-J. Liu, H. Y. Chu and Y.-P. Zhao, *J. Phys. Chem. C*, 2010, **114**, 8176–8183.

81 A. Lamberti, A. Virga, A. Angelini, A. Ricci, E. Descrovi, M. Cocuzza and F. Giorgis, *RSC Adv.*, 2015, **5**, 4404–4410.

82 M. Fan and A. G. Brolo, *Phys. Chem. Chem. Phys.*, 2009, **11**, 7381–7389.

83 H. Wang, J. Kundu and N. J. Halas, *Angew. Chemie - Int. Ed.*, 2007, **46**, 9040–9044.

84 G. F. S. Andrade, M. Fan and A. G. Brolo, *Biosens. Bioelectron.*, 2010, **25**, 2270–2275.

85 H.-W. Cheng, S.-Y. Huan, H.-L. Wu, G.-L. Shen and R.-Q. Yu, *Anal. Chem.*, 2009, **81**, 9902–9912.

86 W. Ruan, W. Ji, X. Xue, Y. Cui, L. Chen, T. Zhou, L. Niu, X. Li, J. Zhang and B. Zhao, *J. Raman Spectrosc.*, 2011, **42**, 1492–1496.

87 C. Peng, Y. Song, G. Wei, W. Zhang, Z. Li and W.-F. Dong, *J. Colloid Interface Sci.*, 2008, **317**, 183–90.

88 A. Tao, F. Kim, C. Hess, J. Goldberger, R. He, Y. Sun, Y. Xia and P. Yang, *Nano Lett.*, 2003, **3**, 1229–1233.

89 Y. Kitahama, T. Itoh, J. Aoyama, K. Nishikata and Y. Ozaki, *Chem. Commun.*, 2009, 6563–6565.

90 C. Fang, A. Agarwal, H. Ji, W. Y. Karen and L. Yobas, *Nanotechnology*, 2009, **405604**, 405604–405613.

91 J. Yan, X. Han, J. He, L. Kang, B. Zhang, Y. Du, H. Zhao, C. Dong, H. L. Wang and P. Xu, *ACS Appl. Mater. Interfaces*, 2012, **4**, 2752–2756.

92 Q. Zhang, J.-J. Xu, Y. Liu and H.-Y. Chen, *Lab Chip*, 2008, **8**, 352–357.

93 F. A. Harraz, T. Tsuboi, J. Sasano, T. Sakka and Y. H. Ogata, *J. Electrochem. Soc.*, 2002, **149**, C456.

94 K. Fukami, F. A. Harraz, T. Yamauchi, T. Sakka and Y. H. Ogata, *Electrochem. commun.*, 2008, **10**, 56–60.

95 A. Uhlir, *Bell Syst. Tech. J.*, 1956, **35**, 333–347.

96 V. Lehmann and U. Gösele, *Appl. Phys. Lett.*, 1991, **58**, 856.

97 O. Bisi, S. Ossicini and L. Pavesi, *Surf. Sci. Rep.*, 2000, **38**, 1–126.

98 F. A. Harraz, *Sensors Actuators, B Chem.*, 2014, **202**, 897–912.

99 T. Tsuboi, T. Sakka and Y. H. Ogata, *J. Appl. Phys.*, 1998, **83**, 4501.

100 D. B. Mawhinney, J. A. Glass and J. T. Yates, *J. Phys. Chem. B*, 1997, **101**, 1202–1206.

101 H. Bandarenka, S. Redko, A. Smirnov, A. Panarin, S. Terekhov, P. Nenzi, M. Balucani and V. Bondarenko, *Nanoscale Res. Lett.*, 2012, **7**, 477.

102 S. Chan, S. Kwon, T.-W. Koo, L. P. Lee and A. A. Berlin, *Adv. Mater.*, 2003, **15**, 1595–1598.

103 H. Lin, J. Mock, D. Smith, T. Gao and M. J. Sailor, *J. Phys. Chem. B*, 2004, **108**, 11654–11659.

104 H. Lin, J. Mock, D. Smith, T. Gao and M. J. Sailor, 2004, **1**, 11654–11659.

105 A. Y. Panarin, V. S. Chirvony, K. I. Kholostov, P. Y. Turpin and S. N. Terekhov, *J. Appl. Spectrosc.*, 2009, **76**, 280–287.

106 M. Kosovic, M. Balarin, M. Ivanda, Đ. Vedran, M. Marcius, M. Ristic and O. Gamulin, *Appl. Spectrosc.*, 2015, **69**, 1417–1424.

107 F. A. Harraz, A. A. Ismail, H. Bouzid, S. A. Al-Sayari, A. Al-Hajry and M. S. Al-Assiri, *Appl. Surf. Sci.*, 2015, **331**, 241–247.

108 H. Bandarenka, K. Artsemyeva, S. Redko, A. Panarin, S. Terekhov and V. Bondarenko, *Phys. Status Solidi*, 2013, **10**, 624–627.

109 E. Koglin and M. J. Schwuger, *Faraday Discuss.*, 1992, **94**, 213–220.

110 A. Bonifacio, S. Dalla Marta, R. Spizzo, S. Cervo, A. Steffan and A. Colombatti, *Anal. Bioanal. Chem.*, 2014, **406**, 2355–2365.

111 K. Kneipp, Y. Wang, R. R. Dasari and M. S. Feld, *Spectrochim. Acta A*, 1995, **51**, 481–487.

112 K. E. Shafer-Peltier, C. L. Haynes, M. R. Glucksberg and R. P. Van Duyne, *J. Am. Chem. Soc.*, 2003, **125**, 588–593.

113 W. R. Premasiri, J. C. Lee and L. D. Ziegler, *J. Phys. Chem. B*, 2012, **116**, 9376–9386.

114 C. David, N. Guillot, H. Shen, T. Toury and M. Lamy De La Chapelle, *Nanotechnology*, 2010, **21**, 475501.

115 E. Podstawka, Y. Ozaki and L. M. Proniewicz, *Appl. Spectrosc.*, 2004, **58**, 1147–1156.

116 Y. C. Cao, R. Jin, J.-M. Nam, C. S. Thaxton and C. A. Mirkin, *J. Am. Chem. Soc.*, 2003, **125**, 14676–14677.

117 M. Cottat, C. D'Andrea, R. Yasukuni, N. Malashikhina, R. Grinyte, N. Lidgi-Guigui, B. Fazio, A. Sutton, O. Oudar, N. Charnaux, V. Pavlov, A. Toma, E. Di Fabrizio, P. G. Gucciardi and M. Lamy de la Chapelle, *J. Phys. Chem. C*, 2015, **119**, 15532–15540.

118 C. Otto, T. J. J. van den Tweel, F. F. M. de Mul and J. Greve, *J. Raman Spectrosc.*, 1986, **17**, 289–298.

119 J. S. Suh and M. Moskovits, *J. Am. Chem. Soc.*, 1986, **108**, 4711–4718.

120 S. E. J. Bell and N. M. S. Sirimuthu, *J. Am. Chem. Soc.*, 2006, **128**, 15580–15581.

121 E. Papadopoulou and S. E. J. Bell, *Chem. Eur. J.*, 2012, **18**, 5394–5400.

122 E. Prado, N. Daugey, S. Plumet, L. Servant and S. Lecomte, *Chem. Commun.*, 2011, **47**, 7425–7427.

123 L. He, M. Langlet, P. Bouvier, C. Calers, C.-M. Pradier and V. Stambouli, *J. Phys. Chem. C*, 2014, **118**, 25658–25670.

124 E. Bailo and V. Deckert, *Angew. Chemie - Int. Ed.*, 2008, **47**, 1658–1661.

125 S. Najjar, D. Talaga, L. Schué, Y. Coffinier, S. Szunerits, R. Boukherroub, L. Servant, V. Rodriguez and S. Bonhommeau, *J. Phys. Chem. C*, 2014, **118**, 1174–1181.

126 E. Stofer, C. Chipot and R. Lavery, *J. Am. Chem. Soc.*, 1999, **121**, 9503–9508.

127 P. Yakovchuk, E. Protozanova and M. D. Frank-Kamenetskii, *Nucleic Acid Res.*, 2006, **34**, 564–574.

128 A. W. Peterson, R. J. Heaton and R. M. Georgiadis, *Nucleic Acids Res.*, 2001, **29**, 5163–5168.

129 D. Cialla, K. Weber, R. Böhme, U. Hübner, H. Schneidewind, M. Zeisberger, R. Mattheis, R.

Möller and J. Popp, *Beilstein J. Nanotechnol.*, 2011, **2**, 501–508.

130 A. Kamińska, A. Sivanesan, E. Witkowska, J. Gołąb, M. Winiarska, D. Nowis, I. Dzięcielewski, J. L. Weyher and J. Waluk, *J Chem Chem Eng*, 2013, **7**, 972–978.

131 Y. C. Cao, R. Jin and C. A. Mirkin, *Science (80-.).*, 2002, **297**, 1536–1540.

132 T. Vo-Dinh, K. Houck and D. L. Stokes, *Anal. Chem.*, 1994, **66**, 3379–3383.

133 A. Barhoumi and N. J. Halas, *J. Am. Chem. Soc.*, 2010, **132**, 12792–12793.

134 M. Green, F.-M. Liu, L. Cohen, P. Köllensperger and T. Cass, *Faraday Discuss.*, 2006, **132**, 269–280.

135 J. L. Abell, J. M. Garren, J. D. Driskell, R. A. Tripp and Y. Zhao, *J. Am. Chem. Soc.*, 2012, **134**, 12889–12892.

136 H. T. Ngo, H.-N. Wang, A. M. Fales and T. Vo-Dinh, *Anal. Chem.*, 2013, **85**, 6378–6383.

137 E. Papadopoulou and S. E. J. Bell, *Angew. Chemie - Int. Ed.*, 2011, **123**, 9224–9227.

138 S. Griffiths-Jones, H. K. Saini, S. Van Dongen and A. J. Enright, *Nucleic Acids Res.*, 2008, **36**, 154–158.

139 S. Lin and R. I. Gregory, *Nat. Rev. Cancer*, 2015, **15**, 321–333.

140 H. Dong, J. Lei, L. Ding, Y. Wen, H. Ju and X. Zhang, *Chem. Rev.*, 2013, **113**, 6207–6233.

141 S. L. Ameres, J. Martinez and R. Schroeder, *Cell*, 2007, **130**, 101–112.

142 M. Ha and V. N. Kim, *Nat. Rev. Mol. Cell Biol.*, 2014, **15**, 509–524.

143 K. Förstemann, Y. Tomari, T. Du, V. V. Vagin, A. M. Denli, D. P. Bratu, C. Klattenhoff, W. E. Theurkauf and P. D. Zamore, *PLoS Biol.*, 2005, **3**, 1187–1201.

144 J. L. Brenner, K. L. Jasiewicz, A. F. Fahley, B. J. Kemp and A. L. Abbott, *Curr. Biol.*, 2010, **20**, 1321–1325.

145 A. Srivastava, S. Suy, S. P. Collins and D. Kumar, *Mol. Cell. Pharmacol.*, 2011, **3**, 115–124.

146 J. Skog, T. Würdinger, S. van Rijn, D. H. Meijer, L. Gainche, M. Sena-Esteves, W. T. Curry, B. S. Carter, A. M. Krichevsky and X. O. Breakefield, *Nat. Cell Biol.*, 2008, **10**, 1470–1476.

147 W. Li and K. Ruan, *Anal. Bioanal. Chem.*, 2009, **394**, 1117–1124.

148 J. D. Driskell, A. G. Seto, L. P. Jones, S. Jokela, R. A. Dluhy, Y.-P. Zhao and R. A. Tripp, *Biosens. Bioelectron.*, 2008, **24**, 917–922.

149 B. Guven, F. C. Dudak, I. H. Boyaci, U. Tamer and M. Ozsoz, *Analyst*, 2014, **139**, 1141–1147.

150 J. L. Abell, J. D. Driskell, R. A. Dluhy, R. A. Tripp and Y.-P. Zhao, *Biosens. Bioelectron.*, 2009, **24**, 3663–3670.

151 W. Wu, L. Liu, Z. Dai, J. Liu, S. Yang, L. Zhou, X. Xiao, C. Jiang and V. A. L. Roy, *Sci. Rep.*, 2015, **5**, 10208.

152 W. W. Yu and I. M. White, *Anal. Chem.*, 2010, **82**, 9626–9630.

153 E. P. Hoppmann, W. W. Yu and I. M. White, *Methods*, 2013, **63**, 219–224.

154 Q. Yang, M. Deng, H. Li, M. Li, C. Zhang, W. Shen, Y. Li, D. Guo and Y. Song, *Nanoscale*, 2015, **7**, 421–425.

155 E. Tekin, P. J. Smith and U. S. Schubert, *Soft Matter*, 2008, **4**, 703–713.

156 N. Reis, C. Ainsley and B. Derby, *J. Appl. Phys.*, 2005, **97**, 094903–094908.

157 A. Kamyshny, J. Steinke and S. Magdassi, *Open Appl. Phys. J.*, 2011, **4**, 19–36.

158 W. W. Yu and I. M. White, *Analyst*, 2013, **138**, 1020–1025.

159 A. Chiolerio, A. Virga, P. Pandolfi, P. Martino, P. Rivolo, F. Geobaldo and F. Giorgis, *Nanoscale Res. Lett.*, 2012, **7**, 1–7.

160 J. C. McDonald, D. C. Duffy, J. R. Anderson, D. T. Chiu, H. Wu, O. J. Schueller and G. M. Whitesides, *Electrophoresis*, 2000, **21**, 27–40.

161 Q. Zhou and T. Kim, *Sensors Actuators B Chem.*, 2016, **227**, 504–514.

162 L. X. Quang, C. Lim, G. H. Seong, J. Choo, K. J. Do and S.-K. Yoo, *Lab Chip*, 2008, **8**, 2214–2219.

163 N. Choi, K. Lee, D. W. Lim, E. K. Lee, S.-I. Chang, K. W. Oh and J. Choo, *Lab Chip*, 2012, **12**, 5160–5167.

164 E. Prado, A. Colin, L. Servant and S. Lecomte, *J. Phys. Chem. C*, 2014, **118**, 13965–13971.

165 E. Kämmer, K. Olschewski, T. Bocklitz, P. Rösch, K. Weber, D. Cialla and J. Popp, *Phys. Chem. Chem. Phys.*, 2014, **16**, 9056–9063.

166 E. Kämmer, K. Olschewski, S. Stöckel, P. Rösch, K. Weber, D. Cialla-May, T. Bocklitz and J. Popp, *Anal. Bioanal. Chem.*, 2015, **407**, 8925–8929.

167 H. Mao, W. Wu, D. She, G. Sun, P. Lv and J. Xu, *Small*, 2014, **10**, 127–134.

168 G. L. Liu and L. P. Lee, *Appl. Phys. Lett.*, 2005, **87**, 074101.

169 A. Lamberti, A. Virga, A. Chiadò, A. Chiodoni, K. Bejtka, P. Rivolo and F. Giorgis, *J. Mater. Chem. C*, 2015, **3**, 6868–6875.

170 J. Parisi, Q. Dong and Y. Lei, *RSC Adv.*, 2015, **5**, 14081–14089.

171 J. Parisi, L. Su and Y. Lei, *Lab Chip*, 2013, **13**, 1501–8.

172 Y. Xie, S. Yang, Z. Mao, P. Li, C. Zhao, Z. Cohick, P.-H. Huang and T. J. Huang, *ACS Nano*, 2014, **12**, 12175–12184.

173 A. Lamberti, A. Virga and F. Giorgis, *RSC Adv.*, 2015, **5**, 105484–105488.

174 Y. Deng, M. N. Idso, D. D. Galvan and Q. Yu, *Anal. Chim. Acta*, 2015, **863**, 41–48.

175 Y.-J. Oh and K.-H. Jeong, *Lab Chip*, 2014, **14**, 865–868.

176 D. Lee, S. Lee, G. H. Seong, J. Choo, E. K. Lee, D. G. Gweon and S. Lee, *Appl. Spectrosc.*, 2006, **60**, 373–377.

177 B.-B. Xu, Z.-C. Ma, L. Wang, R. Zhang, L.-G. Niu, Z. Yang, Y.-L. Zhang, W.-H. Zheng, B. Zhao, Y. Xu, Q.-D. Chen, H. Xia and H.-B. Sun, *Lab Chip*, 2011, **11**, 3347–3351.

178 J. Qi, J. Zeng, F. Zhao, S. H. Lin, B. Raja, U. Strych, R. C. Willson and W.-C. Shih, *Nanoscale*, 2014, **6**, 8521–8526.

179 J. Goldstein, D. E. Newbury, D. C. Joy, C. E. Lyman, P. Echlin, E. Lifshin, L. Sawyer and J. R. Michael, *Scanning Electron Microscopy and X-ray Microanalysis*, Springer Science + Business Media, New York, 2003, vol. 44.

180 F. Houdellier, L. De Knoop, C. Gatel, A. Masseboeuf, S. Mamishin, Y. Taniguchi, M. Delmas, M. Monthioux, M. J. Hÿtch and E. Snoeck, *Ultramicroscopy*, 2015, **151**, 107–115.

181 K. D. Vernon-Parry, *III-Vs Rev.*, 2000, **13**, 40–44.

182 D. Cwikel, Q. Zhao, C. Liu, X. Su and A. Marmur, *Langmuir*, 2010, **26**, 15289–15294.

183 M. Żenkiewicz, *J. Achievemnts Mater. Manuf. Eng.*, 2007, **24**, 137–145.

184 F.-C. Wang and Y.-P. Zhao, *Colloid Polym Sci*, 2013, **291**, 307–315.

185 H. B. Eral, D. J. C. M. Mannetje and J. M. Oh, *Colloid Polym Sci*, 2012, **291**, 247–260.

186 Á. Muñoz-Noval, M. Hernando Pérez, V. Torres Costa, R. J. Martín Palma, P. J. De Pablo and M. Manso Silván, *Langmuir*, 2012, **28**, 1909–1913.

187 J. Jopp, H. Grüll and R. Yerushalmi-Rozen, *Langmuir*, 2004, **20**, 10015–10019.

188 R. N. Wenzel, *J. Ind. Eng. Chem.*, 1936, **28**, 988–994.

189 A. Lamberti, M. Quaglio, A. Sacco, M. Cocuzza and C. F. Pirri, *Appl. Surf. Sci.*, 2012, **258**, 9427–9431.

190 Beleites, C.; Sergo, V. (2015): 'hyperSpec: A Package to Handle Hyperspectral Data Sets in R.' R package version 0.98-20150304. http://hyperspec.r-forge.r-project.org.

191 R Core Team (2016): A language and environment for statistical computing. R Foundation for Statistical Computing, Vienna, Austria. URL https://www.R-project.org/.

192 A. Michota and J. Bukowska, *J. Raman Spectrosc.*, 2003, **34**, 21–25.

193 L. Yang, X. Jiang, W. Ruan, B. Zhao, W. Xu and J. R. Lombardi, *J. Phys. Chem. C*, 2008, **112**, 20095–20098.

194 P. Hildebrandt and M. Stockburger, *J. Phys. Chem.*, 1984, **88**, 5935–5944.

195 H. Watanabe, N. Hayazawa, Y. Inouye and S. Kawata, *J. Phys. Chem. B*, 2005, **109**, 5012–5020.

196 P. Bhatia, J. Consiglio, J. Diniz, J. E. Lu, C. Hoff, S. Ritz-schubert and R. H. Terrill, *J. Spectrosc.*, 2015, **2015**, 1–11.

197 S. A. Meyer, E. C. Le Ru and P. G. Etchegoin, *J. Phys. Chem. A*, 2010, **114**, 5515–5519.

198 S. P. Hastings, P. Swanglap, Z. Qian, Y. Fang, S.-J. Park, S. Link, N. Engheta and Z. Fakhraai, *ACS Nano*, 2014, **8**, 9025–9034.

199 A. Lamberti, A. Virga, P. Rivolo, A. Angelini and F. Giorgis, *J. Phys. Chem. B*, 2015, **119**, 8194–200.

200 Z. Liu, L. Cheng, L. Zhang, C. Jing, X. Shi and Z. Yang, *Nanoscale*, 2014, **6**, 2567–2572.

201 L. Wu and B. Shen, *Nanoscale*, 2013, **5**, 5274–5278.

202 C. Novara, F. Petracca, A. Virga, P. Rivolo, S. Ferrero, A. Chiolerio, F. Geobaldo, S. Porro and F. Giorgis, *Nanoscale Res. Lett.*, 2014, **9**, 527.

203 M. Pavese, S. Musso, S. Bianco, M. Giorcelli and N. Pugno, *J. Phys. Condens. Matter*, 2008, **20**, 474206–474213.

204 J. H. Song and M. J. Sailor, *Inorg. Chem.*, 1998, **37**, 3355–3360.

205 C. Novara, A. Lamberti, A. Chiadò, A. Virga, P. Rivolo, F. Geobaldo and F. Giorgis, *RSC Adv.*, 2016, **6**, 21865–21870.

206 TO2015A000227, 2015.

207 D. J. Sirbuly, G. M. Lowman, B. Scott, G. D. Stucky and S. K. Buratto, *Adv. Mater.*, 2003, **15**, 149–152.

208 A. G. Nassiopoulos, S. Grigoropoulos, L. Canham, A. Halimaoui, I. Berbezier, E. Gogolides and D. Papadimitriou, *Thin Solid Films*, 1995, **255**, 329–333.

209 I. Rea, A. Lamberti, I. Rendina, G. Coppola, M. Gioffrè, M. Iodice, M. Casalino, E. De Tommasi, L. De Stefano, I. Rea, A. Lamberti, I. Rendina and G. Coppola, *J. Appl. Phys.*, 2013, **107**, 014513.

210 B. S. Flavel, M. J. Sweetman, C. J. Shearer, J. G. Shapter and N. H. Voelcker, *ACS Appl. Mater. Interfaces*, 2011, **3**, 2463–2471.

211 M. Ladanov, P. Algarin-Amaris, G. Matthews, M. Ram, S. Thomas, A. Kumar and J. Wang, *Nanotechnology*, 2013, **24**, 375301.

212 Y. Zhao, Y. Wang, Y. Yang, J. Liu, Y. Song, Y. Cao, X. Chen, W. Yang, F. Wang, J. Gao, Z. Li and C. Yang, *J. Cancer*, 2015, **6**, 1230–1235.

213 K. L. Jarvis, T. J. Barnes and C. A. Prestidge, *Langmuir*, 2008, **24**, 14222–14226.

214 M. Archer, M. Christophersen and P. M. Fauchet, *Biomed. Microdevices*, 2004, 203–211.

215 R. Fu, C. Wang, J. Zhuang and W. Yang, *Colloids Surfaces A Physicochem. Eng. Asp.*, 2014, **444**, 326–329.

216 M. P. Schwartz, F. Cunin, R. W. Cheung and M. J. Sailor, *Phys. Status Solidi*, 2005, **202**, 1380–1384.

217 A. Janshoff, K.-P. S. Dancil, C. Steinem, D. P. Greiner, V. S.-Y. Lin, C. Gurtner, K. Motesharei, M. J. Sailor and M. R. Ghadiri, *J. Am. Chem. Soc.*, 1998, **120**, 12108–12116.

218 T. M. Herne and M. J. Tarlov, *J. Am. Chem. Soc.*, 1997, **119**, 8916–8920.

219 D. Y. Petrovykh, H. Kimura-Suda, L. J. Whitman and M. J. Tarlov, *J. Am. Chem. Soc.*, 2003, **125**, 5219–5226.

220 S. Il Cho, E. S. Park, K. Kim and M. S. Kim, *J. Mol. Struct.*, 1999, **479**, 83–92.

221 J. Kubackova, I. I. Lorenzo, D. Jancura and S. Sanchez-Cortes, *Phys. Chem. Chem. Phys.*, 2014, **14**, 11461–11470.

222 L. Q. Dong, J. Z. Zhou, L. L. Wu, P. Dong and Z. H. Lin, *Chem. Phys. Lett.*, 2002, **354**, 458–465.

223 R. Treffer, X. Lin, E. Bailo, T. Deckert-Gaudig and V. Deckert, *Beilstein J. Nanotechnol.*, 2011,

2, 628–637.

224 K. Cho, J. Choo and S. Joo, *Spectrochim. Acta A*, 2005, **61**, 1141–1145.

Publications and Conferences

International Journal Papers

C. Novara, F. Petracca, A. Virga, P. Rivolo, S. Ferrero, A. Chiolerio, F. Geobaldo, S. Porro, F. Giorgis
"SERS active silver nanoparticles synthesized by inkjet printing on mesoporous silicon" (2014) *Nanoscale Research Letters*, 9, 527, DOI:10.1186/1556-276X-9-527

C. Novara, A. Lamberti, A. Chiadò, A. Virga, P. Rivolo, F. Geobaldo, F. Giorgis
"Surface enhanced Raman spectroscopy on porous silicon membranes decorated with Ag nanoparticles integrated in elastomeric microfluidic chips" (2016) *RSC Advances*, 6, 21865, DOI: 10.1039/c5ra26746c

C. Novara, S. Dalla Marta, A. Virga, A. Lamberti, A. Angelini, A. Chiadò, P. Rivolo, F. Geobaldo, V. Sergo, A. Bonifacio, F. Giorgis
"SERS active silver nanoparticles on porous silicon and PDMS substrates: a comparative study of uniformity and Raman efficiency" Submitted to *J. Phys Chem C*

Conference proceedings

C. Novara, A. Lamberti, P. Rivolo, A. Virga, A. Chiadò, F. Geobaldo, F. Giorgis
Optofluidic chip integrating silvered porous silicon membranes for multianalyte Surface Enhanced Raman Spectroscopy. In: International Conference on Advanced Vibrational Spectroscopy – ICAVS 8, Vienna (Austria) July 12-17. 2015, Abstracts Oral, pp. 298-299

A. Virga, A. Lamberti, A. Chiadò, C. Novara, P. Rivolo, S. Bianco, F. Geobaldo, F. Giorgis
Smart plasmonic metal-dielectric nanostructures for Surface Enhanced Raman Scattering. In: International Conference on Advanced Vibrational Spectroscopy – ICAVS 8, Vienna (Austria) July 12-17, 2015. Abstracts Poster, pp. 298-299

A. Virga, P. Rivolo, E. Descrovi, A. Angelini, C. Novara, K. Bejtka, A. Chiodoni, A. Ricci, F. Geobaldo, F. Giorgis
Single molecule detection in resonant SERS regime on metal-dielectric nanostructures based on porous silicon. In: XXIV International Conference on Raman Spectroscopy – XXIV ICORS, Jena (Germania) August 10-15, 2014, pp. 1436-1437

A. Virga, A. Chiadò, S. Ricciardi, F. Frascella, C. Novara, P. Rivolo, F. Geobaldo, F. Giorgis
Ag/pSi SERS platforms as biosensors for oligonucleotides/miRNA detection. In: XXIV International Conference on Raman Spectroscopy – XXIV ICORS, Jena (Germania) August 10-15, 2014, pp. 1466-1467

A. Virga, A. Chiadò, S. Ricciardi, F. Frascella, C. Novara, P. Rivolo, F. Geobaldo, F. Giorgis
Ag/pSi SERS platforms as biosensors for oligonucleotides/miRNA detection. In: 9th International Conference -Porous Semiconductors -Science and Technology-PSST 2014, Alicante - Benidorm, March 09-14, 2014, pp. 224-225

C. Novara, F. Petracca, A. Virga, P. Rivolo, F. Geobaldo, S. Porro, F. Giorgis
SERS active silver nanoparticles in mesoporous silicon synthesized by inkjet printing. In: 9th International Conference on Porous Semiconductors - Science and Technology - PSST 2014, Alicante - Benidorm, March 09-14, 2014, pp. 158-159

Conferences

Oral contributions

A. Chiadò, C. Novara, P. Rivolo, A. Lamberti, F. Geobaldo, F. Giorgis
"SERS-active metal-dielectric nanostructures integrated in microfluidic devices for ultra-sensitive label-free miRNA detection" 2016, 26th International conference Biosensors 2016, Gothenburg (Svezia) 25-27 maggio.

A. Lamberti, A. Chiadò, P. Rivolo, A. Chiodoni, K. Bejtka, C. Novara, F. Giorgis
"Ag-decorated TiO2 nanotube arrays grown by anodic oxidation as ultrasensitive SERS substrates for optofluidic sensing applications" 2016, 10th International conference Porous Semiconductors-Science and Technology- PSST 2016, Tarragona (Spagna) 6-11 marzo.

C. Novara, A. Lamberti, P. Rivolo, A. Virga, A. Chiadò, F. Geobaldo, F. Giorgis
"Optofluidic chip integrating silvered porous silicon membranes for multianalyte Surface Enhanced Raman Spectroscopy" 2015, International Conference on Advanced Vibrational Spectroscopy – ICAVS 8, Vienna (Austria) 12-17 luglio.

C. Novara, A. Lamberti, P. Rivolo, A. Virga, A. Chiadò, F. Geobaldo, F. Giorgis
"Integration of Silvered Porous Silicon in All-PDMS Optofluidic Chips for Multianalyte SERS Analysis" 2015, Fotonica 2015, Torino, 6-8 maggio.

A. Virga, A. Lamberti, A. Chiadò, C. Novara, P. Rivolo, F. Geobaldo, F. Giorgis "Smart metal-dielectric nanostructures for SERS Analysis applied to biosensing" 2015, Fotonica 2015, Torino, 6-8 maggio.

P. Rivolo, S. M. Severino, S. Ricciardi, F. Frascella, C. Novara, A. Virga, F.
Geobaldo "Protein immobilization on nanoporous silicon functionalized by RF activated plasma polymerization of acrylic acid" 2014, EUROPT(R)ODE - XII Conference on Optical Chemical Sensors & Biosensors – Atene (Grecia), 13-16 April 2014

"presenting author" of contributions 2, 3, e 4.

Poster contributions

P. Rivolo, S. Bianco, A. Lamberti, A. Chiadò, C. Novara, F. Giorgis

“Graphene-metal nanostructures as Surface Enhanced Raman Scattering substrates for biosensing” 2016, 26th International conference Biosensors 2016, Gothenburg (Svezia) 25-27 maggio.

C. Novara, A. Chiadò, A. Lamberti, P. Rivolo, F. Geobaldo, F. Giorgis
“Ag-coated porous silicon-PDMS membranes integrated in a microfluidic device for label free detection of micro-RNA” 2016, 10th International conference Porous Semiconductors- Science and Technology- PSST 2016, Tarragona (Spagna) 6-11 marzo.

A. Virga, A. Lamberti, A. Chiadò, C. Novara, P. Rivolo, S. Bianco, F. Geobaldo, F. Giorgis “Smart plasmonic metal-dielectric nanostructures for Surface Enhanced Raman Scattering” 2015, International Conference on Advanced Vibrational Spectroscopy – ICAVS 8, Vienna (Austria) 12-17 luglio.

A. Virga, P. Rivolo, E. Descrovi, A. Angelini, C. Novara, K. Bejtka, A. Chiodoni, A. Ricci, F. Geobaldo, F. Giorgis “Single molecule detection in resonant SERS regime on metal-dielectric nanostructures based on porous silicon” 2014, XXIV International Conference on Raman Spectroscopy – XXIV ICORS, Jena (Germania) 10-15 agosto.

A. Virga, A. Chiadò, S. Ricciardi, F. Frascella, C. Novara, P. Rivolo, F. Geobaldo, F. Giorgis “Ag/pSi SERS platforms as biosensors for oligonucleotides/miRNA detection” 2014, XXIV International Conference on Raman Spectroscopy – XXIV ICORS, Jena (Germania) 10-15 agosto.

6. A. Virga, S. Ricciardi, A. Chiadò, F. Frascella, P. Rivolo, C. Novara, A. Angelini, A. Lamberti, E. Descrovi, F. Geobaldo, F. Giorgis “Plasmonic nanoparticles optimized for single molecule detection: SERS analysis of oligonucleotides/miRNA” 2014, EUROPT(R)ODE - XII Conference on Optical Chemical Sensors & Biosensors – Atene (Grecia), 13-16 aprile.

C. Novara, F. Petracca, A. Virga, P. Rivolo, F. Geobaldo, S. Porro, F. Giorgis “SERS active silver nanoparticles synthesized by inkjet printing on silicon.” 2014, 9th International conference Porous Semiconductors- Science and Technology- PSST 2014, Alicante-Benidorm, 9-14 marzo.

A. Virga, A. Chiadò, S. Ricciardi, F. Frascella, C. Novara, P. Rivolo, F. Geobaldo,
F. Giorgis “Ag/pSi SERS platforms as biosensors for oligonucleotides/miRNA detection” 2014, 9th International Conference Porous Semiconductors -Science and Technology-PSST 2014, Alicante - Benidorm, 9-14 marzo.

“presenting author” of the poster contributions 2, 3 e 7.